Max-Planck-Institut für Kolloid- und Grenzflächenforschung

Model membrane interactions with ions and peptides at the air/water interface

Dissertation
zur Erlangung des akademischen Grades
"doctor rerum naturalium"
(Dr. rer. nat.)
in der Wissenschaftsdisziplin "Physikalische Chemie"

eingereicht an der
Mathematisch-Naturwissenschaftlichen Fakultät
der Universität Potsdam

von
Elena Maltseva

Potsdam, den 28 Februar 2005

Contents

1. Introduction

Biological membranes are the major constituents of the living organism. They play a key role in structural organization and functioning of prokaryotic and eukaryotic cells. Lipid molecules make up between 30 and 80% by mass of biological membranes. The remainder are proteins (20 to 60%) and carbohydrates (0 to 10%). In 1972 the *fluid mosaic model* was proposed and is now accepted as the basis of our understanding of cell membranes. The most important components of this model are a lipid bilayer with a thickness of 4-5 nm, and protein molecules, which can be attached or incorporated into the lipid bilayer. Three major kinds of lipids are present in the cell membranes: phospholipids, glycolipids and cholesterol. Phospholipids, the most common ones, are consisting of a glycerol backbone, two fatty acid chains and phosphate.

Different approaches are used to study processes occurring in biological membranes. These model systems help to understand individual properties of particular components of the membrane. They can be divided in three types: 1) monolayers, 2) planar bilayers and 3) vesicles. All these models have advantages and disadvantages. The present work is focused on Langmuir monolayers formed by various phospholipids.

Langmuir monolayers are convenient model systems to mimic biological membranes which can be considered as two weakly coupled monolayers. The great advantage of this model is a possibility to vary and control many thermodynamical parameters. One can incorporate peptides and proteins in it. Interactions between charged lipid membranes and ions can be investigated by changing the subphase composition (i.e. pH, ionic strength). The method helps to understand processes occurring at the membrane surface. However it may fail to model transmembrane processes.

Langmuir monolayers exhibit a rich polymorphism that can be examined by numerous techniques. Pressure-area isotherm measurements provide a straightforward physicochemical characterization since molecular area and lateral pressure are directly accessible. At certain temperatures, typical lipids such as double-chain phospholipids reveal a gas-analogous phase at very large molecular areas. During compression liquid-expanded (LE) and condensed (LC) phases can be observed. The structures of different condensed phases have been characterized with Å-resolution using grazing incidence x-ray diffraction technique (GIXD). The variation in electron density of a Langmuir film in the direction normal to the surface can be obtained from specular x-ray reflectivity measurements. Infrared reflection absorption spectroscopy (IRRAS) at the air/water interface provides information about both the LE and LC phase of lipids,

additionally it allows to estimate the orientation of particular dipoles at the interface. Moreover, the secondary structure of a peptide adsorbed at a lipid monolayer can be revealed.

Peptides (and proteins) are made by joining amino acids together via amide bonds. Peptides are distinguished from proteins by their shorter length (less then ca. 60 amino acid residues). Many peptides have biological activity and important functions in the body. For example, they are involved as neurotransmitters, neuromodulators and hormones in receptor-mediated signal transduction. More than 100 peptides with functions in the central and peripheral nervous systems, in immunological processes, in the cardiovascular system, and in the intestine are known. Peptides influence cell-cell communication upon interactions with receptors, and are involved in a number of biochemical processes, for example metabolism, pain, reproduction, and immune response. The other important type of peptides is antimicrobial peptides. They generally disrupt the membranes of a target cell, causing lysis of the cell. They can be used in medicine as an alternative to the common antibiotics. Besides, peptides primary and secondary structure alteration or absence of certain important peptides causes a number of diseases (Diabetes, Alzheimer's Disease, Respiratory distress syndrome, et. al.). Synthetic peptides are convenient models to study protein folding into certain secondary structure. Investigation of peptides representing particular regions or sequence motifs of large proteins can shed light onto specific binding sites of their precursors.

The objective of this work is to study interactions between phospholipid monolayers, ions and synthetic peptides. Phospholipids as well as peptides are charged molecules, therefore it is necessary to understand electrostatic interactions between charged membranes and counter ions such as low molecular weight metal ions or high molecular weight peptides. The lipids used in the work varied in their aliphatic chain length, head group charge and size. The peptides investigated are Amyloid β (1-40) peptide that is the major component of amyloid plaques found in the Alzheimer's disease, and B18, that is a peptide fragment having fusogenic properties of Sea Urchin Fertilization Protein Bindin. Interactions of both peptides with membranes are thought to play an important role in their biological actions. X-ray diffraction and infrared techniques provide information about changes in lipids and peptides structures induced by their interactions. Additionally circular dichroism (CD) spectroscopy is applied to check the interaction of peptides with phospholipid vesicles.

2. Theoretical background.

2.1 Langmuir monolayers

It has been found that lipids spread at the air/water interface form a monomolecular film, called Langmuir monolayer. The formation of Langmuir monolayers is a thermodynamically favorable process due to the amphiphilic character of lipid molecules. The amphiphile molecules are oriented at the interface in a way that the polar groups (glycerol, phosphate) point towards the water, while the alkyl groups are oriented away from the water. The structure is stabilized trough hydrophobic attractions between alkyl chains and hydrophilic polar group - subphase, polar group – polar group interactions. This orientation of lipids at the air/water interface gives a minimum surface energy and leads to the reduction of the surface tension in the presence of lipid monolayers at the interface.

Area per lipid molecule A, temperature and surface pressure π, which is the difference between the surface tension of the pure air/water interface σ_0 and the surface tension of the monolayer covered surface σ: $\pi=\sigma_0-\sigma$ - are parameters that describe the monolayer. By using a Langmuir trough (figure 2.1.1.) one can control these parameters and measure so called surface pressure/area isotherms. The surface tension (that can be transferred to the surface pressure) is measured by numerous techniques, among those the most frequently used is a Wilhelmy balance. In this method the surface tension is determined by suspending a plate of a material that is completely wetted by water (platinum, paper, glass), and measuring the downward force on it.

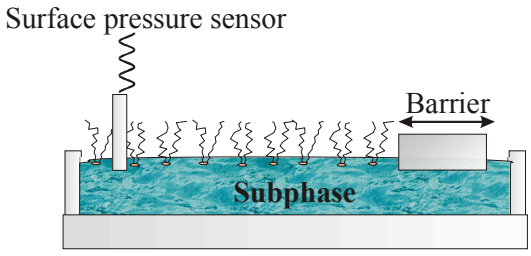

Figure 2.1.1. *A schematic diagram of a Langmuir trough. The area occupied by a monolayer is varied by moving a barrier across the water surface*

Phase transitions in Langmuir monolayers

For almost a century the surface pressure/area isotherms were the main source of thermodynamical data for monolayers. In this process whereby amphiphilic molecules are brought closer together during measurement, the interaction forces between amphiphiles undergo

certain changes, which are related to the packing of the molecules in the two-dimensional plane at the interface. The change in packing of amphiphilic molecules is analogous to the three-dimensional P vs. V isotherms. A generalized surface pressure/area isotherm of a Langmuir monolayer is sketched in figure 2.1.2.

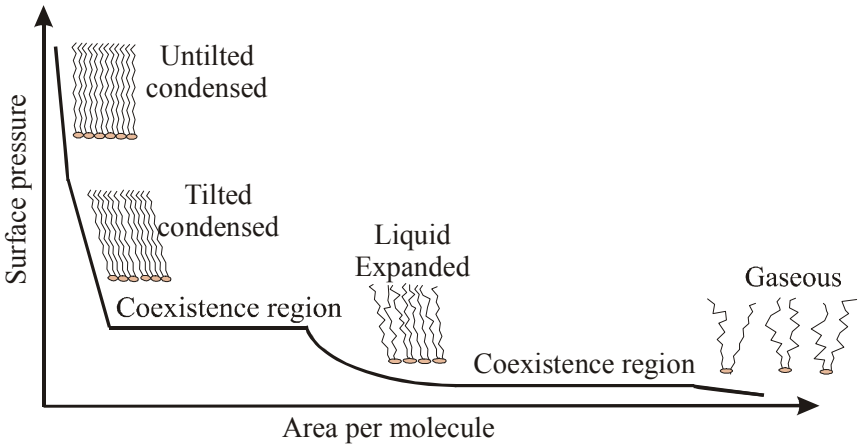

***Figure 2.1.2**. A generalized surface pressure/area isotherm of a Langmuir monolayer*

The very expanded film, when the distance between neighboring molecules is much larger then the size of the molecule, is well described as a two-dimensional gas. The ideal two-dimensional gas obeys the relationship: $\pi A=kT$ - which is analogous to the three-dimensional gas law. Compression of the monolayer leads to an increasing surface pressure and the monolayer transforms into the so called liquid expanded phase (LE or L_1). There is no detectable x-ray diffraction signal in this phase, as well as in the gaseous phase, because the heads of the molecules are transitionally disordered and the aliphatic chains are conformationally disordered. Further compression may lead to the next phase transition into the condensed phase, which is historically called liquid condensed phase (LC). This phase gives pronounced diffraction signals since the molecules in the monolayer exhibit positional order and preferential aliphatic chain alignment.

The phase transition from the liquid expanded to the condensed phase (LE/LC phase transition) can be described as a first order phase transition. The plateau is not perfectly horizontal in many systems, and this disagreement with the Gibbs phase rule give rise to a long standing controversy about the existence and the order of this transition. The direct optical observation by Fluorescence Microscopy [1, 2] and Brewster Angle Microscopy [3, 4] proofs that the plateau in the isotherm is a first order phase transition. The non-flat plateau of the LE/LC coexistence region can be explained by a limited cooperativity of the phase transition [5, 6]. The

gas/liquid expanded and liquid expanded/condensed transition lines merge at low temperatures, giving rise to the gas/liquid expanded/condensed triple point. Below this point a direct transition from a gaseous to the condensed phase is taking place.

The phase transition pressure depends on the temperature, length of the hydrocarbon chains and chemical structure of the head group. The longer molecules experience the phase transition at lower surface pressures. The head group dependence is usually much more complicated. The phase transition for the same chain length and various head group structures depends on their charge and size.

In the study of phase transitions, the Clausius-Clapeyron equation is the most fundamental thermodynamical relationship. It can be expressed for two-dimensional phase transitions as:

$$\frac{\Delta H_c}{T} = \frac{d\pi_c}{dT}(A_{LE} - A_{LC}) \text{ [5, 7, 8]}, \qquad (2.1.1)$$

where ΔH_c is the enthalpy of the transition, π_c is the transition pressure, A_{LE} is the area per molecule in the liquid expanded phase and A_{LC} is the area per molecule in the condensed phase. Extrapolation of the transition enthalpy to zero gives a critical temperature; above this temperature the condensed phase cannot be formed.

When a condensed phase is formed, the monolayer becomes less compressible (the slope of the isotherm is larger). Usually, the lipid forms first a tilted structure where the aliphatic chains are tilted from the surface normal, and then upon compression the tilt is reduced, ending in the untilted phase (chains are perpendicular to the surface). This results in a kink observed in the isotherm that corresponds to the second order phase transition between two condensed phases (tilted and untilted). In the untilted state, the distance between close-packed vertical molecules determines the molecular density, and therefore this condensed phase is even less compressible.

A number of condensed phases of fatty acids with different structures were found experimentally. Theoretical treatment accounting for most of the observed phases and transitions was given using a Landau theory of phase transitions by Kaganer and Loginov [9] for the long chain fatty acids. Using three order parameters, they reproduced the main features of the phase diagram obtained experimentally. One of the parameters describes the collective tilt of the molecules, while others describe one-dimensional crystallization involving herringbone ordering of the molecular backbone planes along the bond direction and normal to it.

Phospholipid monolayers possess similar structures as fatty acids, albeit with some structural restrictions [10]. There are two covalently bound to the glycerol backbone fatty acid

residues in phospholipids. Therefore, the free rotation of chains is not allowed and the lateral motion of a molecule requires movement of two chains and is hindered. Additionally, positions and orientations of the head group can be also involved in ordering.

Electrostatic interactions in phospholipid monolayers

Knowledge about electrostatical interactions in monolayers is required since phospholipids are charged molecules. Some of them, as phosphatidylcholines or phosphatidylethanolamines, are microscopically neutral (zwitterionic) in a wide pH range, while others, as phosphatidic acid, phosphatidylglycerol and phosphatidylserin, are negatively charged. The ionization degree of monolayers formed by the later lipids depends on both pH and ionic strength of the subphase.

The presence of charged molecules at the air/water interface results in the formation of the diffuse double layer consisting of counterions attracted from the subphase. With some approximations this process can be described by Gouy-Chapman theory [11-14]. The value of the electrical potential φ in a space filled with charges obeys the Poisson equation:

$$\varepsilon_0 div(\varepsilon grad\varphi) = \varepsilon\varepsilon_0\nabla^2\varphi = -\rho = -\sum_i n_i z_i e\,, \qquad (2.1.2)$$

where ε is the dielectric constant of water in the vicinity of a monolayer, ε_0 is the electrical constant in vacuum, ρ is the electrical charge density, n_i is the concentration of *i-th* ion, $z_i e$ is the charge of this ion. Gouy-Chapman theory assumes the Boltzmann distribution of ions near the charged surface.

$$n_i = n_{i0}\exp\left(-\frac{z_i e\varphi(x)}{kT}\right) \qquad (2.1.3)$$

where n_{io} is the bulk concentration of *i-th* ion. Combination of these two equations yields the Poisson Boltzmann equation [15]:

$$\frac{d^2\varphi}{dx^2} = -\frac{1}{\varepsilon\varepsilon_0}\sum_i z_i e n_{i0}\exp\left(-\frac{z_i e\varphi(x)}{kT}\right). \qquad (2.1.4)$$

For the friquent case of a symmetric electrolyte ($z_+=-z_-=z;\ n_0^+=n_0^-=n_0$) one can write the Poisson-Boltzmann equation in a simpler form:

$$\frac{d^2\varphi}{dx^2} = -\frac{\rho}{\varepsilon\varepsilon_0} = \frac{2zen_0}{\varepsilon\varepsilon_0}\sinh\left(\frac{ze\varphi(x)}{kT}\right), \qquad (2.1.5)$$

which can be transformed into:

$$\varphi_0 = \frac{2kT}{ze}\sinh^{-1}\left(\frac{\rho}{(8\varepsilon\varepsilon_0 kTn_0)}\right), \text{ if } x \to \infty,\ \varphi \to 0 \text{ and } \frac{d\varphi}{dx} \to 0, \qquad (2.1.6)$$

where φ_0 is the potential at the charged surface.

The Gouy-Chapman approach is valid for many systems, despite the fact, that the size of ions is not taken into consideration. Specific adsorption of counterions to charged surfaces can be added yielding the Gouy-Chapman-Stern theory. In this modification φ_0 is the electrical potential of the Stern layer (the potential is reduced by specifically adsorbed counterions). Another problem to be solved is the high counterion concentration in the vicinity of the charged surface, for example a phospholipid monolayer. If the phospholipid monolayer is negatively charged, the counterion can be an alkaly metal ion or/and proton. This should lead to a much higher proton concentration near the monolayer. The monolayer ionization degree α is determined by the surface proton concentration ($[H^+]_s$) and the equilibrium constant K_a for the acid group dissociation:

$$A^- + H^+ \xleftrightarrow{Ka} AH$$

$$\frac{\alpha}{1-\alpha} = \frac{K_a}{[H^+]_s} \qquad (2.1.7)$$

The surface proton concentration can be calculated if the proton bulk concentration $[H^+]_b$ is known by using the Boltzmann equation:

$$[H^+]_s = [H^+]_b \exp\left(-\frac{ze\varphi_0}{kT}\right) \qquad (2.1.8)$$

The Gouy-Chapman approach is then used to relate φ to the charge density at the interface [14] with consideration that the monolayer charge density (ρ) is equal to $\alpha e \cdot A$ (where A is the area occupied by a lipid molecule)

$$\varphi = \frac{2kT}{e}\sinh^{-1}\left(\frac{1.38\alpha}{A\sqrt{c}}\right) \qquad (2.1.9)$$

where c is the cation concentration. Combining the last three equations one obtains the following relation that can be written in a logarithmic form as:

$$pH_b = pK_a + \log\left(\frac{\alpha}{1-\alpha}\right) + 0.87\sinh^{-1}\left(\frac{1.38\alpha}{A\sqrt{c}}\right). \qquad (2.1.10)$$

The last equation has important consequences, which also have a big effect in real systems. For example the difference between bulk and surface pH in biological systems can lead to the

different ionization state of proteins in bulk and adsorbed to the membrane (monolayer). Another example is the difference between the pK_a measured and predicted for charged phospholipids and fatty acids. Even at modest monovalent salt concentration the difference between bulk and surface pH can be more than 3 pH units [12, 14].

2.2 Peptide structures

Peptides formally are polymers of amino acids, connected via amide bonds between the carboxygroup of one amino acid residue and the amino group of the following residue. They usually consist of 10 to 60 amino acid residues, proteins can consist of a much larger number of amino acids up to thousands. Natural peptides and proteins encoded by DNA contain 21 different amino acids (ApendixI). The chemical nature of the side chains of these amino acids determines the biochemical mode of action and structure of peptides. The structural description of proteins can be considered at four levels of organization: primary, secondary, tertiary and quaternary structures. The primary structure is a particular amino acid sequence of the protein (peptide). The secondary structure describes the tree-dimensional arrangement of the peptide backbone and it is stabilized via hydrogen bonds. The tertiary structure describes the three-dimensional structure or overall shape of a single peptide chain resulting from the intramolecular interactions between secondary structure elements. The quaternary structure is formed by two or more polypeptide chains associated by non-covalent interactions. Usually, peptides reproduce these structures only in some extent, due to their small size.

The nature of the amino acid side groups (primary structure) dictates structure-function relationships of peptides and proteins in solution. The hydrophobic amino acids are generally encountered in the interior of proteins shielded from direct contact with water. Conversely, the hydrophilic amino acids are generally found on the exterior of proteins as well as in the active centers of enzymatically active proteins.

Seven amino acid residues have ionizable side groups. Four of them are anionic: aspartic and glutamic acid, tyrosine and cysteine, and three are cationic: lysine, arginine and histidine. The *pK* values of their side groups are presented in table 1.1 in Appendix 1 [16]. Additionally the terminal amino group and the carboxilate group can be charged. Their charge can be important for short peptides. At physiological pH (pH = 7.4) aspartic and glutamic acid are negatively and lysine and arginine are positively charged, while cystein and tyrosine are not charged. Lysine and arginine are usually responsible for the electrostatic interactions of peptides and proteins with

membrane owing to their positive charge. The most interesting among the charged residues is histidine. The imidazole ring of histidine allows it to act either as a proton donor or acceptor at physiological pH. Hence, it is frequently found in the reactive center of enzymes. Equally important is the ability of histidines in hemoglobin to buffer protons from carbonic acid ionization in red blood cells. It is this property of hemoglobin that allows it to exchange O_2 and CO_2 at the tissues or lungs, respectively. The nonbonded electron pair of the basic form of histidine is always available for metal chelation. This versatility has been utilized and histidine is quite often found at the active site of enzymes and as a point of attachment for metal containing groups.

The primary alcohol of serine and threonine as well as the thiol (-SH) of cysteine allow these amino acids to act as nucleophiles during enzymatic catalysis. Additionally, the thiol of cysteine is able to form a disulfide bond with other cysteines. The formation of disulfide bonds within proteins is important for the formation of active structural domains in a large number of proteins. Disulfide bonding between cysteines in different polypeptide chains of oligomeric proteins plays a crucial role in ordering the structure of complex proteins.

The primary structure sometimes determines what secondary structure the peptide can have. However the same peptide (protein) with the same primary structure may adopt different secondary structures. A mistake in the primary structure (mutation) can stabilize the wrong secondary structure or change a peptide charge and hydrophobicity and this can lead to physiological dysfunction. Besides the changes in primary structure the wrong folding of proteins and peptides can be caused by other environmental factors such as: pH change, hydrophobic interactions with other cell constituents, chelating with metals and temperature change.

The peptide chain conformation preferred under physiological conditions is dominated by the energetically favored torsion angles φ, ψ and ω together with other stabilizing factors as hydrogen bonds and hydrophobic contacts. The accessible torsion angles for peptides are restricted as a consequence of the partial double bond character of the amide bond [17]. The accessible torsion angle regions are displayed in Ramachandran plots. This typical plot gives an indication of the conformations a peptide may adopt and this is confirmed by observations of X-ray protein structures.

Hydrogen bonds are basically formed between the NH-group and oxygen atom of carboxylate within the peptide backbone. Most proteins contain one or more stretches of amino acids that form a characteristic three-dimensional structure. The most common of these are the α-

helix, the β-conformation (or β-sheet) and turns. The unstructured parts are usually called random coil.

α-helix

The helix is a widely occurring secondary structure of proteins and peptides. The most common is the right-handed α-helix, which was originally proposed by Pauling and Corey (figure2.2.1). The α-helix has a spiral arrangement of the peptide backbone with 3.6 amino acid residues per turn. The α-helix pitch is 0.54 nm, the torsion angles φ = 57˚, ψ = 47˚. It is stabilized by intramolecular hydrogen bonds aligned parallel to the helix axis, and directed backwards from C-terminal NH to a N-terminal C=O. Hydrogen bonds are formed between the carbonyl group of the n-th residue and the amino group of the n+4 residue. The regular arrangement of peptide bonds results in an excess of partially positively charged amide nitrogen atoms near the amino-terminus of a helix and partially negatively charged oxygen atoms near the carboxy-terminus. The aggregate charge separation is termed the helix dipole, and it destabilizes the helix. The compensating charge of an appropriate side chain can stabilize the helix, *e.g.*, glutamate at the amino-terminus or lysine at the carboxy-terminus. Some proteins use the helix dipole to stabilize the binding of charged ligands.

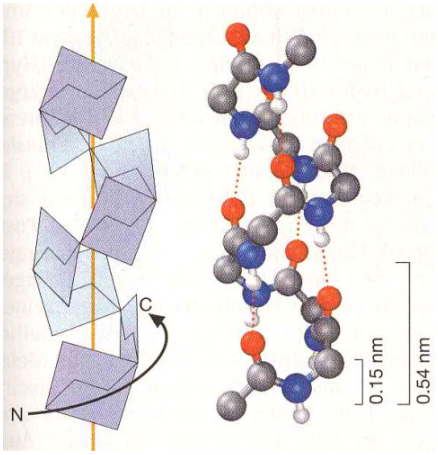

Figure 2.2.1. *Model of right handed α-helix. Carbons are marked by grey colour, Oxygens by red Nitrogen by blue and Hydrogenes by white colour. Hydrogen bonds denoted by red dots.*

The nature of amino acid side chains is important for helix stability. The amino acids proline and hydroxyproline have no available proton to form the hydrogen bonds. Therefore they display helix-breaking properties. Proline is usually found in the kink between α-helices. Correct placement of hydrophilic and hydrophobic residues within an amino acid sequence promotes the formation of amphipatic helices. Interactions of these helices with other parts of the protein (peptide) or with a lipid membrane stabilize the structure. For example, the small peptide mellitin is present in a monomeric form at low concentrations in aqueous media of low ionic strength, where it has a random coil conformation. However, at the lipid interface it adopts a helical conformation.

β-sheet

The β-sheet hydrogen-bond pattern differs fundamentally from that of the helical structure. In a β-sheet, hydrogen bonds are formed between two neighboring polypeptide chains. There are two major types of β-sheets: parallel β-sheet (figure 2.2.2) and antiparallel one (figure 2.2.3)

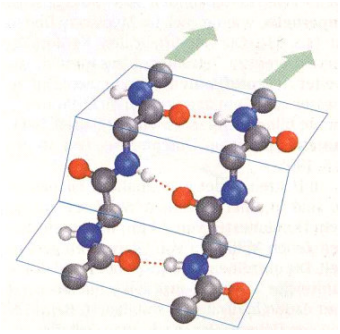

Figure 2.2.2. *Model of a parallel β-sheet [17]*

The parallel β-sheet is characterized by two peptide strands running in the same direction held together by hydrogen bonding between the strands. Torsion angles of parallel β-sheet are φ = - 119˚ and ψ = 113˚. Hydrogen bonds create so called hydrogen-bond rings. In parallel β-sheets the rings consist of 12 atoms. In β-sheet structures only half of the groups, which can potentially form hydrogen bonds, participate in the interactions with a neighbouring strand. Therefore, β-sheets usually consist of more than two strands.

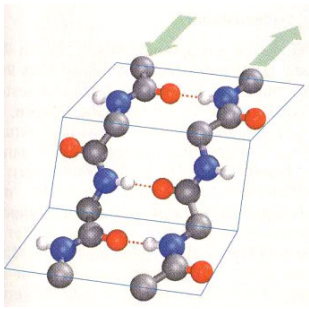

Figure 2.2.3. *Model of an antiparallel β-sheet [17].*

In the antiparallel β-sheet two neighboring chains are running in opposite directions (from N-terminal to C-terminal). The antiparallel β-sheet structure displays torsion angles φ = - 139˚ and ψ = 135˚. One can recognize an antiparallel β-sheet by the number of atoms in the hydrogen-bonded rings. The number of atoms in hydrogen bonded rings alternates between 14 and 10 in an antiparallel β-sheet. Hydrogen bonds in an antiparallel β-sheet are linear unlike parallel β-sheet. For this reason antiparallel β-sheets are more stable than parallel.

The average length of a β-sheet is about six residues and most β-sheets contain less than six strands. However, they can form extremely elongated structures in amyloid fibrils. The β-sheet structure is much more complex than a simple ribbon diagram may display. β-sheets occur in a twisted, curled or back-folded form. Side chains from adjacent residues of a strand in a β-sheet are found on opposite sides of the sheet and do not interact with one another. Therefore, like α-helices, β-sheets have the potential for amphiphilicity with one face polar and the other apolar.

Turns

Loops of polypeptide chains are characterized by an inversion of the chain direction. The characteristic secondary structure of loops is the inverse turn. Turns are necessary for globule

formation of proteins, they are also found in small peptides. They often occur on the exposed surface of proteins and play therefore a significant role in immune recognition. Often they are stabilized by a hydrogen bond between an amino group located C-terminally and a carboxy group located N-terminally. Turns are classified according to the number of amino acids involved, for example γ-turns formed by tree amino acids, β-turns by four, α-turns by five and π-turns by six amino acids. The most common is a β-turn. β-Turn can be further classified according to the characteristic dihedral angles φ and ψ of the second and third amino acid. Some amino acids have a high tendency to be located in the turns. Proline is often found in a reverse turn and glycine often occurs in the second and third position of β-turns.

3. Materials and methods.

3.1 Materials

Phospholipids: 1,2-Dimyristoyl-sn-glycero-3-phosphoethanolamine (DMPE) and 1,2-dipalmitoyl-sn-glycero-3-phosphoethanolamine (DPPE), 1,2-dimyristoyl-sn-glycero-3-phosphocholine (DMPC), 1,2-dipalmitoyl-sn-glycero-3-phosphocholine (DPPC), 1,2-dimyristoyl-sn-glycero-3-[phospho-rac-(1-glycerol)] sodium salt (DMPG), 1,2-dipalmitoyl sn-glycero-3-[phospho-rac-(1-glycerol)] sodium salt (DPPG) and 1,2- dimyristoyl -sn-glycero-3-phosphate monosodium salt (DPPA) were purchased from Sigma with purity of 99% and used as received. Ganglioside G_{M1} from ovine brain, 1,2-dipalmitoyl-3-trimethylammonium-propane chloride (DPTAP) and 1,2-distearoyl-3-trimethylammonium-propane chloride (DSTAP), 1,2-dipalmitoyl-sn-glycero-3-[phospho-L-serine] sodium salt (DPPS), 1-palmitoyl-2-oleoyl-sn-glycero-3-[phospho-rac-(1-glycerol)] sodium salt (POPG) and 1-palmitoyl-2-[6-[(7-nitro-2-1,3-benzoxadiazol-4-yl)amino]-dodecanoy]- sn-glycero-3-phosphocholine (NBD-PC) were purchased from Avanti Polar Lipids (USA) with purity of 99 % and used as received. They were spread onto the air/water interface from a 10^{-3} M methanol (Sigma)/ chloroform (Baker) (1/3 v/v) solution. Chemical structures of these lipids are shown in Appendix 2.

The Amyloid β (1-40) peptide (Aβ) was obtained from Bachem (Switzerland) as a TFA (trifluoroacetic acid) salt with the purity of ~90 %. The amino acid sequence is as follows: **DAEFRHDSGYEVHHQKLVFFAEDVGSNKGAIIGALMVGGVV**, the molecular weight is 4329.9 g/mol. The peptide was first dissolved in hexafluoroisopropanol (HFIP) (Sigma, Germany) to destroy possible aggregates and stored in a refrigerator [18]. Before measurements, HFIP was evaporated under a nitrogen stream and the peptide was dissolved in water or aqueous solutions with various pHs. The secondary structure of the peptide was checked using circular dichroism (CD) spectroscopy (Jasco J-715, Japan). The peptide was found to have predominantly random coil conformation in water or buffer at pH 2-4 and 7-12 after such a pre-treatment and it forms β-sheet structure at pH between 4 and 6.

The peptide B18 (**LGLLLRHLRHHSNLLANI**), representing amino acids 103-120 of the mature *Strongylocentrotus purpuratus* bindin sequence with molecular weight of 2098 g/mol, was kindly provided by Dr. Olaf Zschoernig from Institute of Medical Physics and Biophysics, University of Leipzig. The peptide was synthesized by standard Fmoc protocols and purified

using HPLC. Purity of the B18 was proved by mass spectroscopy. The preparation and characterization of B18 was described earlier [19-21]. The peptide stock solution (c = 1 mg/ml) was prepared by dissolving it in water, giving pH ~4 and stored in the refrigerator, then it was diluted to the appropriate concentration with water or buffer at pH 7,4 (see below). For CD experiments with lipid vesicles the B18 was treated with HFIP that was evaporated under nitrogen stream.

Cesium chloride (Fluka, Switzerland) 99% purity, potassium chloride, sodium chloride and lithium chloride (Merck, Germany) 99% purity were used to adjust the ionic strength of the aqueous solutions to 0.1 and 0.01 M. The pH of solutions was adjusted with sulphuric (95-98% diluted to 1 M), hydrochloric (1 M), acetic (1 M) and phosphatic acid (30%, diluted to 1 M) obtained from Merck, Germany and cesium (Sigma, Germany), potassium (Merck, Germany), sodium (Merck, Germany) and lithium (Fluka, Switzerland) hydroxides. $5*10^{-4}$ M EDTA (Sigma, Germany) was added to solutions in order to avoid influence of possible impurities of polyvalent cations. For peptide solutions only sodium and potassium chlorides and hydroxides were used. Aβ was dissolved in different subphases: 0.01 mM hydrochloric acid for pH 2, 0.01 mM phosphoric acid for pH 3, 0.1 mM ammonium acetate/acetic acid for pH 4 and 5, 0.1 M hepes (Roth, Germany, 99% purity)/sodium hydroxide, 0.1 M Tris (Sigma, Germany, 99 % purity) /HCl and 0.1 M sodium dihydrophosphate (Merck, Germany, 99 %) /KOH for pH 7.4, ammonium hydroxide and sodium hydroxide for pH 10. Buffer with 0.01 M hepes/NaOH, 0.1 M NaCl, pH 7.4 was used to prepare B18 solutions. All solutions were prepared using Milli-Q deionized water (resistivity of >18.2 MΩcm).

DMPC and DMPG vesicles were prepared as follows: 10 mg of DMPG and 10 mg of DMPC were dissolved in 0.5 ml cloroform/methanol 3:1, then the solvent was evaporated under nitrogen stream and dried in vacuum for 3 hours. The dry lipid film was dispersed in 1ml of water or buffer at pH 7.4 (0.01 M hepes/sodium hydroxide) by using vortex and then sonicated for about 15 minutes at ~10ºC until an almost transparent solution was obtained. The lipid stock solution (concentration of $1.5*10^{-2}$ M) was diluted to appropriate concentrations and added to a dried peptide (after HFIP pre-treatment) and then again vortexed.

All measurements were carried out in PTFE Langmuir troughs. The surface pressure was controlled by a Wilhelmy microbalance using a filter paper plate. Three different set-ups were used to adsorb peptides to the lipid monolayer or to the air/water (buffer) interface. In the first procedure, the lipid was spread onto the freshly cleaned surface of a subphase containing peptide

in various concentrations. In the other experiments, the peptides were injected into the subphase beneath the phospholipid monolayer, which was compressed to 30 mNm^{-1}. To obtain the adsorption kinetic isotherms of peptides a specially constructed Langmuir trough was used. The trough has two compartments: the lipid monolayer was formed on pure water (buffer) and compressed to a certain lateral pressure (lateral density) in the first compartment and then transferred to the other compartment containing the peptide solution.

3.2 Methods

3.2.1. CD-spectroscopy

Circular dichroism (CD) spectroscopy was applied to determine the conformation of peptides [22]. CD spectra of peptide solutions were recorded on a Jasco J-715 (Japan) spectrometer. The wavelength interval used extends from 185 for pure water and HFIP or 190 nm for buffers (Hepes or potassium phosphate, pH 7.4) and lipid vesicles to 260 nm. The cuvettes path length was either 1 mm or 0.5 mm, peptide concentration 0.2-0.4 mg/ml. The data was obtained after accumulation of 4-10 measurements with response of 2 to 4 s and a bandwidth of 1 nm and data pitch of 0.2 nm. The measured CD signal was then transformed to the molar ellipticity – $[\theta]$. The blank spectra of pure subphase (water, HFIP, buffer) were subtracted.

CD-spectroscopy is based on the difference in absorption of right and left circularly polarised light (A_R and A_L, respectively) by optically active molecules. This difference in absorption is called circular dichroism. The molecules are optically active if they cannot be superimposed on their mirror image. The circularly polarized light passed through an optically active substance is then transformed into elliptically polarised light. A parameter called ellipticity, θ is often used to describe the elliptical polarization. In CD-spectroscopy one uses the molar ellipticity that is the difference in absorption coefficients for right and left polarized light and is given by the equation:

$$[\theta]_\lambda = 3298 \cdot (\varepsilon_R - \varepsilon_L),$$

where ε_R and ε_L are molar absorption coefficients of a chromophore for right and left circularly polarized light.

In peptides and proteins the major optically active groups are the amide bonds and aromatic side chains. Peptides and proteins have regions where these chromophores are in highly ordered arrays, such as α-helix and β-sheets. Depending on the orientation of the peptide bonds

in the arrays, the optical transitions of the amide bond can be split into multiple transitions, the wavelengths of the transitions can be increased or decreased, and the intensity of the transitions can be enhanced or suppressed. As a consequence, many common secondary structure motifs, such as the α-helix, β-sheet and β-turn have very characteristic CD-spectra (Fig. 3.2.5.) For example, α-helices display large CD bands with negative ellipticity at 222 and 208 nm, and a positive band at 193 nm, β-sheets exhibit a broad negative band near 218 nm and a large positive band at 195 nm, while disordered chains have a weak positive or negative band near 217 nm and a large negative band near 200 nm. The peptide or protein spectrum is in principle the sum of its conformation elements.

There are many methods to extract protein conformation in solution from CD data in literature [23, 24]. However, all of them have advantages and drawbacks. The choice of a method better suited to the sample depends on many factors: amount of aromatic amino acids that can contribute to the CD-spectrum, length of the helix, amount of unstructured component etc. In the present work two methods were chosen: multilinear regression (MLR) and ridge regression analysis (Contin ll).

In the MLR the experimental data is fitted to the spectra of standards by the method of least squares. The MLR is a non-constrained least-squares analysis and is the only method, which can be used to estimate the conformation when the peptide or protein concentration is not known precisely. The last is important for samples containing vesicles or aggregated peptide since light scattering or precipitation can reduce the CD-signal intensity. Using the spectra of the polypeptide models suggested by Brahms and Brahms as standards [25], the method gives a reasonable estimate of α-helical component, and there is some correlation between estimated and found amount of β-sheet structure, but the estimation of β-turn is very poor. The method is adequate to indicate whether organic solvents, membranes, or ligands increase or decrease the helicity of a peptide or protein.

The Contin ll method, developed by Provencher and Glöckner [26] and improved by Sreerama and Woody [27], uses the ridge regression procedure, which fits the spectrum of a test protein or peptide as a linear combination of the spectra of a large data base of proteins with known conformation. The method still suffers, however, in that the fits depend on the choice of proteins in the database of standards. Since the peptide studied in the present work are short compared to proteins and are not well ordered, we have used the database that contains spectra of denaturated proteins.

The analysis of CD-spectra was performed with CDPro and CD softwares.

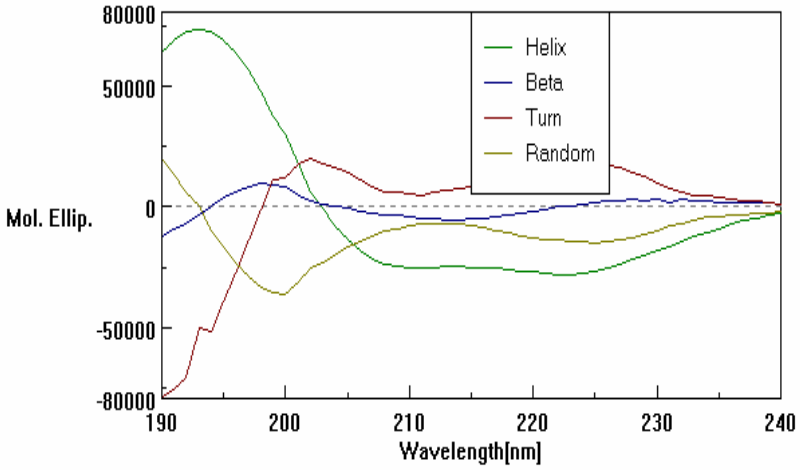

Figure 3.2.1. *The reference spectra for pure α-helix, β-sheet, random coil and turn used in the Jasco secondary structure estimation program.*

3.2.2. Fluorescence microscopy

Fluorescence microscopy [2] (Zeiss, Germany) was applied to visualize the formation of condensed phase domains in the liquid phase during compression of the lipid monolayer or during peptide adsorption to it. Fluorescence microscopy images were obtained by introducing the fluorescence dye – NBDPC (1mol%) in the monolayer. For excitation a mercury lamp (HBO 50 W) was used. The light emitted from the monolayer is collected by an objective lens, selected by a filter in the range of 450-490 nm and directed either onto the objective of the microscope or to the low light level camera.

Because lipid molecules have no fluorescent groups, a fluorescent probe can be incorporated into the lipid monolayer and the lateral dye distribution can be determined from the analysis of fluorescence microscope images [2]. When a monolayer undergoes a phase transition from liquid expanded to condensed phase, one obtains a pattern with distinct textures [28]. Usually small dark uniform spots (domains) appear in the coexistence region. The domains increase in size during compression. In this case the observation of domains is possible owing to the different dye solubility in the liquid expanded and condensed phases of the lipid monolayer with bright areas representing the liquid phase (high dye solubility in the monolayer) and dark domains corresponding to the condensed phase (low dye solubility). In the majority of cases, domains grow far from equilibrium and the growth can be understood as diffusion limited aggregation process that may lead to fractal structures.

3.2.3. GIXD

Synchrotron grazing incidence X-ray diffraction (GIXD) measurements were carried out at 20 °C using the liquid-surface diffractometer on the undulator beamline BW1 of HASYLAB, DESY (Hamburg, Germany). The experimental set-up was described elsewhere [29, 30]. The Langmuir film balance was thermostated (20 ºC) and placed into a hermetically closed container filled with helium. The monochromatic beam (λ = 1.3038 Å) strikes the monolayer surface at an angle of incidence $\alpha_i = 0.85\ \alpha_c$, where $\alpha_c \sim 0.13^o$ is the critical angle for total external reflection, and illuminates only the top 80 Å beneath the water surface, thus enhancing the surface sensitivity and reducing the background scattering. The intensity of the diffracted beam was detected with a linear position sensitive detector (OEM-100-M, Braun, Garching, Germany) as a function of the vertical scattering angle α_f. A Soller collimator was located in front of the detector. The in-plane (horizontal) scattering angle 2Θ was varied by rotation of the entire assembly (detector and Soller collimator). The experimental set-up is sketched in figure 3.2.2.

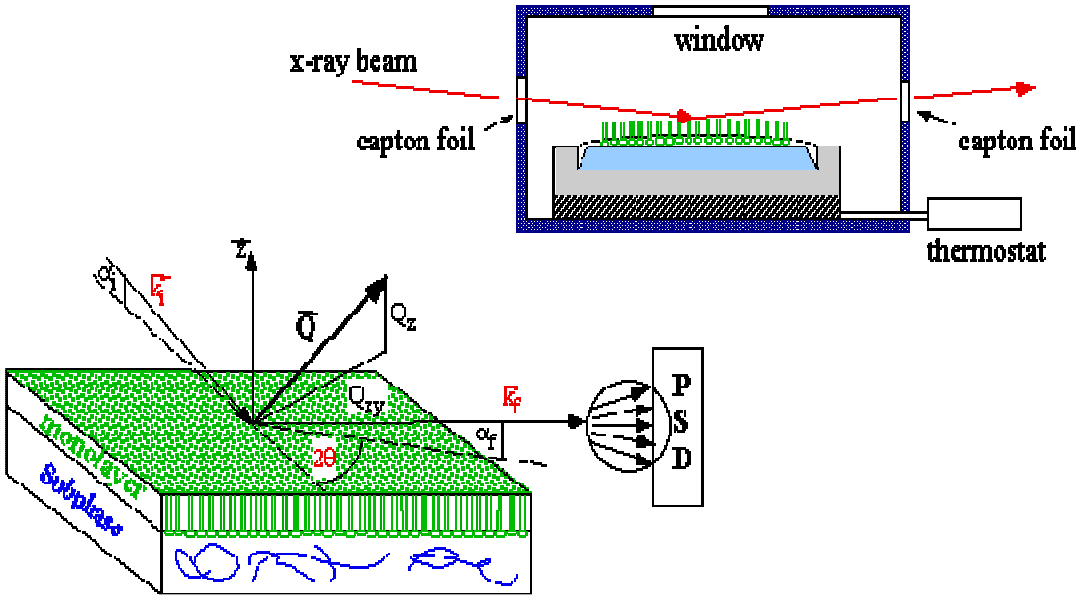

Figure 3.2.2. *Schematic representation of GIXD set-up in undulator beamline BW1 Hasylab, Desy (Hamburg).*

The horizontal- (Q_{xy}) and vertical (Q_z) components of the scattering vector can be given by equations:

$$Q_{xy} \approx \frac{4\pi}{\lambda}\sin\frac{2\Theta}{2} \qquad (3.2.3.1a)$$

$$Q_z \approx \frac{2\pi}{\lambda}\sin\alpha_f \qquad (3.2.3.1b)$$

where λ is the X-ray wavelength. The accumulated position-resolved counts were corrected for polarization, effective area, and Lorentz factor. Model peaks taken as a Lorentzian in the in-plane direction and a Gaussian in the out-of-plane direction, respectively, were least-square fitted to the measured intensities. The full width at half maximum (*FWHM*) of the peak taken in the in-plane direction is related to the correlation length l [31]:

$$l = 2/FWHM, \qquad (3.2.3.2)$$

where *FWHM* is determined from the measured value $FWHM_{mes}$ by deconvolution with the resolution $FWHM_{res}$ ($FWHM = \sqrt{FWHM_{mes}^2 - FWHM_{res}^2}$). The peaks taken in the out-of plane direction are called Bragg rods and their width is inversely proportional to the length of the molecule. From the peak positions of the horizontal (in-plane) diffraction data, the lattice spacing can be determined as

$$d(hk) = \frac{2\pi}{Q_{xy}^{hk}} \qquad (3.2.3.3)$$

where (h, k) indicates the reflection order. The lattice parameters *a, b*, and the angle γ, can be estimated from the lattice spacings *d*(*hk*), leading to the area per unit cell A_{xy}:

$$A_{xy} = a \cdot b \cdot \sin\gamma\,. \qquad (3.2.2.4)$$

Amphiphilic molecules can pack only in a limited number of crystalline lattices: hexagonal, orthorhombic and oblique (figure 3.2.2.1b). In a hexagonal lattice, the chains are usually oriented normal to interface (not-tilted phase) with lattice parameter a = b and γ = 120º.

When monolayers form an orthorhombic (distorted hexagonal) lattice, the chains can be tilted in a symmetry direction either towards the nearest (NN) or the next-nearest (NNN) neighbor. Only two Bragg peaks are detected. The tilt angle *t* can be calculated by:

$$\tan t = \frac{Q_z^d}{\sqrt{\left(Q_{xy}^d\right)^2 - \left(Q_{xy}^n/2\right)^2}} \qquad \text{if } Q_z^n = 0\text{, or} \qquad (3.2.2.5a)$$

$$\tan t = \frac{Q_z^n}{Q_{xy}^n} \qquad \text{if } Q_z^n \neq 0\,. \qquad (3.2.3.5b)$$

For the oblique structure (intermediate tilted phase) with three distinct diffraction peaks, the tilt *t* can be given more generally by:

$$Q_z^{(h,k)} = Q_{xy}^{(h,k)} \cdot \cos\left(\psi_{(h,k)}^*\right) \cdot \tan t \qquad (3.2.3.6)$$

with $\psi_{(h,k)}^*$ as the tilt azimuth between the tilt direction and the reciprocal lattice vector. Using the obtained tilt angle *t*, the cross-sectional area per chain A_0 can be calculated from the area per chain in the water plane:

$$A_0 = A_{xy} \cdot \cos t \,. \qquad (3.2.3.7)$$

Since in phospholipids two chains are covalently bound to the glycerol backbone the area occupied by a molecule (A) is a double A_{xy}.

3.2.4. X-ray reflectivity

The specular x-ray reflectivity measurements were performed with the same instrument, as GIXD experiments on the undulator beamline BW1 at HASYLAB, DESY (Hamburg) [32-34]. Figure 3.2.3.1 schematically depicts the scattering geometry of the sample. For reflectivity measurements the angles of incident α_i and reflected α_f beam are equal and varied in a range $0.5\alpha_c < \alpha_i(\alpha_f) < 30\alpha_c$, where α_c = 0.13º. The reflected intensity is measured with a NaI scintillation detector in the plane of incident beam as a function of out-of-plane scattering vector Q_z.

In the case of an ideally sharp interface between vapor and liquid the reflectivity ($R_f(Q)$) is simply a Fresnel reflectivity. A monolayer film of thickness d modulates the reflectivity at wave-vectors of the order of π/d and beyond. The measured reflectivity (R), divided by Fresnel Reflectivity is given by the master formula [35]:

$$\frac{R}{R_f} = \frac{1}{\rho_w^2}\left|\rho'(z) \cdot e^{iQ_z z} dz\right|^2,$$

where ρ_w is the electron density of water, ρ' is the electron density gradient along the normal wave vector transfer Q_z (see equation 3.2.3.1b). In reality the interface between two phases is not mathematically sharp. The molecular roughness, σ, is in the order of 3 Å and stems mainly from thermally excited capillary waves on the water surface. It leads to a Debye-Waller factor exp ($-Q_z^2\sigma^2$) in the master formula.

The direct Fourier inversion of the reflectivity into the electron density distribution is not possible, because one measures the absolute square of a complex number and not the phase. For this reason the measured reflectivity curve has to be fitted by a model density profile with a certain number of adjustable parameters. Two different approaches are used to fit reflectivity

data: the so called Box model [32].

In the Box model the Langmuir monolayer is considered as two boxes representing aliphatic chain region (tails) and head group (head) with constant electron densities. The model contains 5 adjustable parameters: two box heights (densities), two box width (length of the segments) and an overall smearing parameter (roughness). This model describe satisfactorily the tail region however it suffers in the determination of the head group orientation and hydration.

3.2.5 IRRAS

IRRAS-spectra have been recorded on the IFS 66 FT-IR spectrometer (Bruker, Germany) equipped with a liquid nitrogen-cooled MCT detector. The IR beam was conducted out of the spectrometer and focused onto the water surface of the Langmuir trough. The angle of incidence can be varied from 25° to 90° with respect to the surface normal and the IR beam was polarized by a BaF_2 polarizer in the plane of incidence (p) or perpendicular to this plane (s). Measurements were performed with a trough containing two compartments using a trough shuttle system [36]. One compartment contained the monolayer system under investigation (sample), whereas the other (reference) was filled with pure water (buffer). The spectra from the reference were subtracted from the sample spectra in order to eliminate the water vapor signal. To maintain a constant water vapor content the set-up was placed in a sealed container. FTIR spectra were collected at 8 cm^{-1} resolution using 200 scans for s-polarized light and 400-800 scans for p-polarized light.

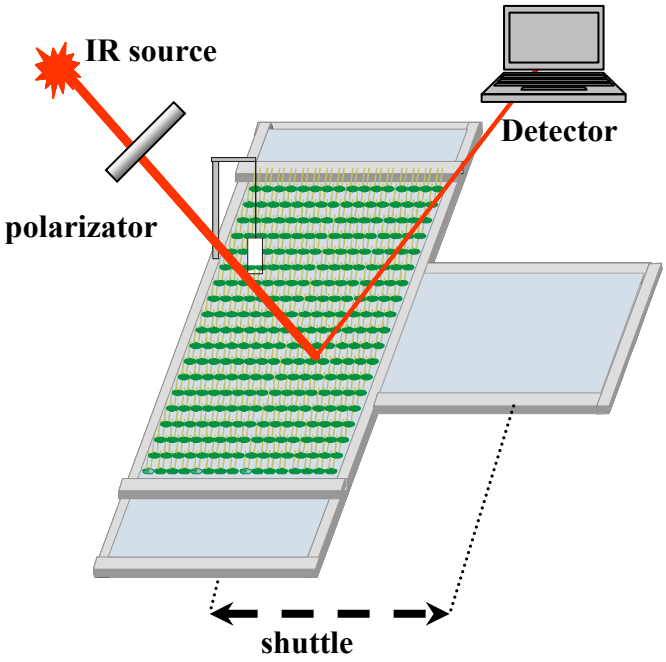

Figure 3.2.3. *Schematic representation of the IRRAS set-up.*

Infrared spectroscopy of lipids and peptides

Infrared spectroscopy is a useful technique for the determination of conformation and orientation of proteins and peptides associated with lipid membranes [37, 38]. It allows detecting the influence of different lipid structure on peptides or proteins, and vise versa, since vibrational

modes of both, lipids and peptides, are present in the same IR spectrum. Modern Fourier-Transformed Infrared (FTIR) spectrometers are sensitive enough to measure the infrared (IR) spectrum of Langmuir monolayers of lipids with adsorbed and penetrated peptides [39-43].

Although the IRRA spectrum contains much information, assignment of each band to a certain chemical bond is complicated. Additionally water vibrations contribute in the IRRAS. A typical IR spectrum of a phospholipid monolayers with adsorbed peptide is shown on Figure 3.2.4. It contains few characteristic bands: CH_2 stretching and scissoring vibrations, which are sensitive to the monolayer state and structure, C=O and PO_2^- stretching, which display the hydration level of phospholipids, amide A, I, II and III of peptides and proteins reveal their secondary structure. The common band positions are summarized in Table A2 in Appendix 2.

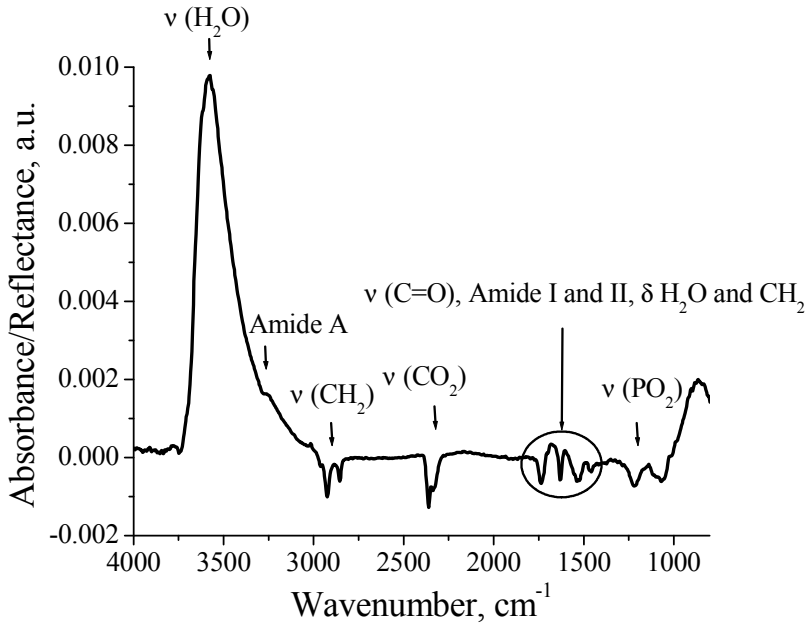

Figure 3.2.4. *A typical IRRA spectrum of a phospholipid monolayer with adsorbed peptide.*

The methylene (CH_2) stretching vibrations are sensitive to the conformational order of hydrocarbon chains [44, 45]. The CH_2 symmetrical and asymmetrical stretching modes shift from 2854 and 2924 cm^{-1} to approximately 2849 and 2919 cm^{-1}, respectively, upon a transition from liquid to condensed state. The frequencies of these bands are sensitive to the formation of gauche rotamers in the chain. In the liquid phase they can be formed, whereas in the condensed phase chains have to be in all-trans conformation. Another important CH_2 vibrational mode is the CH_2 scissoring near 1470 cm^{-1}. This mode splits into two components when chains form an

orthorhombic lattice and remains as a single peak in hexagonal and triclinic phases or in a disordered phase (liquid) [46].

The C=O stretching mode of lipid ester groups depends on the hydration and hydrogen bonding [47]. This band is a result of superposition of at least two components at around 1723-1728 and 1740-1742 cm^{-1}. The higher frequency band (~1742 cm^{-1}) can be assigned to the non-hydrogen bonded C=O vibration, while the lower frequency component results from the hydrogen bonded C=O. The higher frequency component intensity increases in the gel phase of phospholipid dispersions indicating a lower hydration level of the head group comparing to the hydration in the liquid crystalline phase. The tighter packing of DMPE aliphatic chains, compared with DMPC leads to the lower head group hydration and therefore to the increasing intensity of the C=O band [47]. Similar results are obtained for the DPPG monolayer [48]. The higher frequency component progressively grows with compression of the film from 0 to 40 mN/m. It was also found that the tighter packed DPPA monolayer is much less hydrated than the loosely packed DPPC [49].

The phosphate vibrations are also extremely sensitive to hydration and hydrogen bonding. Furthermore, they can provide information about the charge of phospholipids. Arondo and Gorni [50] assign three absorption bands to the phosphate group of DPPC (1222, 1086 and 1060 cm^{-1}). These values are similar above and below the phase transition temperature. The asymmetrical and symmetrical PO_2^- stretching modes at around 1222 and 1086 cm^{-1}, respectively, are shifted toward higher wavenumbers (1245 and 1091 cm^{-1}) upon a dehydration process. The symmetrical phosphate stretching mode is almost not changing for different phospholipids. On the contrary the asymmetrical PO_2^- stretching mode differs for various phospholipids [47]. The high degree of hydrogen bonding shifts this band position to lower wavenumbers in the case of phosphatidylglycerol and phosphatidic acid (1216 and 1180 cm^{-1}, respectively). Zwitterionic lipids hardly respond to the change in the subphase composition, however anionic lipids can be protonated at low pH, they interact differently with mono- and divalent cations. It was found that Ca^{2+}as well as Sr^{2+} induce the double negative charge in the phosphatidic acid. Laroche et al [51] attribute bands at ~1080 and ~1000 cm^{-1} to the asymmetrical and symmetrical PO_3^{2-} stretching vibrations.

The peptide group, the structural repeat unit of the protein “backbone”, gives rise to nine characteristic infrared bands. Only three of them are intense enough to be discussed in the present work. Amide A occurs in the 3200-3300 cm^{-1} region and essentially ~95% of the intensity is due

to the amide stretching mode (ν_{N-H}). This mode does not depend on the chain conformation but is very sensitive to the strength of the hydrogen bond [52]. It shifts towards higher frequency when the length of the hydrogen bond increases. Interaction with the overtones of amide II mode further disturbs the frequency of Amide A. The Amide A band position is higher for α-helix (3305 cm^{-1}) than for β-sheet (3230-3275 cm^{-1}). Amide I is the most intense adsorption band of proteins and peptides. Amide I is found between 1700 and 1600 cm^{-1}, but its frequency is determined by the geometry of the polypeptide chain and hydrogen bonding. The major component of this band is the C=O stretching of amide bonds. It accounts for 70-85 % of the potential energy. The rest is C-N stretching (10-20%) and C-CN deformation (~10%). Amide II occurs in the 1510-1580 cm^{-1} region. It is conformation sensitive, although its interpretation is difficult since it is too complex. Amide II derives mainly from the in-plane N-H bending (40-60%). The residual potential energy arises from C-N stretching (18-40%) and C-C stretching (~10%).

The mean frequency of α-helical peptides was found to be 1652cm^{-1} for the main component of Amide I and 1548 cm^{-1} for the main component of Amide II [38]. Nevskaya and Chirgadze [53] investigated the effect of the helix length on the Amide I frequency. They predicted the Amide I band at 1653 cm^{-1} for infinite α-helix, it shifted to 1658 cm^{-1} for 14-16 residues, 1660 cm^{-1} for 11-13 residues, 1663 cm^{-1} for 8-10 residues, 1668 cm^{-1} for 5-7 residues and 1678 cm^{-1} for 1-4 residues. The Amide II frequency is not affected if the number of residues is above 6. The Amide I and II bands of random coil occurs at the same wavenumbers as α-helix, however it is broader and less intense compared with the helix [54].

In contrast, the β-sheet structure has unique Amide I frequency. It appears at lower wavenumbers and splits into at least two components. The splitting can be explained by the transition dipole coupling between nearest and next nearest neighbor peptide groups [55, 56]. The Amide I frequencies are essentially independent of the amino acid sequences, its hydrophobicity, size and charge. The most pronounced splitting of the Amide I band with the lowest frequency (B2) maximum is predicted to multistrained β-sheet. For the antiparallel β-sheet, the average frequency of component B2 is 1629 cm^{-1} and 1696 cm^{-1} for the other component (B1). The later is ten fold weaker than the B2 component. Parallel and twisted β-sheets are predicted to have significantly smaller Amide I splitting with the higher frequency for the lower component [57]. The splitting of Amide I depends on the chain length and number of strains in the sheet [55, 56].

For two antiparallel chains, a gradual decrease of the main adsorption band (B2) frequency of ~ 8 cm^{-1} occurs when the chain length increases from 2 to 25 amino acid residues with no change in the splitting. The increasing number of chains in the sheet from two to seven drastically decreases the frequency of the B2 component and increases the splitting.

In contrast to the α-helix and β-sheet, turns are not as conspicuous since backbone torsion angles are not repeating in the polypeptide chain. Nevertheless turns are regular structures, which are often exposed to the solvent and are thought to be important sites for enzymatic reactions. The β-turns usually occur in the 1660-1680 cm^{-1} region of Amide I and overlap both, β-sheet and α-helical regions of Amide II. The triflouroacetic acid is a common solvent in the peptide synthesis and preparation. It absorbs in the same region as turns [38].

Interpretation of the peptide infrared spectra sometimes requires considering the side chain absorption contribution in the 1700-1500 cm^{-1} region [58]. Aspartic and glutamic acids absorb in this region due to the carboxilate group, giving rise to a band at ~1715 cm^{-1} in the protonated form (ν of COOH) and at 1560-1574 cm^{-1} for the deprotonated form (ν_{as} of COO^-). Asparagine and glutamine absorb at 1678 cm^{-1}(ν of C=O), 1622 cm^{-1} (δ of NH_2) and 1670 cm^{-1} (ν of C=O), 1610 cm^{-1} (δ of NH_2) respectively. Positively charged arginine gives bands at 1673 and 1633 cm^{-1} (ν_{as} and ν_s of $CN_3H_5^+$). Lysine absorbs at 1629 and 1526 cm^{-1} (δ_{as} and δ_s of NH_3^+). Tyrosine in protonated state absorbs at 1518 cm^{-1} and in the deprotonated state at 1602 cm^{-1}.

The infrared reflection absorption spectra (IRRAS) can be acquired with p-polarized radiation. This allows determining the orientation of the particular chemical bond at the interface. The successful determination of the aliphatic chain tilt angle at the air/water interface as well as orientation of α-helix and β-sheet at the interface was achieved in recent years [43, 59-61].

Determination (Simulation) of the dipole moment orientation

There are several theoretical approaches describing the dependence of the IRRAS band intensities from the incident angle and transition dipole moment orientation. In the present work, the mathematical model of Kuzmin et al. [62, 63] developed by Mendelsohn et al. [40] for monolayers at the air/water interface is used. Briefly for s-polarization:

$$\underline{\underline{r_s}} = \frac{\sin\left(\theta - \underline{\underline{\phi}}\right) - ik_0 \underline{\underline{n}}_2^{-1} \sin\theta \underline{\underline{I}}_1}{\sin\left(\theta + \underline{\underline{\phi}}\right) - ik_0 \underline{\underline{n}}_2^{-1} \sin\theta \underline{\underline{I}}_1} \qquad (3.2.5.1a)$$

for p-polarization:

$$\underline{\underline{r_p}} = \frac{\sin\left(\theta - \underline{\underline{\phi}}\right)\cos\left(\theta + \underline{\underline{\phi}}\right) - ik_0 \underline{\underline{n}}_2^{-1} \sin\theta\left(\underline{\underline{I}}_1 \cos\theta\cos\underline{\underline{\phi}} - \underline{\underline{I}}_2 \sin\theta\sin\phi\right)}{\sin\left(\theta + \underline{\underline{\phi}}\right)\cos\left(\theta - \underline{\underline{\phi}}\right) - ik_0 \underline{\underline{n}}_2^{-1} \sin\theta\left(\underline{\underline{I}}_1 \cos\theta\cos\underline{\underline{\phi}} + \underline{\underline{I}}_2 \sin\theta\sin\phi\right)} \qquad (3.2.5.1b)$$

where θ is the angle of incidence between the incoming ray and the direction of the surface normal and $\underline{\underline{\phi}}$ is the complex angle of the refracted ray. In which

$$\underline{\underline{I}}_1 = \int \left(\underline{\underline{n}}_x^2(z) - \underline{\underline{n}}_2^2\right)dz = \left(\underline{\underline{n}}_x^2 - \underline{\underline{n}}_2^2\right)d \qquad (3.2.5.2a)$$

$$\underline{\underline{I}}_2 = \int \frac{\left(\underline{\underline{n}}_z^2(z) - \underline{\underline{n}}_2^2\right)}{\underline{\underline{n}}_z^2(z)}dz = \frac{\left(\underline{\underline{n}}_z^2 - \underline{\underline{n}}_2^2\right)}{\underline{\underline{n}}_z^2}d \qquad (3.2.5.2b)$$

and

$$k_0 = \frac{2\pi}{\lambda} \qquad (3.2.5.3)$$

d - is the film thickness and $\underline{\underline{n}}_x$, $\underline{\underline{n}}_z$ are the complex refractive indices of the film.

Calculation of single band intensities requires the following parameters: angle of incidence, θ; mean tilt angle of the molecular axis relative to the surface normal, τ; twist angle of the molecule, angles between transition dipole and molecular axis, α and β; wavelength of the light in vacuum λ; film thickness, d; refractive indices and extinction coefficients of the incident and final phases, n_0, n_2, k_0, k_2; and directional refractive indices and extinction coefficients of the film, n_x, n_z, k_x, k_z.

To simulate an entire band a Lorentzian or Gaussian distribution is assumed for the wavenumber (ν) dependence of the film extinction coefficients and refractive indices:

$$n_x(\nu) = n_{x\max} - \frac{2\Delta k_{x\max}\gamma}{4\Delta^2 + \gamma^2} \qquad (3.2.5.4a)$$

$$n_z(\nu) = n_{x\max} - \frac{2\Delta k_{z\max}\gamma}{4\Delta^2 + \gamma^2} \qquad (3.2.5.4b)$$

$$k_x(\nu) = \frac{\Delta k_{x\max}\gamma}{4\Delta^2 + \gamma^2} \qquad (3.2.5.5a)$$

$$k_z(\nu) = \frac{\Delta k_{z\max}\gamma}{4\Delta^2 + \gamma^2} \qquad (3.2.5.5b)$$

where $\gamma = 2\pi c(FWHH)$, $\Delta = 2\pi c\left(\nu - \nu_0\right)$, FWHH is the full width at half height, c is the speed of light, ν_0 is the center frequency for which the calculation is being made.

When the mean tilt angle of a molecular axis relative to the surface normal is τ, then:

$$n_x = n_y = n_{ext} \sin^2 \tau + n_{ord} \cos^2 \tau \quad (3.2.5.6a)$$

$$n_z = n_{ext} \cos^2 \tau + n_{ord} \sin^2 \tau \quad (3.2.5.6b)$$

where n_{ext} and n_{ord} are refractive indices in the parallel and perpendicular directions to the molecular axis. The film is assumed to be isotropic in x and y directions.

The k_{xmax} and k_{zmax} can be obtained from Korte model that takes into account the order parameters S and D that depend on the molecular orientation:

$$k_{x\max} = \frac{1}{3} k_{\max} \left[1 - S\left(1 - \frac{3}{2} \sin^2 \alpha \right) + \frac{1}{2} D \sin^2 \alpha \cos 2\beta \right] \quad (3.2.5.7a)$$

$$k_{x\max} = \frac{1}{3} k_{\max} + \left[1 + 2S\left(1 - \frac{1}{3} \sin^2 \alpha \right) - D \sin^2 \alpha \cos 2\beta \right] \quad (3.2.5.7b)$$

where k_{max} is the transition dipole strength, $S = \frac{1}{2}\left(2\cos^2 \tau - 1\right)$, $D = \frac{3}{2}\left(\sin^2 \tau \cos 2\psi\right)$ and ψ are the tilt and the twist angle of the molecule, α and β are the polar angles of the transitional dipole moment (figure 3.3.3.2).

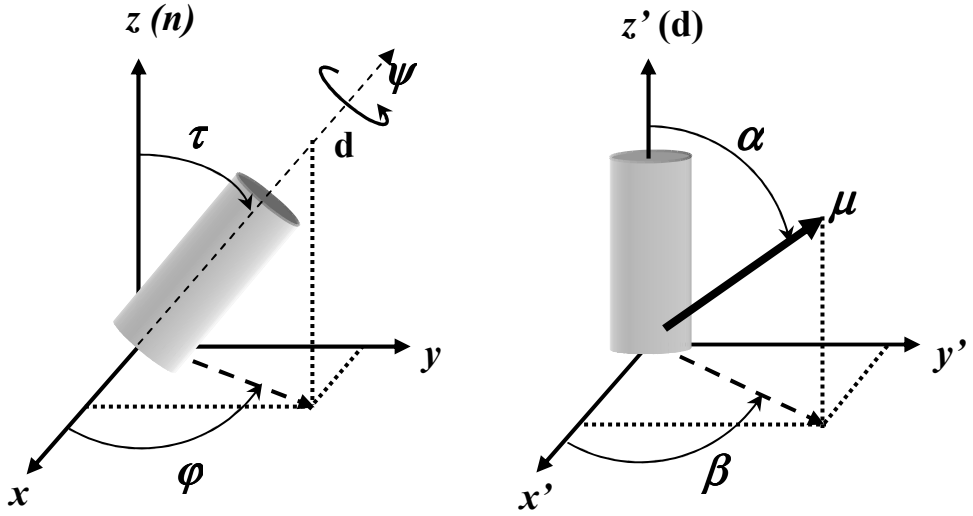

Figure 3.2.4. *The surface coordinate system (left) for the molecular director, d with its tilt angle, τ, twist angle, ψ and azimuth angle, φ; and the molecular coordinate system (right) for the transitional dipole moment μ with polar angles α and β*

The measured intensities at several incident angles are then compared with the simulated ones for various values of τ and k, to thereby obtain the value of tilt angle for particular transition moment.

4. Structure and ionic interactions of DPPG monolayers.

4.1 Introduction

Electrostatic interactions play an important role in the functioning of biological membranes. Membranes often bear a negative charge, manly due to the presence of acidic phospholipids as well as membrane proteins and gangliosides. It was shown that the phase behaviour and structure of acidic phospholipid membranes depends on the pH, the ionic strength and the nature of counterions: size, charge, hydrophobicity [64-66]. Phosphatidylglycerols (PGs) are components of many biological membranes, especially bacterial cell membranes; they are also one of the important components of pulmonary surfactants. The phase behaviour of these phospholipids was explored previously using bilayer systems, dispersions and Langmuir monolayers [65, 67-71]. However, there is still no clear picture of the dependence of the PGs ionisation state and structure on subphase composition. Different counterions have different influence. It was shown that addition of monovalent cations tends to expand PG membranes while addition of divalent cations condenses them.

Langmuir monolayers are convenient model systems to study the interaction between lipids and ions in the subphase since the air/liquid interface is planar, smooth and the lipid surface density is well controlled. Sacre and Tocanne [70] have used surface pressure/area isotherms of PG monolayers on various subphases to define the apparent pK_a of the PG head group. They found that the apparent pK_a values depend on the ionic strength and the size of alkali cations. Lakhar-Ghazal et al. [11] have studied the ionisation of PG monolayers by measuring the surface potential of monomolecular PG film as a function of the aqueous subphase pH and concentration of monovalent cations (Li^+, Na^+, Cs^+). It was demonstrated that the experimental data can be interpreted by means of Gouy-Chapman theory taking into account the specific cation adsorption. Their interpretation of the results is sometimes ambiguous, since the surface potential values are similar for all cations, although the binding constants derived from simulationsare completely different. In recent years Grigoriev et al. [72] have used Brewster angle microscopy to elucidate the DPPG dissociation constant. They assumed that the protonated DPPG forms solid like aggregates, while the dissociated part surrounds them. However, charged DPPG molecules can form a condensed phase as well. The major problem of these investigations is the fact that none of the methods used allows obtaining the ionisation degree directly. In the present work we are trying to solve this problem by techniques developed in the last decade for Langmuir monolayers:

Infrared Reflection Absorption Spectroscopy (IRRAS) and X-ray diffraction and scattering techniques, which provide straightforward information about structure and ionisation state of the DPPG monolayer. Gouy-Chapman theory is applied to evaluate the intrinsic pK_a of the DPPG monolayer.

4.2 Results

4.2.1 Surface pressure/area isotherms

Surface pressure/area isotherms of a DPPG monolayer on aqueous subphases with various pHs containing 0,01 M K^+ are presented in Figure 4.1. The shape of the isotherm depends strongly on the subphase pH. At pH 2, the DPPG monolayer is condensed at all surface pressures, the molecules occupy the smallest area at any surface pressure compared to the DPPG monolayer at higher pH. Increasing pH shifts the isotherm to a larger area/molecule and a plateau appears in the isotherm, which corresponds to the phase transition of a DPPG monolayer from the liquid expanded to a condensed phase. The transition pressure increases with increasing pH; at pH above 6 the transition pressure remains the same. A similar phenomenon was found previously by varying both pH and ion concentration [70, 72]. Obviously the ionization state of the phosphate group strongly influences structure and phase state of the DPPG monolayer, the larger charge densities (ionization state) at higher pH values lead to increasing repulsion between lipid molecules and thus to a more expanded structure. When full ionization is reached at pH 6 for 0.01 M salt the shape of the isotherm does not change with increasing pH.

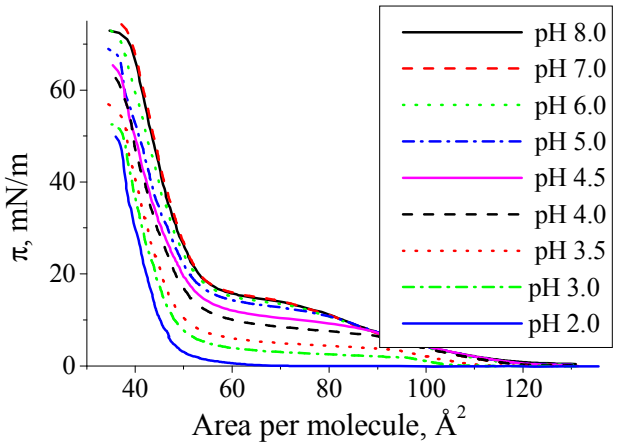

Figure 4.1. *Surface pressure/Area isotherms of DPPG monolayers at 23ºC on subphases with various pH values in the presence of 0.01 M K^+.*

To elucidate the influence of the counterion size on the DPPG monolayer phase behavior, the π/A isotherms were measured on subphases with different alkali cations: Li^+, Na^+, K^+, Cs^+. The effect of pH on the isotherm and area per DPPG molecule is similar for all these cations, however the transition pressure and shape of the isotherm slightly differ. This effect is small compared to the effect of the ion concentration or pH. Figure 4.2 represents the isotherms of DPPG monolayers on subphases with pH 9 (fully ionized DPPG monolayer) containing the same concentration of Li^+ and Cs^+. The phase transition of a DPPG monolayer on Li^+ appears at a little bit lower surface pressure, the molecules occupy a slightly smaller area (A) and the plateau is more horizontal. The shape of DPPG monolayer isotherms on subphases with Na^+ and K^+ resembles those on Li^+ and Cs^+ and the smooth change of the isotherm from Li^+ to Cs^+ in the order: π_{tr} and Area (Li^+) < π_{tr} and Area (Na^+) < π_{tr} and Area (K^+) < π_{tr} and Area (Cs^+) – is observed.

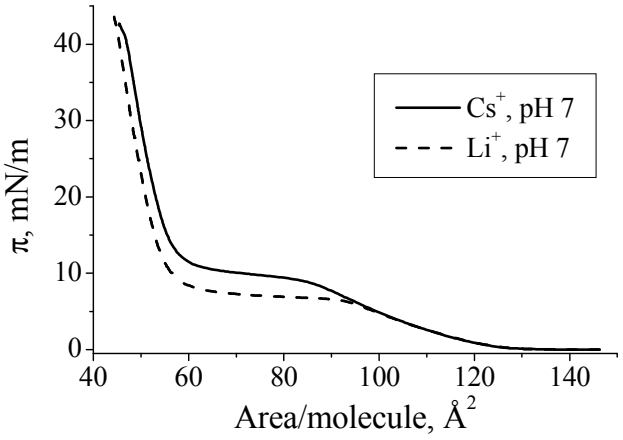

Figure 4.2. *Surface pressure/Area isotherms of fully ionised DPPG monolayer at 20ºC on subphases with pH 7 in the presence of 0.01 M cesium – left and 0.01 M lithium – right.*

In the study of phase transitions, the Clausius-Clapeyron equation is the most fundamental thermodynamical relationship (see theoretical part). In order to obtain the thermodynamical data compression isotherms of DPPG monolayer on subphases containing 0.01 M Li^+ and Cs^+ at pH of 7 were measured at different temperatures (Figure 4.3).

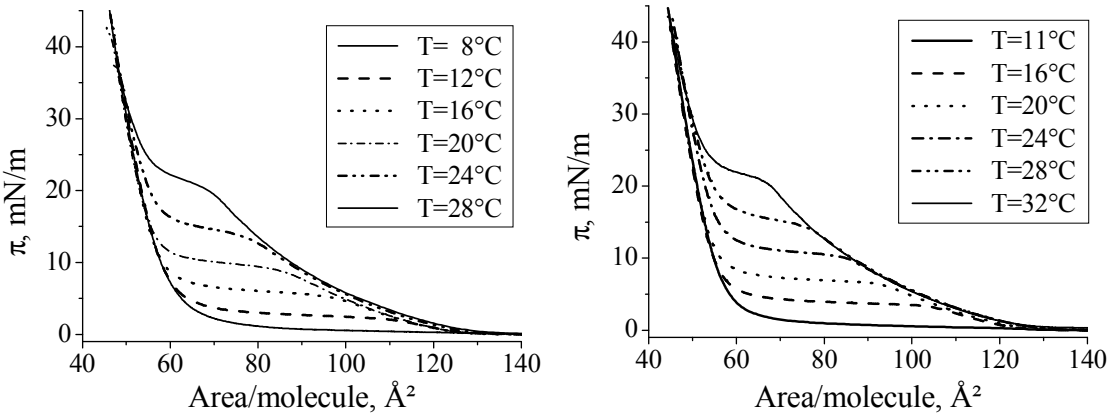

Figure 4.3. *Surface pressure/Area isotherms at various temperatures of fully ionised DPPG monolayer on subphases with pH 9 in the presence of 0.01 M cesium – left and 0.01 M lithium – right.*

Being treated with the procedure described in [73] and in the theoretical part of the present work, the data reveal that the characteristic temperatures (T_c and T_0) for DPPG monolayer on lithium and cesium differ from each other by approximately 3-4ºC and the transition enthalpy at the same temperature is larger in the case of lithium (Table 4.1).

Table 4.1.
The phase transition entropy and enthalpy and critical temperatures of fully ionised DPPG monolayer (pH 9) on 0.1 M lithium and cesium.

	Temperature, ºC	**ΔS, J/(mol·K)**	**ΔH, kJ/mol**	**T_0, ºC**	**T_c, ºC**
Li^+	16	-314.4	-90.9	13.9	37.1
	20	-270.0	-79.1		
	24	-196.1	-58.2		
	28	-140.2	-42.2		
	32	-75.2	-22.9		
Cs^+	12	-347.0	-98.9	11.0	32.8
	16	-278.8	-80.6		
	20	-199.3	-58.4		
	24	-141.7	-42.1		
	28	-85.4	-25.7		

4.2.2 X-ray Diffraction

The GIXD data provide information about packing of aliphatic chains in the condensed monolayers. Figure 4.4 represents contour plots of the corrected x-ray intensities versus the in-plane and out-of-plane scattering vector components Q_{xy} and Q_z, respectively, for DPPG

monolayers at 25 mN/m on subphases with pH 2 and pH 7 in the presence of cesium and lithium.

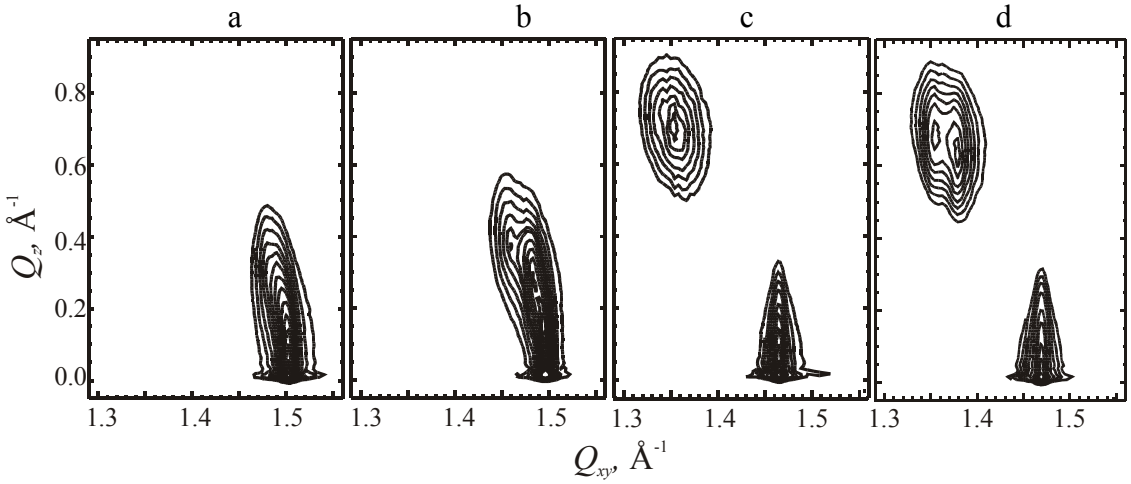

Figure 4.4. *Contour plots of the corrected X-ray intensities as a function of the in-plane component Q_{xy} and the out-of-plane component Q_z of the scattering vector of DPPG monolayer at 25 mN/m on various subphases: a – subphase with pH 2 adjusted with hydrochloric acid and without addition of other counterions, b – subphase with pH 2 adjusted with hydrochloric acid and with addition of 0.1 M CsCl, c – phosphate buffer with pH 7 and 0.1 M cesium as phosphate salt, EDTA salt and chloride, d – phosphate buffer with pH 7 and 0.1 M lithium as phosphate salt, EDTA salt and chloride.*

The data reveal a large difference in the structure of DPPG monolayers at low and at high pH. The DPPG aliphatic chains at pH 2 occupy a much smaller area and are less tilted than at pH 7 on both lithium and cesium. Apparently the DPPG monolayer is partly charged at pH 2, since its structure is affected by the presence of cesium. These data and, additionally, result obtained on pure water and on phosphate buffered saline (pH 7.4, 0.13 M Na^+, 0.008 M K^+) are presented in Tables A3.1 - 4 (see Appendix 3). The structure of the DPPG monolayer on subphase with pH 2 is similar to that on water. At low surface pressure, three diffraction peaks can be detected for DPPG on water as well as at low pH. Such a peak distribution indicates the existence of an oblique chain lattice with molecules tilted in an intermediate direction between nearest (NN) and next-nearest (NNN) neighbour direction. Increasing pressure leads to a shift to larger Q_{xy} and smaller Q_z values. This can be easily understood, because increasing lateral pressure decreases the tilt angle of the aliphatic chains. The phase transition to hexagonal packing of upright oriented molecules takes place between 35 mN/m and 40 mN/m for DPPG on water and between 30 and 35 mN/m on subphases with pH 2. On subphases with higher pH, the peak positions differ from those obtained on water and pH 2. The Bragg peaks positions are shifted to lower Q_{xy} and higher Q_z values indicating larger unit cell area and larger tilt angle of the aliphatic chains. For subphases with pH 7, the transition to hexagonal packing cannot be achieved even at

a very high surface pressure. At a surface pressure of 40 mN/m, the tilt angle amounts still to 26°. Obviously, increasing the ionization state of the DPPG head group at higher pH and salt concentration leads to increased repulsion between molecules and to the reorientation of the head groups. The mismatch between the head group size and the size of the two aliphatic chains results in the tilted structure observed at all pressures.

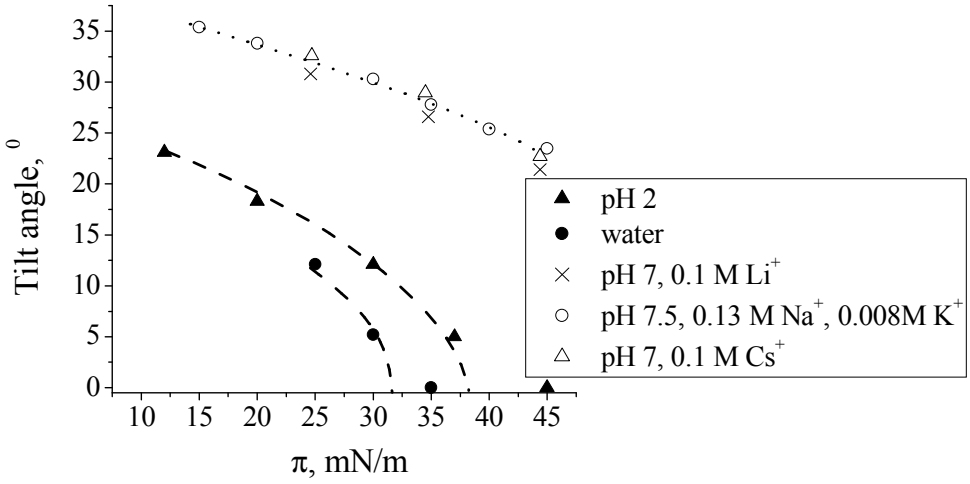

Figure 4.6. *Tilt angle as a function of surface pressure of DPPG monolayers on various subphases.*

Figure 4.6 illustrates the strong effect of pH and ionic strength (ionization state of DPPG) compared with the small effect of monovalent cation nature (specific binding) on the tilt angle of aliphatic chains at various surface pressures. It is clear that the effect of ionization is much larger than the effect of the cation size.

In order to demonstrate the condensation effect of divalent cations on DPPG, the GIXD measurements were performed on DPPG monolayers in the presence of Mg^{2+}, Ca^{2+}, Zn^{2+} and Cu^{2+} ions. The structure as well as the phase behaviour of DPPG in the presence of these cations differs significantly from its behaviour on monovalent cations at the same pH. The phase transition disappears (condensation effect) and the molecules are tighter packed (Tables A3.5-8 in the Appendix 3). The tilt angle as a function of the surface pressure for DPPG alkyl chains on subphases containing 0.005 M of Mg^{2+}, Ca^{2+}, Zn^{2+} and Cu^{2+} is shown in Figure 4.7.

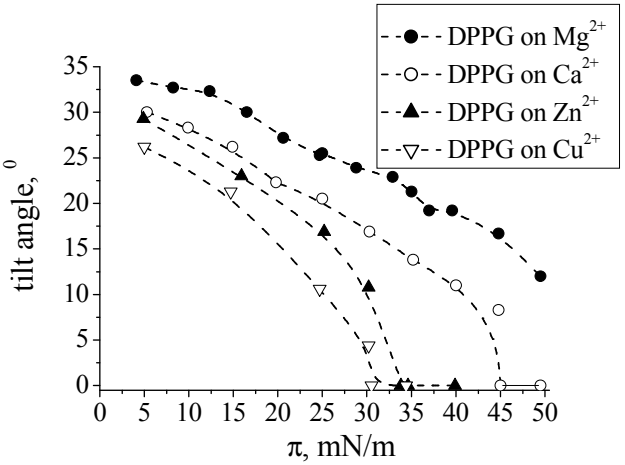

Figure 4.7. *Tilt angle as a function of surface pressure of DPPG monolayers on various subphases containing 0.005 M of divalent cations with neutral pH.*

The data clearly demonstrate that the structure of the DPPG monolayer is influenced by the divalent cation nature. The data reveal that in the presence of magnesium ions the DPPG molecules occupy a larger area in the monolayer than in the presence of other divalent ions. Obviously, the ion radius and hydration level play a certain role, magnesium is smaller than other cations but it is well hydrated and its hydration radius is bigger than that of calcium (Vormann and Guenter, 1993). Therefore it is not favourable for Mg^{2+} to penetrate deep into the head group region where it will partly loose the hydration water. Cupper and zinc probably bind not only electrostatically but they can form a complex. Therefore, the monolayer structure is completely different in the presence of these two cations.

4.2.3 X-ray Reflectivity

A series of X-ray reflectivity curves of the DPPG monolayer obtained on subphases containing Cs^{+} at different pH is shown in Figure 4.8 (left). Cesium was chosen due to its high electron density compared to water and lipid. To elucidate the electron density profiles, each curve was fitted with a box model by varying the roughness, thickness and electron density using the Paratt program.

Fitting of the experimental curves reveals a decrease of lipid chain thickness with increasing pH. This can be easily understood because the DPPG aliphatic chains tilt stronger at higher pH as demonstrated by GIXD and hence the monolayer thickness decreased. Integrating the electron density along z multiplied by the area/molecule obtained from the GIXD data gives the number of electrons as a function of distance for one molecule. The number of electrons can

be estimated from the chemical structure of the monolayer. However the water amount is unknown and does not allow precise determination of the ionisation degree.

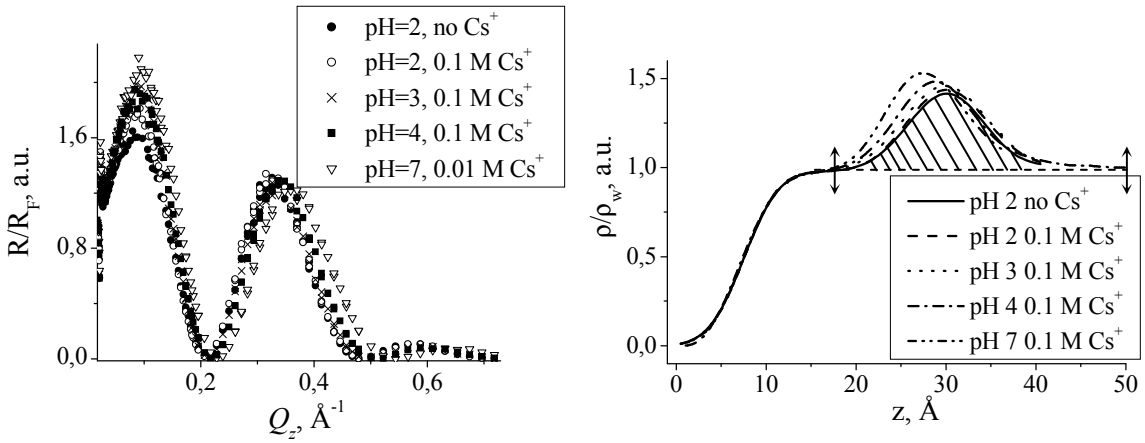

***Figure 4.8**. X-ray reflectivity divided by the Fresnel reflectivity (left) and the electron density profiles (right) of DPPG monolayer on various subphases.*

In order to estimate the ionisation degree, we have calculated the excess amount of electrons in the head group region, which arises from the high electron density of phosphate compared to water or glycerol and to the high electron density of cesium attracted to the negatively charged phosphate group of DPPG. The number of excess electrons – N_{ex} (compared to the number of electrons in a water layer of the same thickness) can be calculated by integrating the electron density profile (Figure 4.8, right) in the head group region multiplied by the area per molecule (A) obtained from GIXD.

$$N_{ex} = \left(\int_{15}^{\infty} \rho(z)dz - \int_{15}^{\infty} \rho_w(z)dz \right) \cdot A$$

In this case the contribution of the lipid remains the same for all pHs while the contribution of cesium varies. Table 4.2 shows that the excess number of electrons in the head group region increases with increasing pH due to a larger amount of counter ions near the phosphate at higher ionisation state. The data reveal 55 excess electrons in the head group of DPPG at pH 2 without Cs^+ and 91 excess electrons in the DPPG head group at pH 7 with Cs^+. The excess of electrons in the head group region at different pHs should be proportional to the charge of DPPG molecules. We assume that alpha (degree of ionisation) of DPPG at pH 7 is 1, then alpha at lower pHs (2,3,4) must be proportional to the difference between excess of electrons at current pH ($N_{ex}^{pH_i}$, i=2,3,4) and pH 2 ($N_{ex}^{pH_2*}$) without Cs^+ in the subphase divided by the difference between excess water at pH 7 ($N_{ex}^{pH_7}$) and pH 2:

$$\alpha = \frac{\left(N_{ex}^{pH_i} - N_{ex}^{pH_2^*}\right)}{\left(N_{ex}^{pH_7} - N_{ex}^{pH_2^*}\right)}.$$

Table 4.2.
Excess of electrons in the head group region over the water layer of the same thickness N_{ex} for DPPG monolayer at 25 mN/m on varios subphases.

pH	Concentration of Cs^+, M	N_{ex}
2	No Cs^+	55
2	0.1	65
3	0.1	74
4	0.1	84
7	0.01	91

The obtained titration curve is shown in Figure 4.9. The data reveal that the DPPG monolayer is partly charged even at pH 2 in the presence of 0.1 M CsCl that is in good agreement with the x-ray diffraction data. The experimental data were fitted according to the equation given in the theoretical part (2.1), which is deduced from the Gouy-Chapman theory and does not take into account the specific counterion adsorption. The best fit to the experimental data was achieved for $pK_a = 1$ (Figure 4.9).

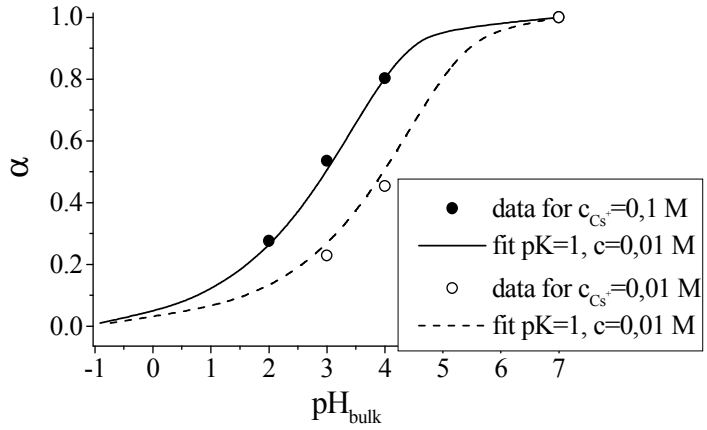

Figure 4.9. *The titration curve obtained from x-ray reflectivity measurements for DPPG monolayer on subphases containing 0.1 and 0.01 M cesium. The experimental data were fitted by the theoretical curves based on Gouy-Chapman theory.*

4.2.4 IRRAS

IRRA spectra in the region of phosphate stretching bands of DPPG monolayer on subphases at various pH and constant ionic strength are shown in Figure 4.10 (left). They should yield direct information on free and protonated head groups.

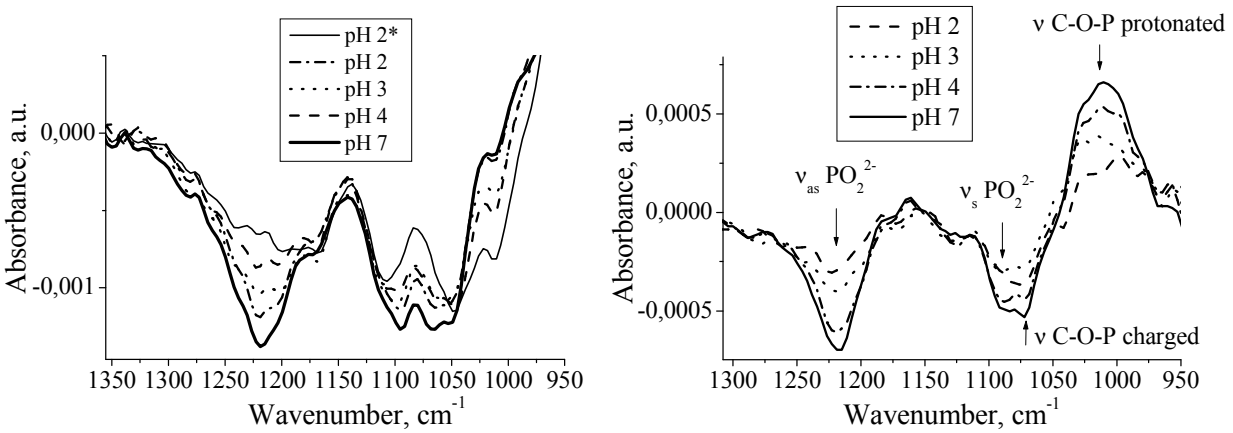

Figure 4.10. *Selected region of IRRA spectra of the DPPG monolayer at 25 mN/m on subphases containing 0.1 M lithium at various pHs and * on subphase with pH 2 and no lithium – left; the spectrum of DPPG monolayer at 25 mN/m on subphase with pH 2and without Li^+ is subtracted from the other spectra - right.*

It was found that position and intensity of these bands does not depend on the alkali counterion size (Figure 4.11). Beside the asymmetrical and symmetrical PO_2^- stretching modes at ~ 1217 cm^- and ~ 1090 cm^{-1}, respectively, there are many other vibrations in this region, namely: CO-O-C asymmetrical and symmetrical stretching modes at ~ 1170 cm^{-1} and at ~ 1070 cm^{-1} [37], C-O stretching of glycerol (CH_2-OH) in the region 1060-1025 cm^{-1}, C-O-P-O-C stretching mode at ~ 1060 cm^{-1} for charged phosphate and in the region 1040-1010 cm^{-1} for the protonated one, and additionally the P-O-(H) stretching mode in the same region [74]. The P=O stretching mode of the protonated phosphate is difficult to identify, however it has to appear in the region of 1139-1191 cm^{-1} and is reported to be broad and diffuse [75]. Therefore one can follow the change in the asymmetrical and symmetrical stretching vibrations qualitatively, but the direct quantitative determination of the ionisation state of the DPPG monolayer is impossible. To overcome these problems the spectrum of the DPPG monolayer at pH 2 without Li^+ can be subtracted from spectra at other pHs with Li^+. Since the intensity of the bands in this region does not strongly depend on the packing density, we assume that it depends only on the ionisation state of the DPPG monolayer. Figure 4.10 (right) represents the result of this treatment. The obtained negative bands can be explained by the increasing intensity of PO_2^- stretching (asymmetrical 1217 cm^{-1} and symmetrical 1080 cm^{-1}) and C-O-P-O-C stretching (1067 cm^{-1}) with increasing pH. Whereas positive bands are due to the disappearance of the P-O-(H) band and the shifting of C-O-P-O-C stretching mode from 1070-1060 cm^{-1} to 1040-1000 cm^{-1}.

It is interesting to note that the asymmetrical phosphate stretching mode appears at lower wavenumbers than for other phospholipids (PC, PS, PE). This can be explained by a better

hydration or by involving the phosphate group of DPPG into hydrogen bonding with the glycerol hydroxyl group of neighbouring molecules [71]. The last is more favourable since the shift of the phosphate asymmetrical stretching mode to lower wavenumbers was observed even for dry DPPG films [48].

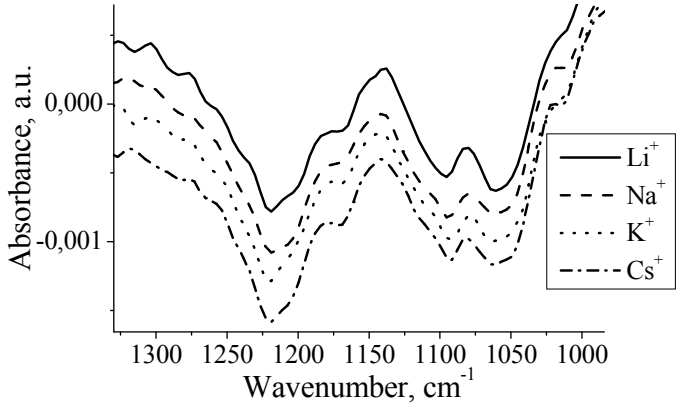

Figure 4.11. *Selected region of IRRA spectra of DPPG monolayers at 25 mN/m on subphases with pH 7 containing 0.1 M of various alkali cations. The spectra of DPPG monolayers on Li^+, Na^+, Cs^{2+} are shifted for clarity by 0.0005,0.0002 and – 0.0003 a.u., respectively.*

The asymmetrical stretching band was chosen to calculate the ionisation state of the DPPG monolayer. The intensity of this band can be directly transferred into the degree of ionisation – α. The only problem is that the ionisation degree of the monolayer at pH 2 is unknown and cannot be evaluated from IRRA spectra. To overcome this problem we use the degree of ionisation of DPPG at pH 2 obtained from x-ray reflectivity ($\alpha_{pH\,2}$ = 0.14). Then the intensity of the difference spectra at any pH ($A_{pH\,i}$- $A_{pH\,2}$) will be proportional to the difference between degree of dissociation at any pH and at pH 2 ($\alpha_{pH\,i}$ - $\alpha_{pH\,2}$). One obtains $\alpha_{pH\,i}$ if one assumes that $\alpha_{pH\,7}$ = 1:

$$\alpha_{pHi} = \frac{A_{pHi} - A_{pH2}}{A_{pH7} - A_{pH2}} \cdot 0.86 + 0.14$$

The obtained values of α for DPPG at various pH and different counterion content are shown in Figure 4.12. The obtained α is consistent with that obtained from x-ray reflectivity measurements and does not depend on the monovalent counterion size.

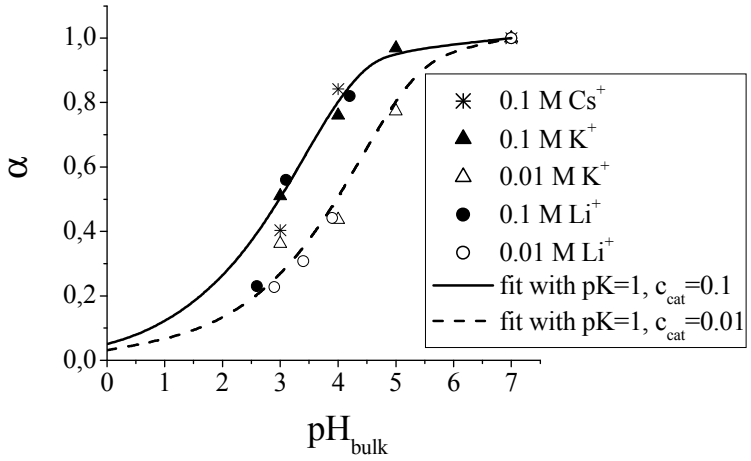

Figure 4.12. *Degree of dissociation a as a function of pH for DPPG monolayers at 25 mN/m obtained from IRRAS for various subphases.*

To prove the influence of the divalent cation nature on the DPPG phosphate group the IRRA spectra of DPPG monolayers in the presence of Mg^{2+}, Ca^{2+}, Zn^{2+} and Cu^{2+} were measured (Figure 4.13). The obtained spectra differ in the phosphate region. Obviously the influence of the ions nature is much more pronounced for divalent cations than for monovalent ones. The asymmetrical stretching mode of the DPPG monolayer on subphases containing magnesium appears at ~ 1223 cm^{-1}. However, in the presence of calcium, the band is more pronounced and sharp. In contrast, on zinc containing subphases, it occurs at ~ 1211 cm^{-1} and on cupper at 1203 cm^{-1}. The shift to higher frequencies in the case of Mg^{2+} and Ca^{2+} can be related to a dehydration of the DPPG head group, whereas the opposite shift in the presence of Cu^{2+} and Zn^{2+} indicates complex formation with the phosphate group of the DPPG monolayer [64].

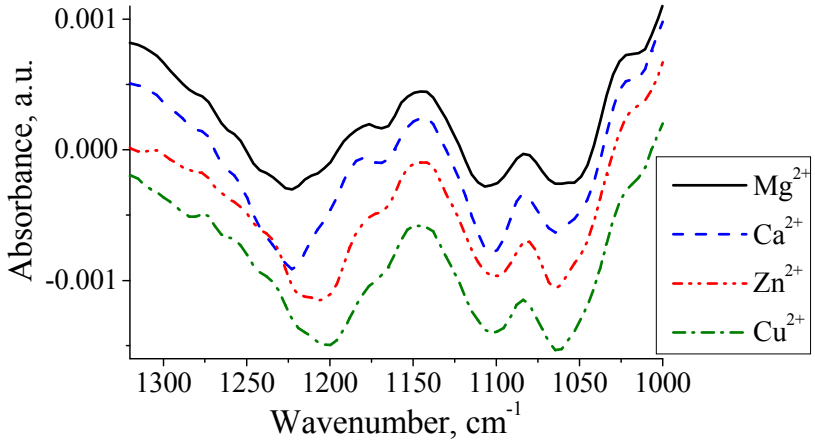

Figure 4.13. *IRRA spectra (selected region) of DPPG monolayers at 25 mN/m on subphases with pH 7 containing 0.1 M of various divalent cations. The spectra of DPPG monolayers on Mg^{2+}, Ca^{2+}, Cu^{2+} are shifted for clarity by 0.0006,0.0003 and – 0.0003 a.u. respectively.*

4.3 Discussions

DPPG has an ionizable head group and therefore its phase behavior depends on both pH and ionic strength of the subphase as shown by surface pressure/area isotherms. At high pH and at modest monovalent counterion concentration the DPPG monolayer is more ionized compared to pure water or subphases with low pH. The higher ionization of DPPG monolayer increases the repulsion between neighboring molecules, which leads to the formation of a more loosely packed layer. The increased distance between molecules in the monolayer decreases the inter-chain interactions and leads to a stabilization of the liquid-expanded phase. Besides, the counterions can penetrate into the head group region and increase the distance between the DPPG molecules as well. The penetration of counterions can explain the small difference in the phase behavior of DPPG observed on lithium and cesium. However, one has to distinguish between specific adsorption of counterions and formation of a diffuse double layer near the charged DPPG head groups. The monovalent cations, even when forming the diffuse double layer, can partially penetrate into the head group region. For example the length of the ionic atmosphere formed by 0.1 M monovalent cation near the highly charged surface is around 3 nm and is in the range of the head group size (~ 1nm).

The surface pressure/area isotherms alone do not allow obtaining degree of dissociation versus pH, since the ionisation state is not observed directly. The area occupied by a molecule can be an indication of the ionisation state but one cannot distinguish between the slightly charged monolayer and a completely protonated one. By applying the x-ray reflectivity technique we were able to estimate the ionization degree of the DPPG monolayer at various pH and monovalent salt concentrations. It was possible to obtain the ionization degree of a DPPG monolayer even at low pH. The experimental titration curves for 0.1 M and 0.01 M cesium are in good agreement with the theoretical curves using Gouy-Chapman theory. The obtained intrinsic pK_a ($pK_a = 1$) value is close to the one estimated previously ($pK_a = 1.2$ [70]) and is realistic. It is unlikely that cesium specifically adsorbs to the DPPG monolayer. At least the proton can successfully compete with cesium at low pH indicating that the binding constant of the DPPG monolayer with protons is larger than with cesium.

IRRAS supports the data obtained from X-ray reflectivity. Moreover, the ionization degree of a DPPG monolayer is found to be independent of the monovalent cation size. There is no complete proof that alkali cations do not form a Stern layer. However, the contribution of the latter has to be small since the difference between cesium and lithium is small. The alkali cations

do almost not specifically bind to the phosphate group of DPPG.

From the other hand it was shown that the structure and thermodynamics of the DPPG monolayer is slightly influenced by the cation nature. DPPG on lithium has the tendency to form a more ordered structure and on cesium a more disordered one. Cations forming the diffuse double layer perturb the water structure in the vicinity of the monolayer. However, this perturbation is small and does not change the hydration of the phosphate group. But it may slightly change the geometry of hydrogen bonds, which leads to a slight difference in the structure formed by DPPG on lithium and cesium. Additionally, being attracted to the charged monolayer, alkali cations undergo partial dehydration. It is well known that cesium is less hydrated than lithium. Therefore, penetration into the head group region is easier for cesium than for lithium. A slightly higher cesium concentration compared with lithium in the head group region of DPPG influences the interaction between neighboring DPPG molecules and the monolayer becomes more disordered. This is seen by a decrease of the characteristic temperatures (the liquid expanded phase appears at lower temperatures). Apparently, cesium is not able to neutralize the DPPG charge. Decreased repulsion due to neutralization would lead to a condensation of the monolayer as observed in the case of protons.

A different picture is observed in the presence of divalent cations. The structure of the DPPG monolayer is strongly affected by these cations. Mg^{2+} and Ca^{2+} ions binding to the DPPG monolayer lead to condensation and dehydration of DPPG molecules. Nevertheless Mg^{2+} is not able to penetrate so deep into the head group region and dehydrate the DPPG monolayer as Ca^{2+} does. It is better hydrated and forms, therefore, a more diffuse layer and hence the structure of the DPPG monolayer on Mg^{2+} also resembles that on alkali cation subphases. Cu^{2+} and Zn^{2+} are obviously involved in complex formation with phosphate (probably between neighbouring molecules) that leads to the formation of a compact lattice of the lipid aliphatic chains. The Gouy-Chapman approach in the case of divalent cations cannot satisfactorily describe such differences. The interactions between the lipid and such metal cations as Zn^{2+} and Cu^{2+} have probably more covalent character.

5. Interactions of lipid monolayers with fusogenic peptide B18

5.1 Introduction

B18 is a synthetic peptide consisting of 18 amino acids that reproduce the minimal membrane-binding motive of the acrosomal protein bindin [76]. This highly conserved part of the parent protein mediates the fertilization of the sea urchin. It is thought to play a key role for the adhesion and fusion between sperm and egg membranes. It was demonstrated that B18 resembles the fusogenic properties of the bindin protein [20, 21, 76]. To understand the mechanism of the peptide binding to the phospholipid membranes it is necessary to elucidate structural changes induced in both peptide and the lipid membrane upon binding. The previous researches were focused on the structure of B18 [20, 21, 77-79] under membrane binding conditions and the role of zinc and cupper ions as mediators for B18 membrane activity [19, 76, 80]. The methods used were electron microscopy [20], nuclear magnetic resonance [21, 77-79], CD spectroscopy [21, 76], mass spectrometry [80], x-ray diffraction techniques [20] and FTIR [19]. The NMR data allow determination of the peptide structure with local details. However, methods used previously suffer the information about the lipid structure. Langmuir monolayer techniques open new facilities in investigating both the B18 structure at the membrane surface and lipid structural changes induced by the binding with peptide.

B18 is unstructured in aqueous solutions below pH 7 [21, 76] and it can slowly precipitate into extended β-sheet oligomers or fibrils at higher pH [20]. The formation of a β-sheet structure is concentration dependent and is facilitated in the presence of cupper and probably lipid vesicles with zinc at high peptide to lipid ratios. The oligomerization of the peptide at pH above 7 probably occurs because three histidines became uncharged under these conditions that decreases repulsion between neighbouring molecules. The peptide adopts also the α-helical conformation in buffer at pH above 7 in the presence of zinc and in membrane mimicking conditions – in the presence of SDS-micelles and TFE. The secondary structure of B18 in membrane-mimicking conditions was

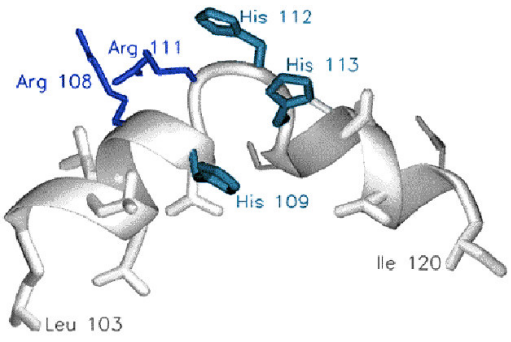

Figure 5.1 *Structure of the B18 in membrane mimicking conditions [21].*

elucidated by NMR technique [21]. The proposed structure is demonstrated in Figure 5.1. The structure formed is amphipathic. It consists of two short helixes with the kink between them. The hydrophobic residues are located in the helix ends, while the charged residues are located in the region of the kink. It is interesting to note that all three histidines are located in the kink and are available for the complexation with zinc that probably stabilizes this structure.

In the presence of phosphatidylcholine bilayers, B18 adopts the β-sheet conformation at high peptide to lipid ratio and the α-helical at low ratio that reminds the behaviour of amyloid peptide [19, 81, 82]. However, for B18 the β-sheet formation requires a much larger peptide to lipid ratio than for amyloid peptide. ATR-FTIR spectroscopy of mixed lipid/peptide films in the atmosphere with varied humidity revealed that B18 adopts α-helical conformation in the presence of POPC bilayers independent of the presence or absence of zinc at low peptide to lipid ratio and that the peptide forms a β-sheet structure at high ratios. The helix formed is assumed to have a 'boomerang' like alignment in the membrane [78]. The more recent observations confirm that the B18 structure depends on the peptide to lipid ratio, and a new model of B18 fusion activity was proposed. The peptide in the β-sheet conformation appears to be more membrane active than the α-helical one [77]. Interestingly B18 forms parallel β-sheets in contrast to amyloid peptide that is thought to form mostly antiparallel ones.

The data obtained are sometimes controversial and no clear picture about the lipid structure is introduced. The GIXD and IRRAS experiments applied to mixed lipid/peptide films at the air/water interface can help to understand the processes occurring in the membrane when B18 binds to it. Since the peptide is positively charged, negatively charged lipids can have a specific effect on the peptide structure. Additionally, B18 peptide resembles some properties of amyloid peptides and therefore it is interesting to compare the behavior of these two peptides at the air/water interface and adsorbed to lipid monolayers.

5.2 Results:

5.2.1 B18 structure in aqueous solutions

The CD spectra can provide information about content of different secondary structure motives in the overall structure of peptides and proteins [83]. There are many different approaches to calculate the structure from the CD spectra [23]. However, none of these methods can give the exact amount of certain secondary structure components, especially for short

peptides. Only two methods can satisfactorily fit the experimental data for B18: Continll and MLR. The last method gives probably more reasonable values since it does not require precise determination of the peptide concentration. This is especially important for B18 that can form aggregates with zinc and lipid vesicles. Both programs show the same tendencies, however the absolute numbers can be completely different. Table 1 represents results of the B18 secondary structure estimation under various conditions obtained with these methods. The specification of each method is described in the experimental part. The poor reproducibility of the secondary structure content calculated by different approaches can be related to the fact that B18 forms very short α-helices and that none of these methods takes into account the length of α-helix and β-sheets. The database used in all approaches is made mainly from the protein structural data measured by CD-spectroscopy and proved by x-ray crystallography. The kink in the B18 structure is not necessarily a β-turn used in most of the methods and can have a different influence on the CD signal.

Table 5.1

Secondary structure of B18 in different conditions calculated by two programs: Continll and MLR

Solution	**Method**	**Secondary structure motifs, %**			
		α-helix	**β-sheet**	**turn**	**random**
water	Continll	2.4	23.9	10.2	63.5
	MLR	13.1	-	13.1	73.8
buffer at pH 7.5, 100 mM NaCl	Continll	3.3	20.8	9.9	66.0
	MLR	7.3	15.0	10.6	67.1
directly dissolved in buffer at pH 7.5, 100 mM NaCl	Continll	6.9	27.1	24.0	41.0
	MLR	-	48.7	13.5	37.7
buffer at pH 7.5, 100 mM NaCl, 1 mM $ZnCl_2$	Continll	18.1	25.2	15.8	41.8
	MLR	85.7	-	-	14.3
HFIP	Continll	20.1	21.5	16.0	42.4
	MLR	47.0	-	12.9	40.1
buffer at pH 7.5, 100 mM NaCl, after HPIP pretreatment	Continll	3.2	30.4	13.4	53.1
	MLR	0.8	28.5	4.5	66.2
DMPC vesicles in buffer at pH 7.5, 100 mM NaCl	Continll	4.2	33.6	14.7	47.4
	MLR	29.3	-	7.6	63.1
DMPG vesicles in buffer at pH 7.5, 100 mM NaCl	Continll	17.6	29.1	17.7	35.6
	MLR	49.6	8.5	-	41.9
SDS below the CMC	Continll	24.0	26.0	11.9	38.2
	MLR	68.2	-	-	31.8

The CD measurements (Figure 5.2) have proved that B18 is unstructured in water but it folds into β-sheet in buffer at pH 7.4-7.5 (only if the peptide was directly dissolved in the buffer). On the other hand, when the peptide was first dissolved in water and then diluted by buffer it remained unstructured. However, in this case, the CD signal slightly decreases at 198 nm and

increases at 217 nm, that indicates formation of β-sheet structure. It is possible that the concentration we used was too low compared with [20] and therefore the peptide needs more time for complete transformation to β-sheets and aggregation. The pre-treatment with HFIP (hexafluoroisopropanol) also reduces formation of β-sheets, although the peptide partly remains on the walls of vessel used for peptide preparation and the signal is decreased compared to water and still some β-sheets are formed. In HFIP B18 adopts α-helical conformation as well as many other peptides. No effect of Zn^{2+} in $ZnCl_2$ solutions at pH below 7 was found, although in buffer at pH 7.4 addition of zinc leads to the conformational change of the peptide structure from random coil to α-helix. A remarkable change in the structure was obtained only if the peptide concentration was above 100 μM. This is consistent with [21]. Obviously the peptide forms a complex through histidines with zinc ions or zinc hydroxide that is formed at neutral pH due to hydrolysis of zinc salts. Another requirement for complex formation can be the deprotonation of histidines at pH above 7 (pKa = 6.5) The CD signal is also significantly reduced which indicates aggregation of the peptide/zinc complex.

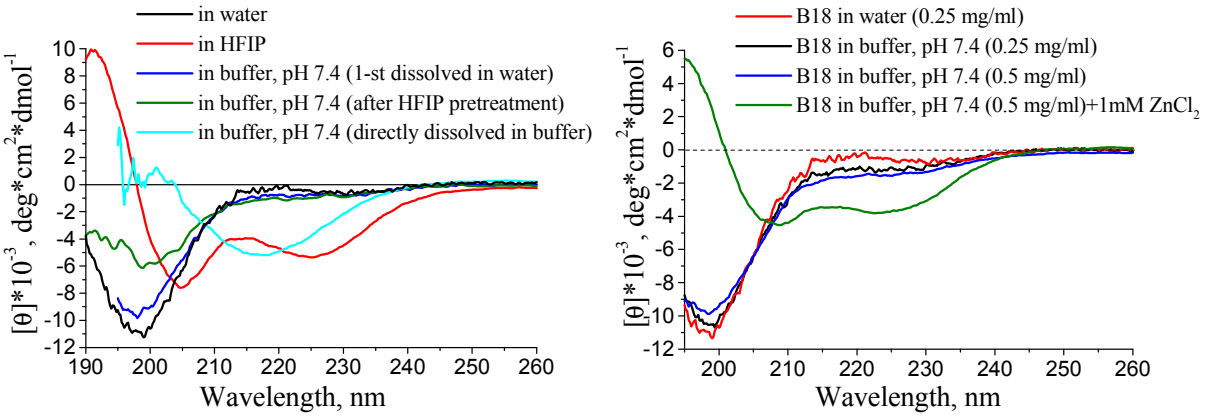

Figure 5.2. *CD-spectra of B18 left - in water, HFIP and directly dissolved in buffer with, pH 7.5 and in the same buffer with HFIP pre-treatment with; right – in water, first dissolved in water and when diluted with buffer with pH 7.5 in the absence and presence of* Zn^{2+}.

Figure 5.3 represents the CD spectra of B18 in buffer at pH 7.5 in the presence and absence of lipid vesicles. The negatively charged vesicles (DMPG) drastically change the spectrum shape, providing partly the α-helical partly the β-sheet structure in B18. In contrast presence of zwitterionic vesicles (DMPC) does almost not change the spectra shape, revealing only small influence of vesicles on the peptide structure. The effect was stronger in buffer with pH 7.5, than in water. The peptide to lipid ratio was 1 peptide to 30 lipid molecules.

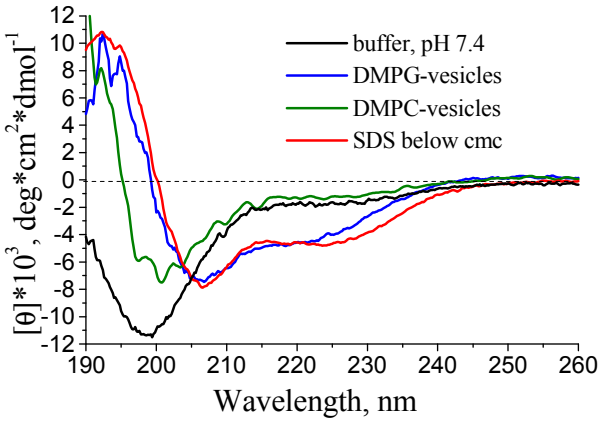

Figure 5.3. *CD-spectra of B18 in buffer at pH 7.5 and in the presence of lipid vesicles.*

5.2.2 Adsorption of B18 at the air/water interface and to the lipid monolayers

B18 is an amphipathic peptide therefore it has a pronounced surface activity (Figure 5.4 left). The kinetics of peptide adsorption is concentration dependent. The equilibrium surface pressure is around 20 mN/m for high peptide concentration and is smaller for lower peptide concentration. The hydrophobicity of B18 is increased at pH above 7, since the histidines become uncharged at this pH. Therefore the surface activity is enhanced in buffer with pH 7.5 compared to water (Figure 5.4 right).

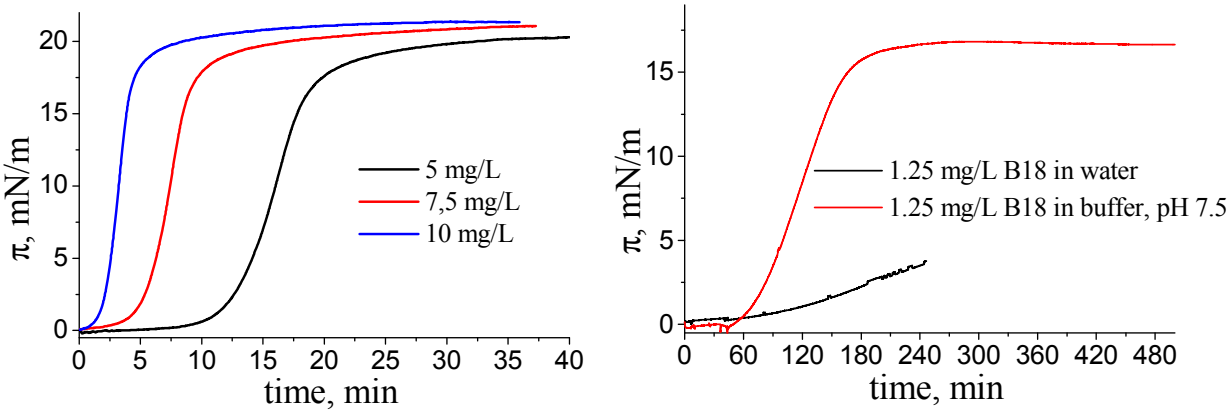

Figure 5.4. *Kinetics of B18 adsorption left - at the air/buffer interface for various peptide concentration in bulk; and right – at the air/water and air buffer interface for the bulk peptide concentration of 1.25 mg/L.*

The sigmoidal shapes in Figure 5.4 can be understood as follows. The initial adsorption at low densities hardly increases surface pressure. Shortly but below saturation, the adsorbed peptide film becomes less compressible causing the step slope in the surface pressure / time curve. At longer time the surface is saturated and equilibrium surface pressure is reached. Unfortunately it was not possible to measure adsorption isotherms more systematically because

of the limited amount and cost of the material.

Adsorption of B18 on a DPPC monolayer was performed at initial zero pressure of the monolayer and area of ~ 98 Å^2/molecule. The DPPC monolayer was transferred onto the 1.5 mg/L B18 solution in buffer at pH 7.5. The adsorption kinetics of B18 to the DPPC monolayer is shown in Figure 5.6 and it resembles features of the Aβ adsorption isotherm to the same lipid: a plateau appeared at a surface pressure of 4-5 mN/m and the equilibrium pressure is similar to that of the peptide adsorption to the pure air/buffer interface. The equilibrium surface pressure induced by B18 insertion is ~ 20 mN/m that is also similar to Aβ (see Chapter 6). In the presence of zinc the adsorption isotherm of B18 to DPPC monolayer is similar to one obtained on pure buffer, although the equilibrium pressure is slightly above 20 mN/m.

Adsorption of B18 was followed by fluorescence microscopy. To visualize the condensed phase domain formation, the lipid was doped with 1% of fluorescence-labeled lipid (NBD-PC). The labeled lipid has high solubility in the liquid phase and low solubility in the condensed phase, therefore the condensed domains formed in the phase transition region are dark spots in the bright liquid phase. Figure 5.5 shows the compression isotherm of a pure DPPC monolayer and corresponding FM images. In the plateau region the condensed phase domains (black spots) appear, grow and increase in number during compression.

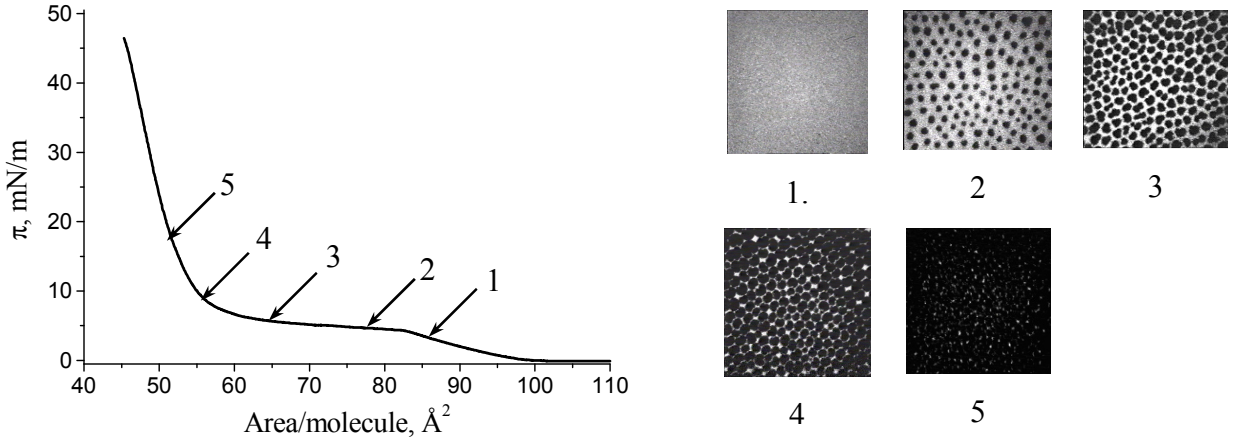

Figure 5.5. *Compression isotherm of a DPPC monolayer with 1% fluorescence-labelled lipid on buffer and corresponding fluorescence microscopy images. The images size is 280x300 μm^2.*

Very similar images were obtained during adsorption of B18 to the DPPC monolayer at initially zero surface pressure. The adsorption kinetics and corresponding FM images are shown in Figure 5.6. It is interesting to note that the domains are formed at the same transition pressure as for pure DPPC, but they do not grow with increasing surface pressure. Probably in the

beginning of the phase transition the formation of the DPPC domains is not influenced by the inserted peptide indicating that there are no interactions between the lipid and the peptide. The peptide, apparently, is excluded from the condensed phase of lipids. Therefore the brighter areas at high pressure represent parts of a monolayer occupied by the peptide and labeled lipid which are well mixed.

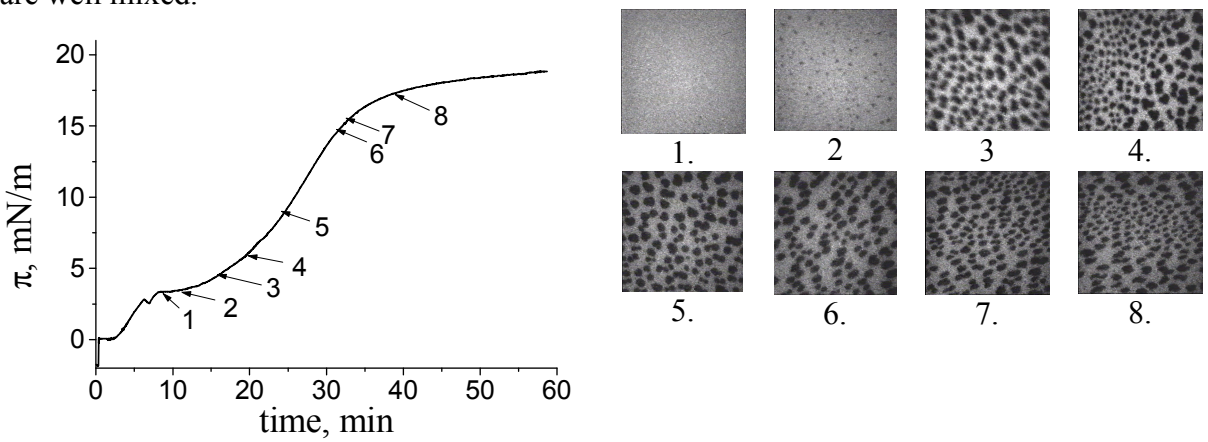

Figure 5.6. *Kinetics of B18 adsorption to the 1% fluorescence labeled DPPC monolayer and corresponding fluorescence microscopy images. The bulk peptide concentration in buffer at pH 7.4 was 1.5 mg/L. The images size is 280x300 μm^2.*

In the next step, the DPPC monolayer with adsorbed B18 was compressed to 50 mN/m. The peptide is squeezed-out from a lipid monolayer when the surface pressure increases. The shape of domains however remains unchanged, only slight deformation and increasing number of them is observed (Figure 5.7).

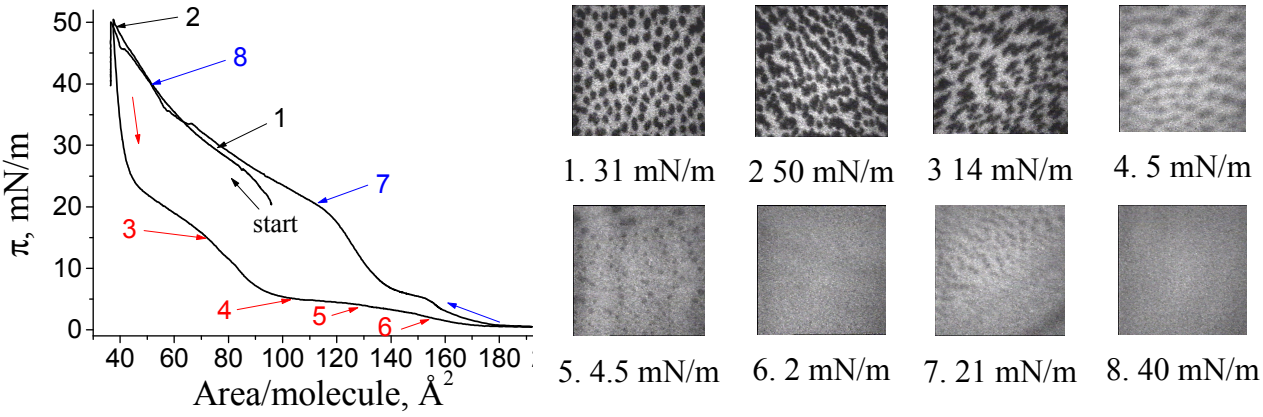

Figure 5.7. *Compression and expansion isotherm of a DPPC monolayer containing 1% fluorescence-labeled lipid on buffer and corresponding fluorescence microscopy images. 1-st compression is shown by black arrows, expansion by red arrows and 2-nd compression by blue The bulk peptide concentration in buffer at pH 7.4 was 1.5 mg/L. The images size is 280x300 μm^2.*

Expansion of the monolayer leads to a reinsertion of the peptide into the monolayer below 20 mN/m. The domains disappear at the transition pressure. During the second compression

domains are hardly formed, despite appearance of obvious phase transition in the surface pressure/area isotherm. It is possible that the domain size is too small to be observed with the present resolution (~ 2μm).

Adsorption of B18 to the negatively charged DPPG monolayer leads to a larger surface pressure increase, compared with DPPC (instead of 20 mN/m the final pressure is above 25 mN/m). The domains formed by DPPG at the phase transition are small even for a pure monolayer, therefore it is hard to see any domain formation during peptide insertion into the DPPG monolayer (Figure 5.8). The phase transition is also hardly seen in the adsorption isotherm. The transition pressure is decreased in the presence of zinc compared to the buffer at pH 7.5 and 100 mM NaCl. Obviously divalent zinc specifically adsorbs to the DPPG monolayer and condenses it. Compression to higher surface pressure leads to the peptide squeeze-out that is again similar to the behaviour of Aβ.

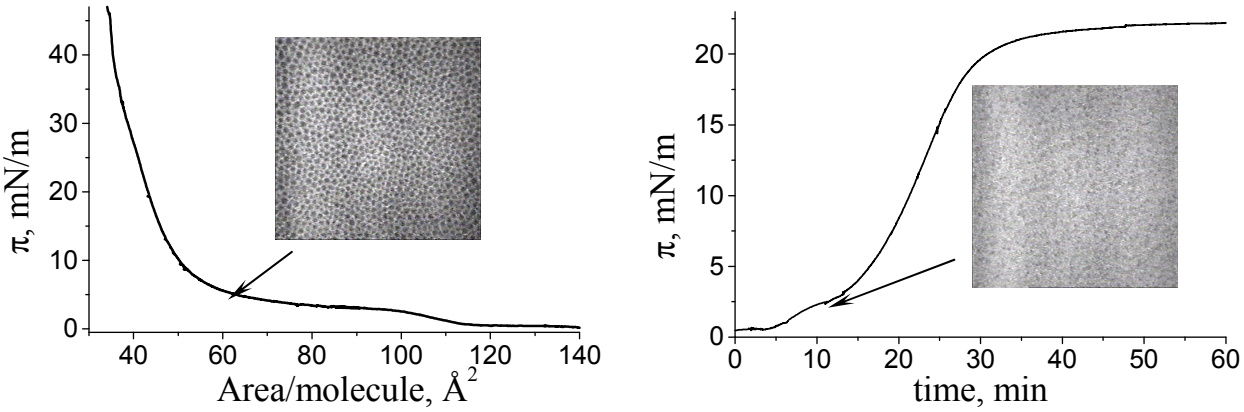

Figure 5.8. *Surface pressure/are isotherm of a DPPG monolayer on buffer: 10mM Hepes, 100mM NaCl, 0,3mM $ZnCl_2$, pH 7,5 – left. Right - kinetics of B18 adsorption to the 1% fluorescence labelled DPPG monolayer on the same buffer and corresponding fluorescence microscopy images in the phase transition region. The bulk peptide concentration in buffer at pH 7.4 was 1.5 mg/L. The images size is 280x300 μm^2.*

5.2.3 Structure of lipid monolayers with adsorbed B18 (GIXD).

In the GIXD experiments B18 was injected into buffer at pH 7.5 in the presence and absence of zinc underneath the DPPC monolayer compressed to 30 mN/m. During at least 1 hour, no insertion of the peptide was observed. The lipid structure is the same in both cases: in the presence and absence of zinc. Expansion of these monolayers to pressures below 20 mN/m was almost impossible (due to limited trough size) and the intensity of Bragg peaks from condensed lipid layer drastically decreased. The peak at zero Q_z can be still observed at the same position where it appears in the pure DPPC monolayer. Either the peptide insertion leads to melting of lipid molecules or, being inserted into a monolayer, peptide dilutes lipid crystallites and therefore

the intensity is decreased. The peptide insertion into the monolayer occurs at 25 mN/m in the presence of zinc and at 20 mN/m in its absence. The recompression to 30 mN/m led to "condensation" of lipid (peaks appear again). The structure of DPPC on the peptide solution is similar to DPPC on buffer (Tables A3.9-12 in Appendix 3 and Figure 5.9.)

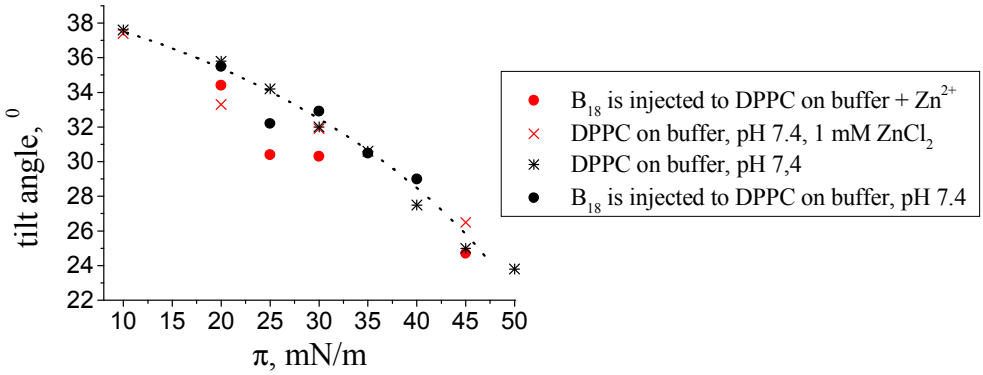

Figure 5.9. *Tilt angle of DPPC chains as a function of surface pressure.*

In the case of DPPG monolayer on buffer at pH 7.4 no change in the lipid structure was observed as well (Tables A3.4 and A3.13 in Appendix 3 and Figure 5.10). Intensity of the peaks at 20 mN/m is so low that the structural calculations are impossible.

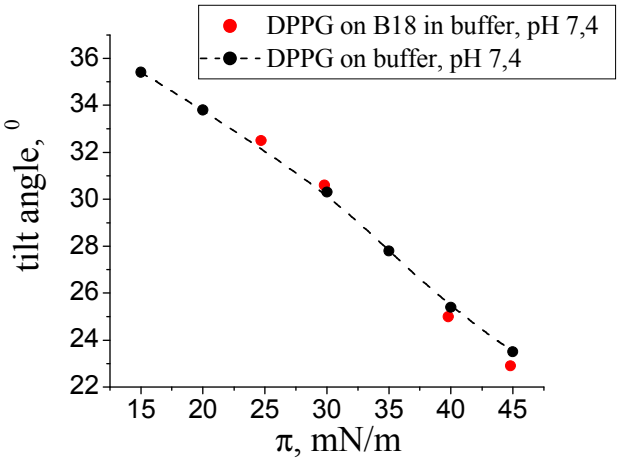

Figure 5.10. *Tilt angle of DPPG chains as a function of surface pressure.*

In the absence of salt in pure water the peptide adsorption leads to a complete disappearance of the diffraction pattern at 20-25 mN/m. Upon compression of the monolayer to the higher surface pressure, the lipid forms a crystalline structure (Figure 5.11 B,C). The diffraction peak is broad and slightly asymmetric. Certainly electrostatic interaction of B18 with negatively charged DPPG in the absence of salt and neutral pH is enhanced and this drastically changes the lipid structure. Moreover, for B18 adsorbed to the DPPG monolayer at high surface

pressure (above 30 mN/m) on pure water, an additional reflection at low Q_{xy} values (below 0.12 $Å^{-1}$) was observed (Figure 5.11 A)

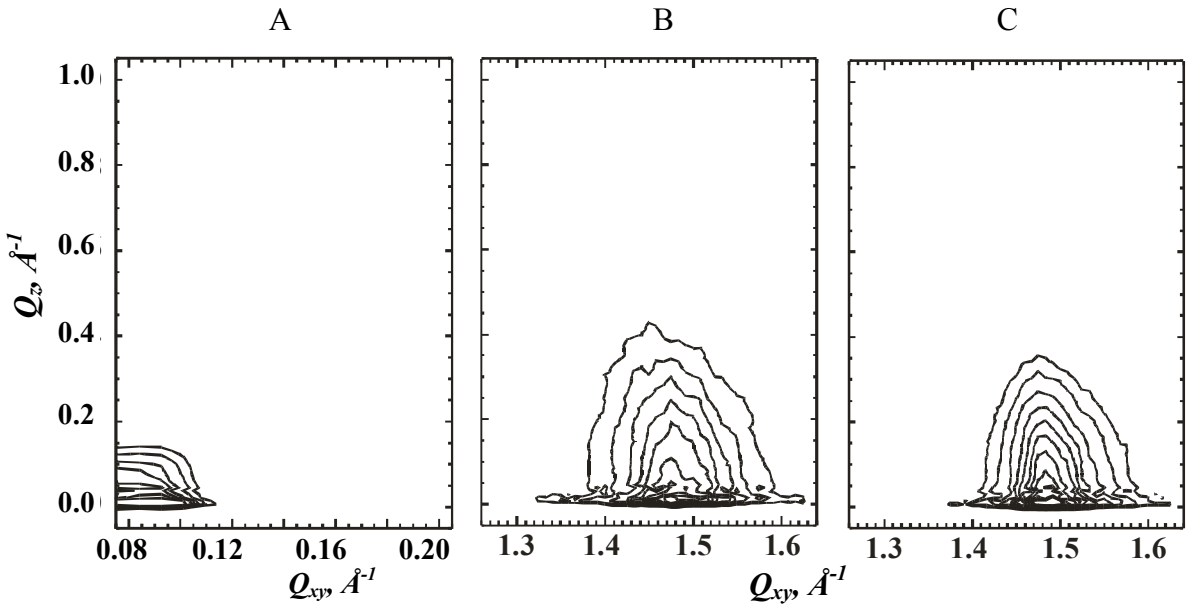

Figure 5.11. *Contour plots of the corrected X-ray intensities as a function of the in-plane component Q_{xy} and the out-of-plane component Q_z of the scattering vector of DPPG monolayer with adsorbed B18 on water in the small-angle region (A) at 40 mN/m and wide-angle region at 35 mN/m (B) and 40 mN/m (C).*

5.2.4 IRRAS of B18 adsorbed at the air/water interface and on lipid monolayers.

Adsorption of B18 to the air/water or air/buffer interface was followed by IRRAS. During adsorption, amide bands and water bands appear and grow (Figure 5.12) indicating increasing peptide concentration or density at the interface. The largest growth was observed when tat zero surface pressure. When the peptide layer is complete, the surface pressure increases and the intensity of all bands (especially amide bands) becomes constant. Probably the peptide reorients at the surface during adsorption in such a way that amide bands intensity does not change so much, but the water bands still grow because of increasing adsorption layer thickness. It is also shown that amide bands positions do not change during the adsorption process and they are similar for the peptide in water, buffer and buffer with zinc. The last indicates that no change in the peptide secondary structure occurs during adsorption and the bulk conditions (pH, salt, presence of zinc) do not influence it as well. The largest contribution in the amide I band region is observed at ~ 1658 cm^{-1} and in the amide II region at ~ 1542 cm^{-1}. Positions of Amide bands reveal that the peptide at the interface adopts either α-helical or random coil conformation [84].

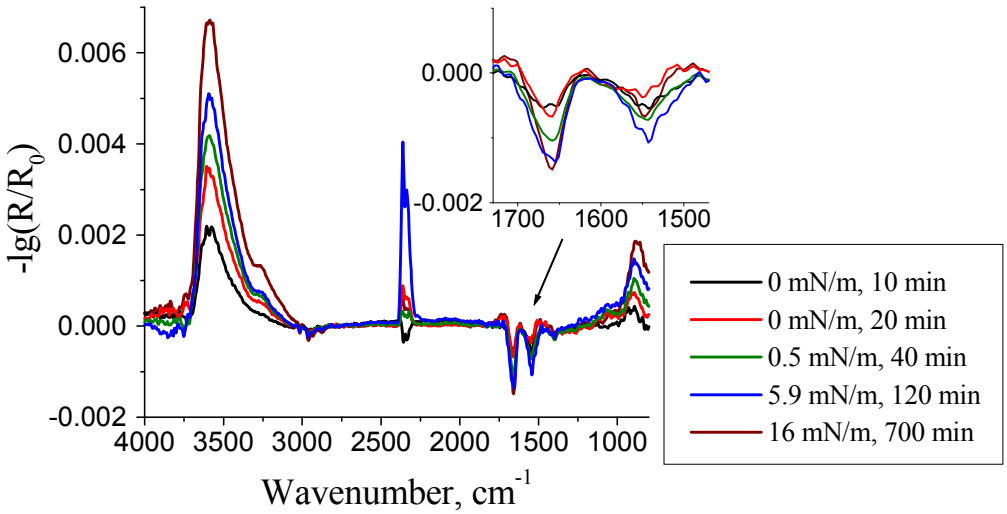

Figure 5.12. *IRRA spectra of B18 adsorbing to the air/buffer interface (c = 1.25 mg/L) acquired with s-polarized light at an incidence angle of 40º. The insert shows an extended view of the spectral rang between 1500 and 1700 cm^{-1}.*

Measurements were also acquired with p-polarized light at various angles of incidence (Figure 5.13). The amide I band remains negative at an angle of incidence above the Brewster angle, as obtained with s-polarized light, and it becomes positive at angles below the Brewster angle. At the same time the amide II band is negative at angles above the Brewster angle and it shifts to larger wavenumbers and remains negative at angles below the Brewster angle. This behavior can be explained by preferential orientation of the amide bonds of the peptide at the interface.

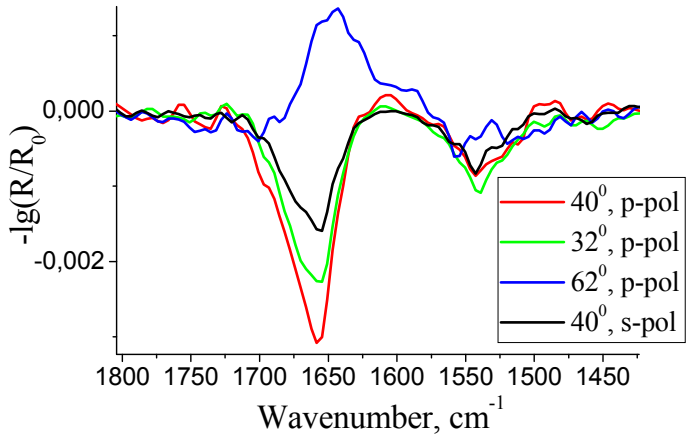

Figure 5.13. *IRRA spectra of B18 adsorbed at the air/water interface, obtained with s- and p-polarized light at various angles of incidence.*

To elucidate the B18 conformation at the interface the IRRA spectra can be simulated using a computing program, kindly provided by Dr. A. Kerth, and compared with experimental

ones. The program is based on the approach developed by Mendelsohn et al (Experimental part). The theoretical simulations of Amide bands for spectra obtained with p-polarized light at different incidence angles, considering an α-helix lying horizontally at the interface (tilt = 90º), slightly tilted from horizontal orientation (tilt = 70º), standing vertical and without preferential orientation, are shown in Figure 5.14.

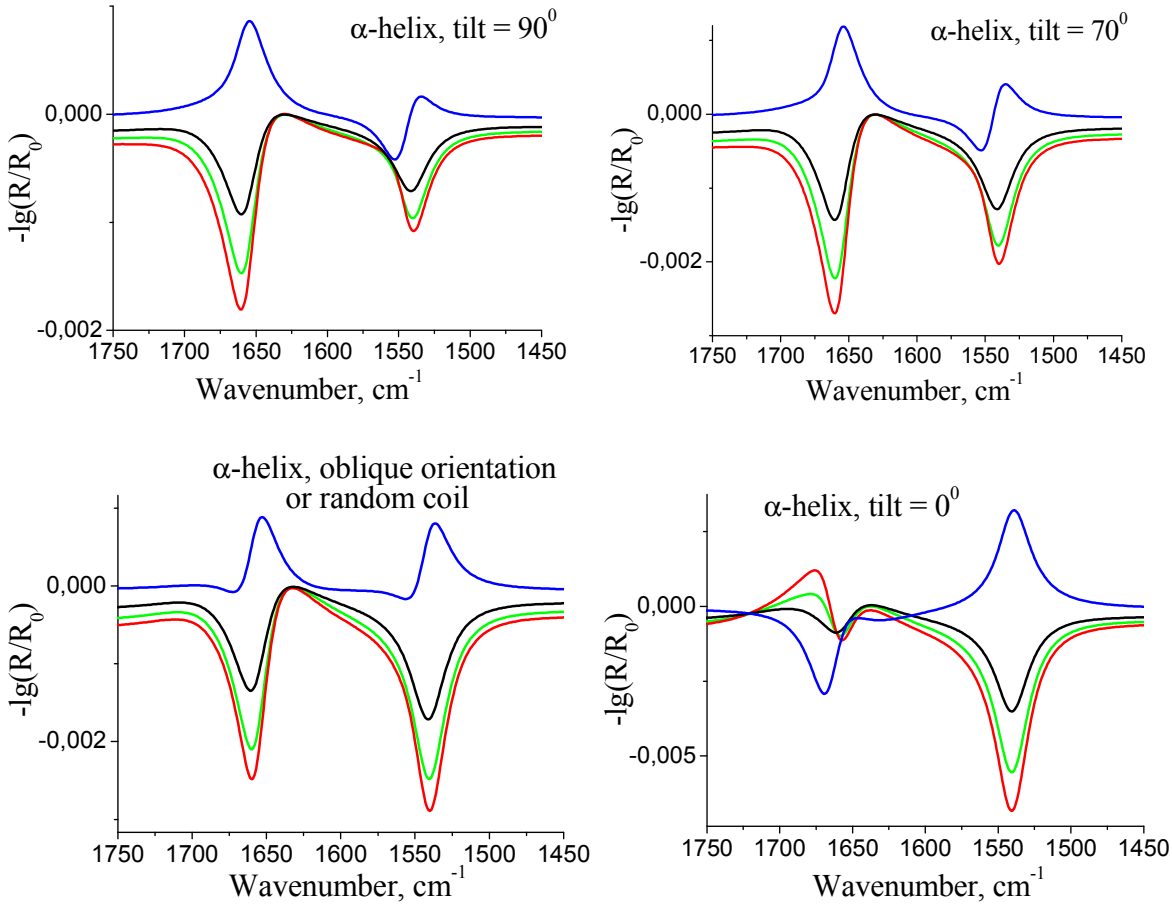

Figure 5.14. *Simulations of IRRA spectra. The spectra were calculated for an α-helix with length of 1.5 nm (approximately ten amino acid residues) and breadth of 0.5 nm. The reflectivity of the s- (black lines) and p-polarized light (coloured lines) was simulated. The spectra for the p-polarized light were calculated assuming an angle of incident light to the surface normal of 62° (blue line), 32° (green line) and 40°(red line). The polar angle α for Amide I was taken as 36° and for Amide II as 74°.*

The spectrum obtained for α-helix with oblique orientation (tilt = 54.7º) is identical to the spectrum obtained for random coil conformation (polar angles α of amide I and amide II bands are 45º). Obviously, neither spectra with vertical nor spectra with oblique orientation of the α-helix resemble the experimental spectra of B18. Therefore one can conclude that B18 forms an α-helix at the air/water or buffer interface that is lying almost horizontally at the interface. The

random coil conformation does not allow preferential orientation. Therefore the peptide apparently forms an α-helix at the interface. The low intensity, slightly higher wavenumbers and broadening in the region of 1674 cm^{-1} indicate the small size of the helix and probably the appearance of a kink [53]. Such a small broken helix is consistent with the previously proposed structure of B18 [21].

The angle between the transitional dipole moment of the Amide I band (ν C=O) and the long axis of α-helix should be 34-38º as determined experimentally by several groups [42]. Likewise, the angle between the Amide II (δ N-H) transition dipole moment and the long axis of α-helix can be estimated to be 73-79º. Hence, for theoretical simulation of IRRA spectra the polar angle α in the case of the α-helix was chosen to be 36º for the amide I band and 74º for the amide II band. The α-helix length was assumed to be 1.5 nm (approximately 10 amino acid residues) and the thickness to be 0.5 nm (one helix). The reduced amount of residues was taken because the helix formed by B18 is not a perfect helix and it probably has a kink in the middle. The twist angle was chosen to be 45º, because for a uniaxial molecule as helix the twist angle is not defined.

When the peptide is adsorbed to the DPPC monolayer at an initially low surface pressure it adopts a conformation similar to that at the pure air/water (buffer) interface. If one considers that the surface pressure increases due to compression of lipids by inserting peptide, then the area occupied by lipids should be ~ 50 $Å^2$ for 20 mN/m. In the case of the DPPC monolayer the initial area per lipid molecule was ~ 100 $Å^2$, therefore the inserted peptide should occupy half of the monolayer area. To prove this the pure lipid spectrum at 20 mN/m was divided by two, since according to Beer's law the band intensities are directly proportional to the concentration. For two-dimensional films the area/molecule can be used instead of the concentration. This spectrum is subtracted from the mixed lipid/peptide spectrum producing a spectrum of pure peptide. The last is compared with the peptide spectra obtained at equilibrium after adsorption to the pure air/water (buffer) interface also divided by two. The spectra are almost identical (Figure 5.15). This demonstrates that the peptide occupies approximately 50% of the surface and adopts similar conformation.

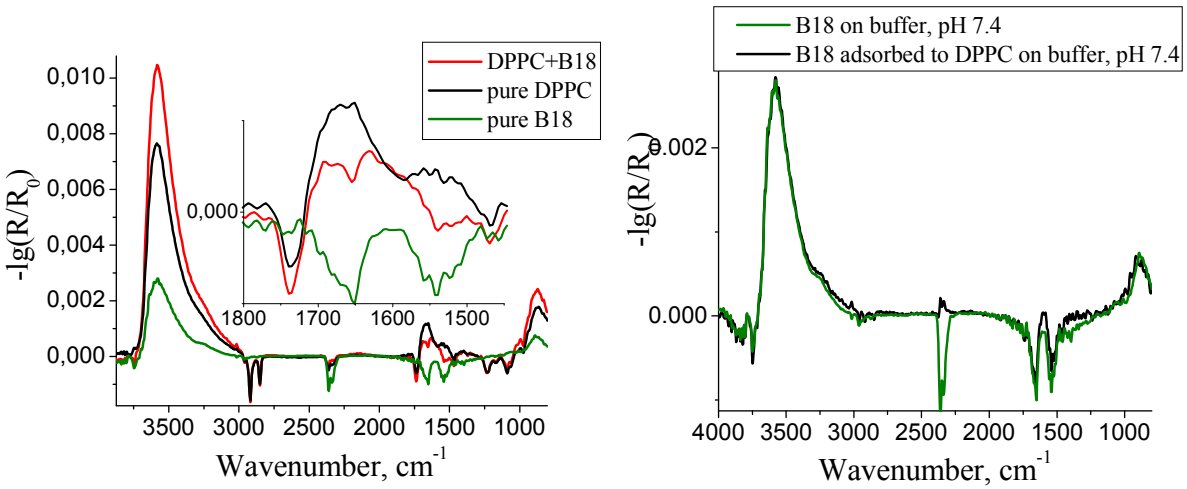

Figure 5.15. *IRRA spectra of the pure DPPC monolayer on buffer at 0 mN/m (black line), B18 adsorbed at the air/buffer interface (green line) and B18 adsorbed to the DPPC monolayer at initially 0 mN/m and final 20 mN/m (red line) in the left side. The B18 spectrum at the pure air/water interface divided by two (green line) and the spectrum of B18 adsorbed to the DPPC monolayer after subtraction of the lipid spectra (black) are represented in the right side. Spectra were acquired with the s-polarized light at the incidence angle of 40º.*

B18 adsorption to the DPPG monolayer on buffer results in a similar structure as in the case of a DPPC monolayer and of the pure air/water (buffer) interface (Figure 5.16). However the simple subtraction of lipid spectra is not possible, probably because the peptide adsorption changes the lipid structure. Additionally B18 may also adsorb to the headgroup region of the DPPG monolayer beside the intercalation. The structure of B18 adsorbed to the DPPG monolayer on water is even more different. The amide I band has two peaks at approximately 1660 and 1675 cm^{-1} and amide II becomes more pronounced and obviously changes the sign for p-polarized light above and below the Brewster angle. Probably the peptide does not form the helix structure or the helix orientation in this case is totally different. It is also possible that the part of peptide that intercalates into the hydrophobic region of the DPPG monolayer has still the helix conformation, but the other part that is located in the headgroup region of the DPPG monolayer does not form a helix but remains unstructured or even forms short β-sheets with many loops (small signal at 1630 and strong signal at 1675 cm^{-1}).

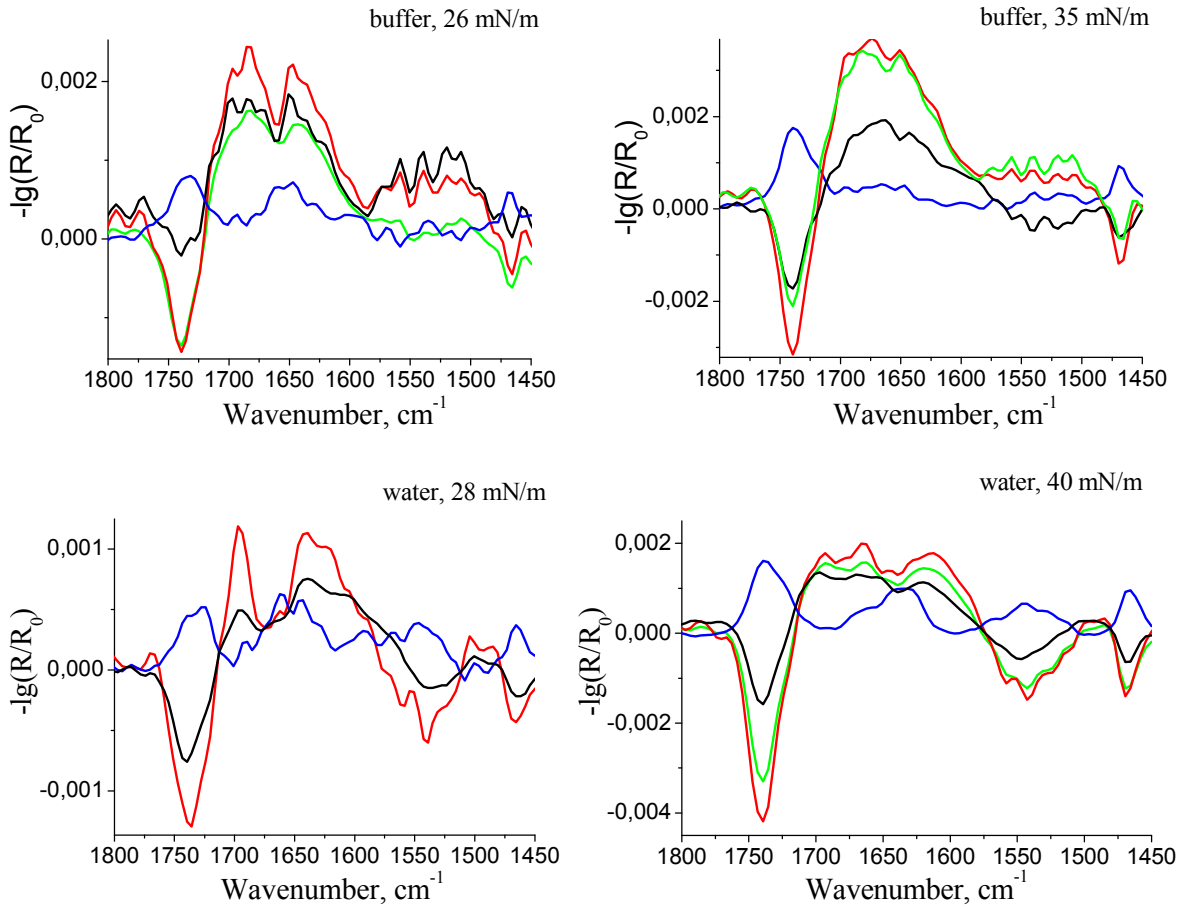

Figure 5.16. *IRRA spectra of B18 (c = 1,25 mg/L) adsorbed to the DPPG monolayer on buffer (top) and on water (bottom) at initially 0 mN/m and final 26 and 28 mN/m for buffer and water, respectively, (left) and compressed to higher lateral pressure (right). The spectra were acquired with s- (black lines) and p-polarized light (colored lines). The spectra obtained with p-polarized light were taken at 62° (blue line), 32° (green line) and 40°(red line) of the incident beam to the surface normal.*

Compression of the monolayers leads to the peptide squeezing out, the amide bands disappear from IRRA spectra of DPPC on B18 in water, buffer and buffer with zinc, and of DPPG on buffer (Figure 5.16). The peptide remains adsorbed (or probably penetrated) to a DPPG monolayer on water. The relative intensity of amide bands (compared to the C=O stretching of lipid) is slightly decreased and its position is shifted to lower wavenumbers. Obviously the B18 adopts a badly correlated β-sheet structure, being adsorbed to the DPPG on water at high surface pressure. The conformational change can appear during compression of the monolayer. Another possibility is that the intercalated peptide in α–helical conformation is squeezed out from the monolayer and only the peptide, adsorbed on the DPPG headgroups due to electrostatic attractions and adopting the β-sheet structure, remains.

IRRAS provides information about the lipid phase state, hydration and ionization degree

at the interface. During adsorption to the DPPC on water, buffer and buffer with zinc, the lipid undergoes the phase transition from a liquid phase to a condensed phase at the same surface pressure as in pure DPPC monolayer (Figure 5.17). The condensation is complete (no liquid phase remains) since the asymmetrical and symmetrical stretching modes are the same for a pure lipid monolayer and one with adsorbed peptide. The phosphate and carboxilate stretching bands are not influenced by the peptide adsorption.

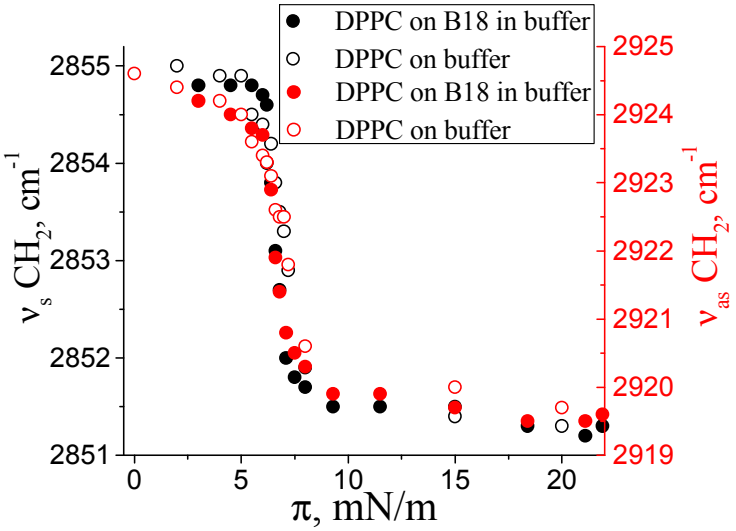

Figure 5.17. *Positions of CH_2 asymmetrical and symmetrical stretching modes versus the surface pressure during compression of the pure DPPC monolayer on buffer and during the peptide adsorption to the DPPC monolayer at initially zero surface pressure in the same buffer.*

In contrast, adsorption of B18 to the DPPG monolayer results in the fluidization (larger amount of gauche conformers) of lipid aliphatic chains. CH_2 symmetrical and asymmetrical stretching modes were observed at larger wavenumbers (2855 and 2853 instead of 2851 cm^{-1}, 2924 and 2922 instead of 2918-19 cm^{-1} for DPPG on water and buffer respectively) (Figure 5.18). The intensities of all lipid bands with the adsorbed peptide are much smaller than for pure lipid because of the low surface density of the lipid. However, it can be clearly seen that the phosphate bands in the case of DPPG on water have a different shape and their relative intensities (to the CH_2 stretching bands) are increased. This indicates that the DPPG monolayer is much more ionized in the presence of the peptide than on pure water.

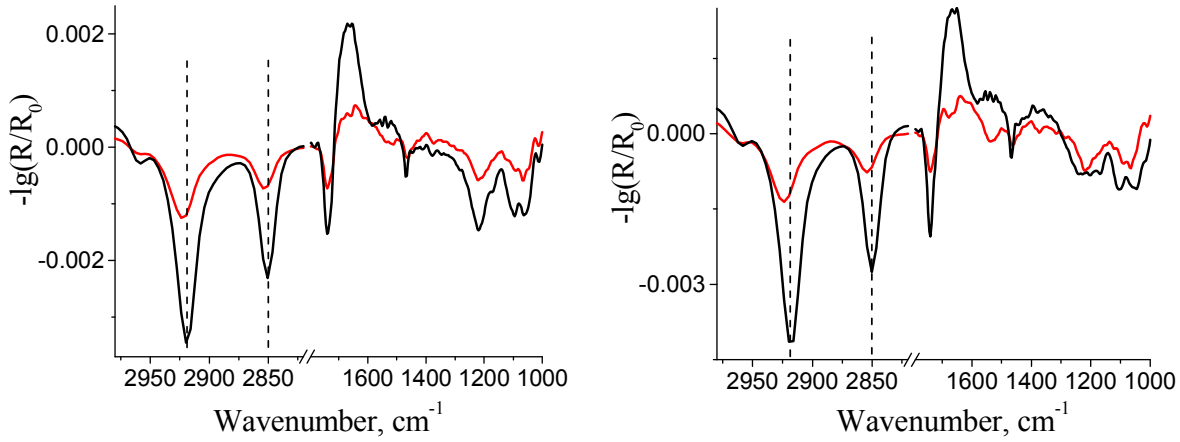

Figure 5.18. *IRRA spectra of DPPG monolayer on buffer (left) and on water (right) at 30 mN/m (black lines) and the spectra of DPPG with adsorbed B18 at 26 and 28 mN/m for DPPG on buffer and on water respectively (red lines) in the region of CH_2 and PO_2^- stretching bands.*

5.3 Discussions

The present CD data support previous observations. Both programs to estimate the peptide secondary structure show the largest content of random coil in water and buffer (first dissolved in water), the largest β-sheet content for the B18 directly dissolved in buffer and the largest α-helical content for B18 in HFIP and in buffer at pH 7.4 with zinc. It is revealed that in the presence of negatively charged SDS and DMPG vesicles the peptide adopts partly helical partly β-sheet conformation. The peptide prefers to be in the α-helical or the β-sheet conformation in more hydrophobic environment. The choice between these two structures probably depends on the peptide concentration and solvent properties. Since formation of the β-sheet structure is possible only if the peptide aggregates, its formation is concentration and time dependent. The electrostatic interactions with SDS and DMPG stabilize the peptide interactions with the SDS and DMPG hydrophobic chains, and the α-helical structure becomes preferential. It is also possible that the peptide partly forms the β-sheet structure because of the increased surface concentration.

B18 is an amphipathic peptide and therefore it adsorbs to the air/water or buffer interface. Since it is less charged at pH above 7 and therefore more hydrophobic, its surface activity is higher in buffer than in water. B18 adopts the α-helical conformation at the interface independent of the pH in the subphase. Obviously in the hydrophobic environment the peptide prefers the α-helical conformation. This behaviour is completely different from that of Aβ. As revealed by

IRRAS simulations, the helix long axis is aligned almost horizontal (along the surface). If one assumes that the structure proposed in [21] is correct then the kink with charged amino acids should point toward the water and the two helical parts with mostly hydrophobic amino acids should align along the surface with slight tilt, that allows withdrawing of hydrophobic residues away from the water. The angle between helices should be far above 90 degrees, because both helical parts of the peptide have only a small tilt from the horizontal orientation (Figure 5.19). It is also possible that the helix in the C-terminus of B18 is aligned horizontally, due to its more hydrophilic character while the N-terminus is tilted from the horizontal orientation in order to avoid interaction with water.

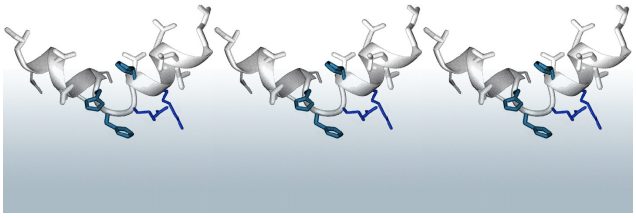

Figure 5.19. *Schematic representation of the B18 adsorbed at the air/water interface The peptide adopts an α-helical conformation at the interface.*

The presence of the DPPC monolayer does not influence the B18 structure at the interface and even more the presence of the B18 does not influence the lipid structure and phase behavior – the peptide acts as a mechanical "barrier". It inserts into the monolayer at low surface pressure and adopts the α-helical structure. It occupies the space in the monolayer and compresses the lipid molecules and this induces the phase transition in the lipid monolayer. Apparently the peptide is not mixed with the lipids in the condensed state, because in the opposite case, the inserted peptide should perturb the hydrophobic attraction between neighboring DPPC chains and formation of condensed phase (domain size and shape) would be affected by the peptide if it would be formed at all. At the same time the peptide should be homogeneously distributed in the DPPC monolayer in the liquid state since no domains of the peptide occur below the lipid phase transition. Figure 5.20 schematically depicts the possible arrangement of B18 and DPPC molecules at the air/water interface. Such phase separation between peptide and lipid in the condensed phase was observed for other peptides as well [85, 86]. Since compression of such mixed B18/DPPC films to higher surface pressure (above the equilibrium pressure of the pure peptide layer) leads to a complete squeeze out of the B18 and the peptide signal disappears from

the IRRA spectra as well, one can conclude that there is no adsorption of the peptide to the DPPC headgroup. The last is supported by the fact that the DPPC phase behaviour and structure is unaffected by the peptide. The lipid chains in the border between the peptide and lipid condensed domains might be fluid because there are no neighbouring alkyl chains to stabilize the all-trans conformation. Unfortunately, this fact is difficult to prove by IRRAS since the amount of lipid on the edge of the lipid condensed domain (if one assumes the size of a domain is around 30 μm in diameter) is less than 0.1 % of the total amount of lipids.

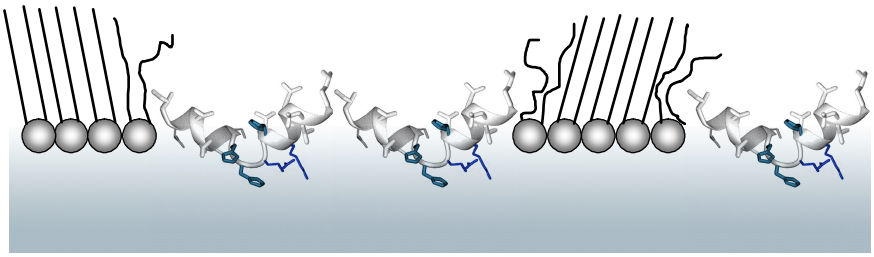

Figure 5.20. *Schematic representation of the B18 insertion into the DPPC monolayer at initially zero surface pressure.*

Additionally, the presence of zinc in the subphase stabilizes the peptide at the air/water interface, but does not lead to the binding of the peptide to the DPPC head group and to another peptide. In the presence of zinc, the peptide insertion into the uncompressed DPPC monolayer leads to a larger surface pressure increase. Zinc probably stabilizes the α-helical structure of the B18 that is more hydrophobic than the random coil structure. However, the phase behavior of DPPC remains unchanged and the peptide is squeezed out under compression indicating no interaction between lipid and peptide. This can explain the increased fusogenic properties of B18 in the presence of zinc. The peptide probably intercalates into the chain region because it avoids interactions with water due to the increased hydrophobicity and destroys the vesicle.

Opposite to the DPPC monolayer, insertion of B18 into the DPPG monolayer on buffer and on water changes the lipid phase behaviour. The B18 is positively charged and DPPG is negatively charged, therefore the peptide can interact electrostatically with DPPG. The interaction between lipid and peptide does not allow complete phase separation; therefore the DPPG chains are more fluid (have more gauche conformers). The peptide insertion into the DPPG monolayer on buffer leads to the formation of condensed domains, but their size is much smaller compared to those of the pure lipid. Interestingly the interactions between B18 and DPPG are much more pronounced on water than on buffer. This is very similar to the Aβ/DPPG interactions. It is possible that in the case of pH 7.5 and 100 mM NaCl, the sodium counter ions

screen the DPPG charge and do not allow adsorption of the peptide to the lipid. Being inserted into the DPPG monolayer, the peptide can interact electrostatically with the lipid and disturbs the condensed phase formation, although the structure of B18 is dictated by the hydrophilic/hydrophobic interface and is similar to that of a pure peptide layer at the air/water interface (Figure 5.21).

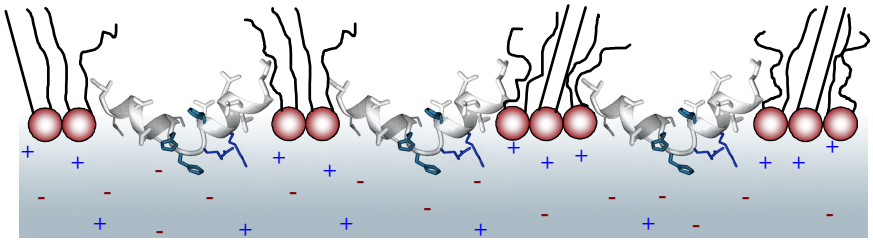

Figure 5.21. *Schematic representation of the B18 insertion into the DPPG monolayer on buffer with pH 7.4 at initially zero surface pressure. The lipid is assumed to be fully charged at pH 7.4 and 100 mM NaCl.*

On the contrary, the DPPG monolayer is only slightly charged on pure water but the counterion concentration in pure water is also very low (~10^{-6} M) and they (counterions) are not able to screen the DPPG charge. Thus B18 is not only inserted into the monolayer but it also adsorbs to the DPPG headgroup forming the diffuse double layer or even Stern layer, winning against small counterions (protons). The structure of this adsorbed B18 is not any more α-helical - the peptide apparently adopts the β-sheet or random coil conformation. At a low surface density of the lipid B18 is partly inserted into the monolayer and partly adsorbed to the DPPG headgroup (Figure 5.22). Therefore, the IRRAS reveals random coil or α-helical structure of B18. The DPPG chains are more disordered indicating the better miscibility between the peptide and lipid under these conditions.

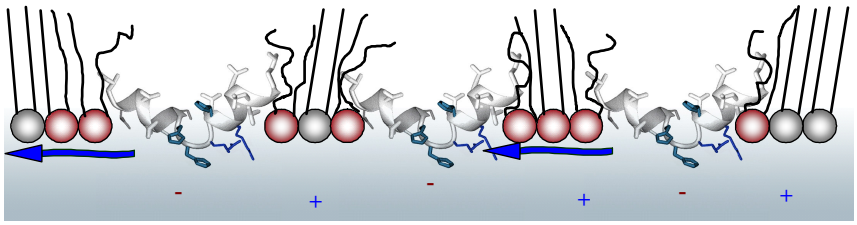

Figure 5.22. *Schematic representation of the B18 insertion into the DPPG monolayer on water at initially zero surface pressure. The lipid is assumed to be partly charged on water. The peptide is not only inserted into the monolayer but is also adsorbed onto it owing to its positive charge and poor screening of the monolayer charge by protons.*

Compression of the complex film leads to the squeezing out of the inserted B18

molecules from the monolayer, nevertheless the peptide adsorbed onto the DPPG via electrostatic interactions remains (Figure 5.23).

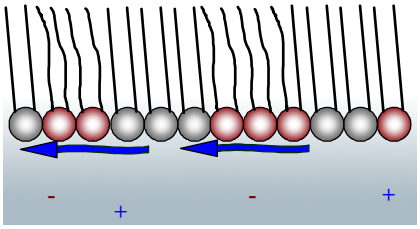

Figure 5.23. *Schematic representation of B18 adsorption to the DPPG monolayer on water at high surface pressure. The lipid is assumed to be partly charged on water. The peptide adopts partly β-sheet partly random coil conformations. The peptide is adsorbed via electrostatic interactions owing to low counterion concentration.*

The secondary structure of the adsorbed peptide is different from that of the inserted peptide due to the polar environment in the vicinity of the DPPG headgroups. Obviously in these conditions the peptide forms short poorly correlated β-sheets with β-turns and unstructured parts. It is also possible that during compression the peptide surface concentration is increased, which leads to aggregation. Additionally the peptide increases the surface pH that leads to the larger ionization state of the DPPG monolayer in the presence of B18 than on pure water. This should lead to a larger tilt of the DPPG chains. On the other hand the peptide is a multi-charged ion and, similar to calcium, can bring DPPG molecules closer to each other decreasing the chain tilt. Hence these two effects may compensate each other and the DPPG structure on B18 in water resembles that on pure water. Some parts of the peptide can still disturb the hydrophobic region of the DPPG monolayer, especially close to the headgroup region of the lipid. Therefore diffraction peaks observed in GIXD are much broader and the cross-sectional area of the chains is larger on the B18 than in the absence of it.

6. Interactions of Aβ (1-40) peptide with lipid monolayers

6.1. Introduction

Alzheimer's disease is characterised by the presence of amyloid plaque in the brain. The major components of this plaque are small peptides of 39-43 amino acids – amyloid β peptides (Aβ). The most common are the peptides with 40 and 42 amino acids. The more hydrophobic 42-residue peptide is thought to play a seed role in plaque formation. However the 40 amino acid peptide can precipitate in the absence of longer peptide as well. Aβ peptides are the products of proteolytical cleavage of a membrane-anchored protein – amyloid precursor protein (APP) [87]. The peptides are amphipathic; they include transmembranic and extracellular parts of APP. Normally they are present in cerebravascular fluids and blood in a soluble form [88]. During aging or as a result of disease they precipitate into amyloid fibrils. This process is thought to include the conformation change of soluble Aβ (either in random coil or α-helical conformation) to β-sheet strains [89-92]. The fibrils are proven to be neurotoxic [93]. However the mechanisms of their toxicity as well as of their formation are still unclear. Many factors influence these processes. Overexpression of Aβ (1–42) can accelerate fibril formation [94]. A change in the membrane composition can induce a conformation change in Aβ or vice versa the peptide can influence membrane properties such as fluidity, permeability and curvature [95-100]. It was also reported that Aβ takes part in neuroinflammation and oxidation processes [101].

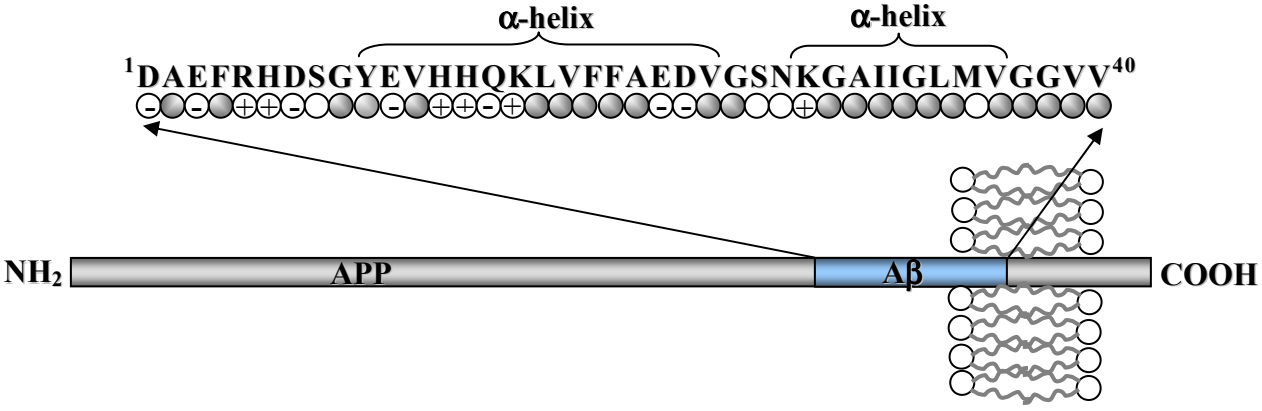

Figure 6.1. *Schematic representation of the Aβ (1-40) peptide location in APP protein and its primary structure and secondary structure in membrane mimicking conditions (obtained from NMR data). Grey circles show non-polar amino acid residues, while white circles correspond to polar and charged residues.*

In order to understand the pathway and cause of Aβ deposition in brain, plenty of investigations were done *in vitro*. In the nineties the structure of synthetic Aβs in different solvents was elucidated using mostly CD and NMR techniques [102, 103]. The data revealed that at pH values below 4 as well as above 7, Aβ peptides adopt predominantly a random coil conformation, while at the intermediate pH, they form β-sheets [104]. At this intermediate pH Aβs are neutral; their isoelectric point (pI) can be estimated as 5.8. Under these conditions the aggregation is more favourable compared to the solutions with low and high pH, due to the decreased repulsion between neighbouring peptide molecules when they have no net charge. Addition of fluoroalcohols, such as hexafluoroisopropanol (HFIP) and trifluoroethanol promotes formation of the α-helical structure of Aβ peptides. Aβs dissolved in HFIP do not form aggregates even after long storage time. Moreover, the pre-treatment with HFIP is reported to be essential for obtaining reproducible results dealing with Aβ peptides [18, 105]. SDS (sodium dodecylsulphate) micelles are also able to induce the α-helical structure of Aβs. ^{1}H-NMR data revealed two helix regions in Aβ that is interacting with SDS micelles or dissolved in TFE or HFIP. In the presence of SDS micelles Aβ (1-40) peptide forms helices from 15-24 and 28-36 residues, with an unstructured NH-terminus and a kink formed by 25-27 residues [106]. It was also shown by other authors that Aβ (1-42) consists of two helixes (Tyr10-Val24 and Lys28-Ala42) with loop region (Gly25-Asn27) and an extended chain at the NH terminus [107]. The helical structure is unstable between residues Tyr10-His14 and Gly37-Ala42 and these regions may exist as an ensemble of α-helix and unfolded structure. Thus it was concluded that Aβ (1-42) and Aβ (1-40) have no significant structural difference in membrane-mimicking conditions. Since Aβs show fast NH –ND exchange it was suggested that they are located at the micelle surface and do not become embedded within the hydrophobic interior of the micelle. However it is possible that the hydrophobic region of Aβs undergoes rapid movement, inside and outside the micelle interior.

The synthetic amyloid peptides and their fragments have a high tendency to aggregate with time in vitro; they form fibrils similar to those found in the brain of patients with Alzheimer's disease, which show a significant neurotoxicity. The process of fibril formation was intensively investigated in the last decade by solid-state NMR, Atomic Force Microscopy (AFM), Electron Microscopy, X-ray analysis, Light Scattering technique etc. It was shown that fibrils are approximately 5-10 nm in diameter and have an axial crossover spacing of 25-27 nm. X-ray

diffraction revealed two major repeat distances: 4.7-4.8 Å in the meridian position that is the distance between hydrogen bonded units in a β-sheet, and ~ 10 Å in equatorial positions that can be attributed to the distance between neighboring β-sheets [108]. Recent NMR data revealed that fibrils are formed from parallel β-sheets [109, 110] and not antiparallel ones as proposed earlier. The kinetics of Aβ aggregation depends on the peptide concentration, pH and ionic strength [105, 111]. The acceleration of fibril formation was observed in the presence of lipids [100], seeding by preformed fibrils [91, 92], or by shaking the Aβ aqueous solutions [112]. The rate of aggregation varies from 30 minutes at high Aβ concentration, pH 5-6 and intensive shaking of peptide in solutions, to several weeks at low Aβ concentration and pH above 7. The concentration of Aβ (1-40) peptide that provides the fibril formation in reasonable time (up to few weeks) was found to be 10-50 μM. However, small aggregates can be formed even at lower peptide concentration [105]. Additionally, studies of Aβ fibrilization *in vitro* revealed that fibrilogenesis proceeds in two stages: formation of intermediate aggregates followed by development of fibrils [91, 92, 105]. The peptide aggregation and fibrilization include a conformational transition of Aβ from predominantly random coil to β-sheet-rich form during which a transitory α-helical component is observed [91]. These intermediates with high α-helical content show even higher neurotoxicity than the mature fibrils.

There are many researches focused on the membrane/Aβ interactions. Due to its amphipathic nature, Aβ can interact with membranes. Such interactions may play a significant role in the pathogenesis of Alzheimer's disease. Previous investigations revealed the influence of the charge of lipids on the secondary structure and aggregation properties of the peptide. Most researchers agreed that neutral membranes have no effect on the peptide whereas negatively charged membranes induce the conformational change of Aβ from a random coil to α-helix or to β-sheet structure with further aggregation [81, 82]. Presence of ions [113], ratio between lipid and peptide [81, 82], as well as presence of cholesterol and gangliosides [99, 114, 115] influence the change in the peptide secondary structure. Langmuir monolayer techniques can help to understand the mechanism and nature of Aβ/membrane interactions and their consequences for the peptide and lipid structure.

6.2 Results:

6.2.1 Aβ (1-40) structure in aqueous solutions

Aβ (1-40) peptide adopts random coil conformation in water or buffer with pH 7.4 at concentrations below 10 μM as was previously shown. However, the history of the peptide and its source is important for obtaining the monomeric unstructured peptide at least in the starting stage. The results obtained reveal that commercial Aβ in wide range of pH and even in pure water, except the very basic pH conditions (more than pH 10), has a mixed β-sheet/α-helical structure that is characteristic for amyloid aggregates [91]. Therefore, in most of our experiments the pre-treatment procedure with HFIP was applied (see Materials and Methods). The spectra of Aβ directly dissolved in water, dissolved in HFIP and dissolved in water after HFIP pre-treatment are shown in Figure 6.2, left. The peptide apparently adopts random coil conformation after the pre-treatment procedure. The Aβ peptide has many ionisable amino acid residues, thus the pH influences its secondary structure and aggregation ability. The presented CD-data (Figure 6.2 right) reveal that at low and high pH the peptide is unstructured while it forms β-sheets at intermediate pH 5-6. As it was mentioned before, in highly basic conditions at pH well above 10, the peptide adopts a random coil structure even without pre-treatment with HFIP [116]. The content of certain secondary structure motifs for all presented CD-spectra are shown in Table 6.1. MLR and Continll programs give different result, although the major trends in the secondary structure changes are revealed with both programs.

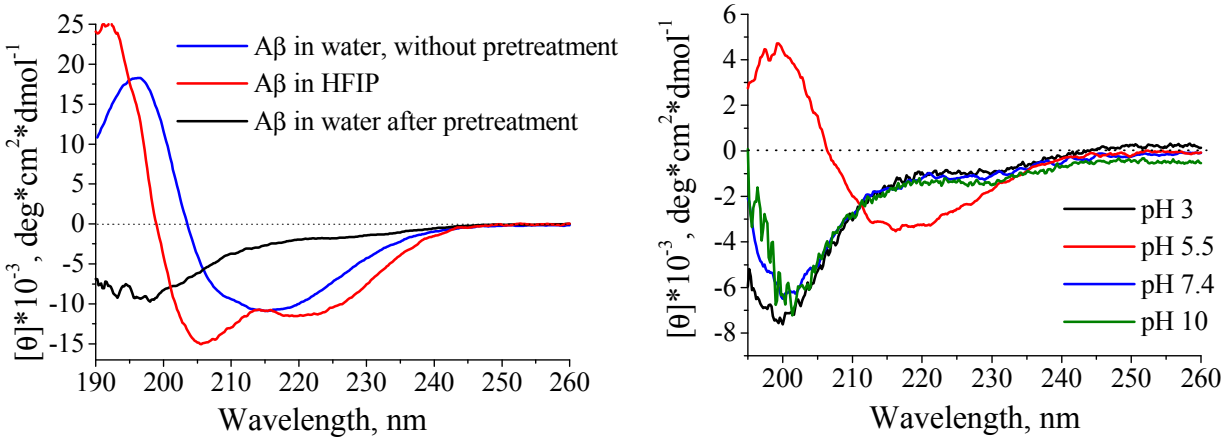

Figure 6.2*.CD-spectra of Aβ (1-40) peptide in different solutions. Left: Aβ directly dissolved in water, Aβ in HFIP and Aβ in water after pre-treatment with HFIP; right: Aβ after pre-treatment in aqueous solutions with various pH.*

Table 6. 1.

The content of secondary structure motifs for different Aβ solutions obtained with two different programs from presented CD-data.

solution	Method	Secondary structure motifs, %			
		α-helix	**β-sheet**	**turn**	**random**
Directly dissolved in water or buffers at pH < 10	Continll	27	30,1	18,7	24,1
	MLR	17,2	33,2	16,5	33
in HFIP	Continll	42,5	12,6	18,8	26,1
	MLR	61,9	-	0,3	37,8
Dissolved in water or buffers at pH < 4 and pH > 7 after HFIP pretreatment	Continll	2,5	19	11,9	66,6
	MLR	5,8	5,6	38,3	50,3
In the presence of SDS micelles	Continll	40,6	11,9	22,9	22,6
	MLR	31,2	28,7	-	40,2
In the presence of DMPC vesicles at P/L = 1/65	Continll	2,5	42,2	18	37,3
	MLR	22,4	8,9	2,2	66,5
In the presence of DPTAP vesicles at P/L = 1/38	Continll	4,6	39,4	23,8	32,2
	MLR	18,9	52		29,1
In the presence of DMPG vesicles at P/L = 1/26	Continll	9,7	38,3	23,9	31,1
	MLR	18,7	52		29,3
In the presence of DMPG vesicles at P/L = 1/65	Continll	15,6	32,1	18,5	33,8
	MLR	61,2	-	10,2	28,6
In the presence of DMPG vesicles at P/L = 1/260	Continll	17,3	25,9	17,3	39,5
	MLR	33,8	12	2,2	66,5

Aβ adopts the α-helical structure in the presence of SDS micelles as many other peptides. Therefore, it was suggested that it should adopt the α-helical conformation in the presence of negatively charged lipid vesicles as well. Terzi et al [81] and Bokvist et al [82] demonstrated that it is only partly true. The structure of Aβ peptide depends on the lipid to peptide ratio. It folds into β-sheets at high peptide to lipid ratio and it forms the α-helix at low ratio. These observations are confirmed in the present studies (Figure 6.3). It is obvious that the peptide adopts a random coil structure in the presence of neutral DMPC vesicles, β-sheet or α-helical structure with negatively charged DMPG vesicles and it folds into β-sheets in the presence of positively charged DPTAP vesicles. However, it was impossible to measure the CD-spectra of Aβ/DPTAP samples at high lipid to peptide ratio because of strong light scattering.

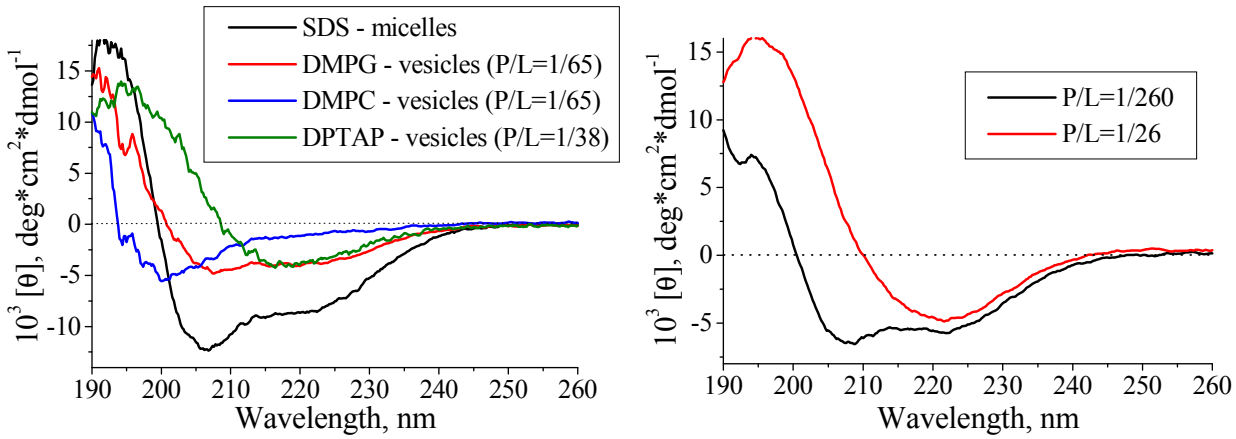

Figure 6.3. *CD-spectra of Aβ in the presence of SDS micelles, DMPG, DMPC and DPTAP vesicles (left) and spectra of Aβ in the presence of DMPG vesicles at P/L ratio of 1/26 and 1/260 (right).*

6.2.2. Adsorption of Aβ (1-40) peptide at the air/water interface and on lipid monolayers

Since Aβ is an amphiphilic peptide, it has a pronounced surface activity. The adsorption to the air/water interface leads to a decrease of the surface tension. The largest value of equilibrium surface pressure was measured for the untreated peptide and reaches 20 mN/m. The adsorption kinetics strongly depend on the solution properties such as pH, ionic strength and what is even more confusing it varies from batch to batch and depends on the history of the solution as well as on the trough material (teflon or glass) and its shape. The peptide simultaneously adsorbs at the air/water interface and on the Langmuir trough walls. The last is seen because the wettability of the Teflon walls by water in the presence of the peptide increases drastically. The glass vessel used for adsorption has a different shape than the Teflon trough; the ratio between the bulk volume and the surface area is larger.

The aging of the peptide solution probably leads to Aβ aggregation and reduced surface activity, either because of the precipitation of the peptide or because of a slower diffusion of amyloid aggregates with high molecular weight. Apparently, the peptide without pre-treatment is more surface-active but it loses its activity also very fast. An explanation could be that the existing β-sheets are more surface active than the random coil. On the other hand, β-sheets form larger aggregates with time, which leads to the loss of surface activity. Considering all this, precise information about the adsorption properties is not available and more detailed investigation is needed. The summary of the results obtained for the same peptide concentration in pure water and for various conditions is shown in Figure 6.4.

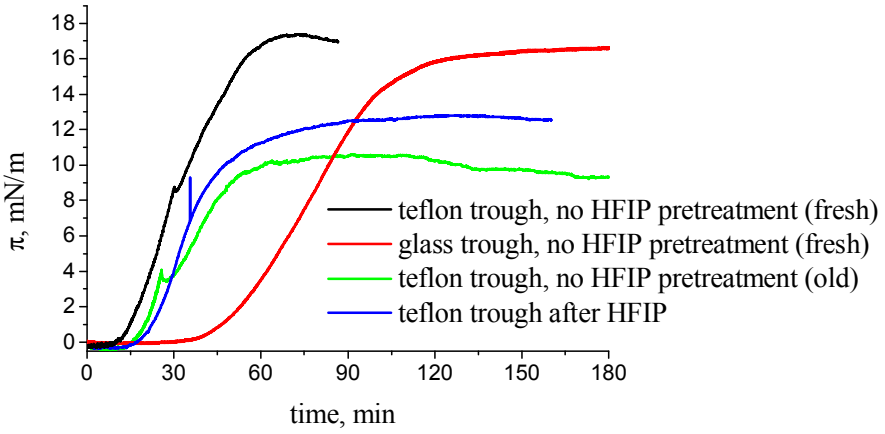

Figure 6.4. *Adsorption kinetics of Aβ to the air/water interface at different conditions. The peptide concentration is 0.58 μM.*

Taking into account the observed dependence of the adsorption kinetics from all these factors, we have established a defined pre-treatment procedure, used only freshly prepared solutions and compared only results for the same peptide lot. Within the same lot the adsorption kinetics is concentration dependent (Figure 6.5), and the peptide has a more pronounced surface activity in buffer solutions than in water. This phenomenon was independently observed by the group of K.Y. Lee [117]. The pH and ionic strength are very important. The peptide has a larger surface activity at low pH and higher ionic strength than at high pH (with minimum activity at pH 5-6) and low ionic strength.

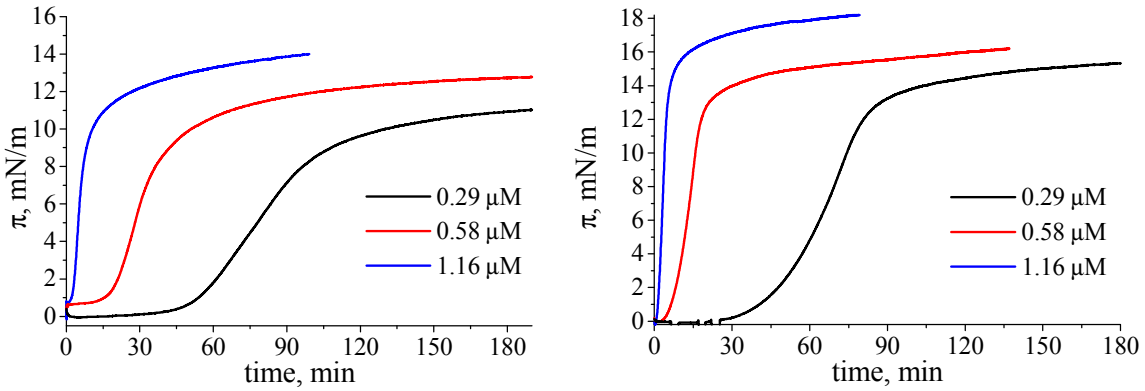

Figure 6.5. *Adsorption kinetics of Aβ to the air/buffer interface: phosphate buffer, pH 7.4 – left and sulphuric acid, pH 2 – right.*

In order to study Aβ/membrane interactions lipid monolayers at the air/water interface have been used as model systems. Three types of experiments have been performed: a) the initial surface pressure (before addition of the peptide) is zero and the large area per lipid molecule is kept constant, b) the lipid monolayer is compressed to 15 – 20 mN/m (the equilibrium surface

pressure of the peptide adsorbed to the pure air/water interface) before addition of the peptide and the increase of the surface pressure during the peptide insertion is recorded (the area is kept constant), c) the lipid is compressed to 30 mN/m before addition of the peptide, and this pressure is kept constant during the peptide adsorption by adjusting the area with a moving barrier. The pressure of 30 mN/m was chosen because there is a long standing discussion that it corresponds to the pressure in lipid bilayers [118].

During adsorption of the peptide to a lipid monolayer the surface pressure increases from zero to the so-called equilibrium pressure (plateau). The equilibrium pressure in the case of zwitterionic lipids is similar to that observed for the peptide adsorption at the pure air/buffer interface, and is lower compared to negatively and positively charged lipids. The last points to specific interactions of the peptide with anionic or cationic lipids. This is not surprising since the peptide has both positively and negatively charged residues. The increase of the surface pressure in the presence of lipids is much more pronounced and much lower peptide concentration is required to achieve the final pressure of 18-20 mN/m after several hours of adsorption. The last can be explained by the fact that the peptide occupies only the lipid free area and compresses the lipids. The other interesting phenomenon observed during the peptide adsorption is the plateau region observed in the kinetics curves of the peptide adsorption to DPPC (Figure 6.6) and DMPE monolayers. The surface pressure of the plateau is similar to the transition pressure from LE to LC phase in the compression isotherm of pure lipids and this resembles adsorption of the B18 on the DPPC monolayer.

In order to prove that the plateau observed in the adsorption kinetics curve is due to the lipid phase transition, adsorption of Aβ to lipid monolayers was followed by Fluorescence Microscopy (FM). The adsorption kinetics to the DPPC monolayer and corresponding FM images are shown in Figure 6.6. During Aβ adsorption, the dark domains appeared in the plateau region indicating condensation of the lipid. The size of ~30 μm and the shape of the domains are similar to that of pure DPPC (Figure 5.5). The only difference observed was that the domains do not grow and do not occupy the whole surface after the transition is completed. Summarizing these observations, one assumes that during adsorption the peptide occupies free space in the lipid monolayer, compresses the lipids and induces the phase transition. Since the domain and the transition pressure are similar to those for the pure lipid monolayer, one can conclude that the peptide does not specifically interact with DPPC and is probably immiscible with the condensed lipids. The fact that domains stop to grow after the transition is completed can be explained by

only partial formation of a condensed phase. The area occupied by dark domains is still smaller than the bright area indicating that lipids surrounding the peptide remain in the liquid-expanded phase. In order to clarify this assumption IRRAS was used and the obtained results will be presented later.

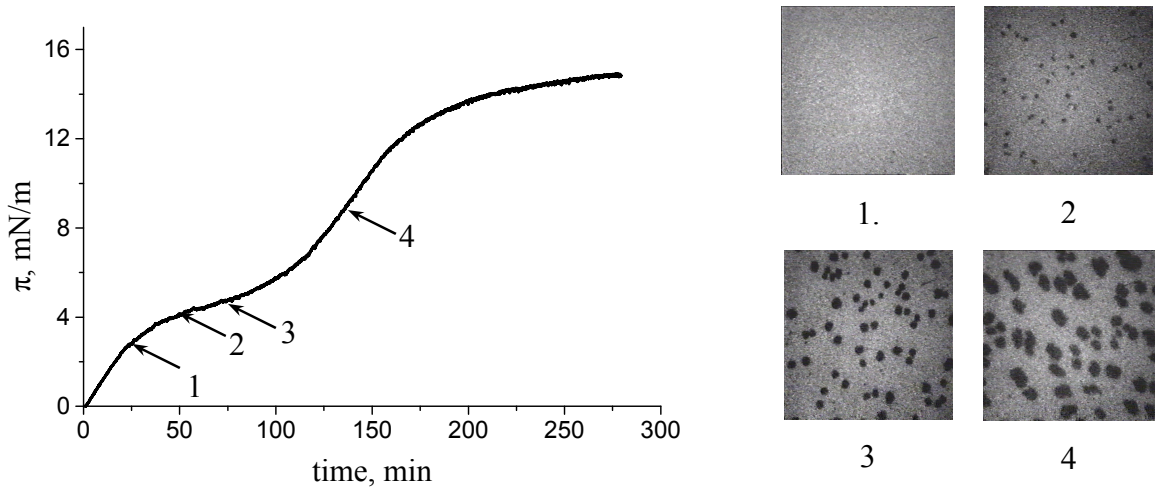

Figure 6.6. *Adsorption isotherm of Aβ (1-40) peptide to a DPPC monolayer with 1% fluorescence label on buffer and corresponding fluorescence microscopy images. The peptide concentration is 0.185 μM. The image size is 280x300 μm².*

After reaching an approximately constant pressure value, the monolayer was compressed. At 30 mN/m the peptide is squeezed out from the monolayer, which is seen as a plateau in the compression isotherm (Figure 6.7).

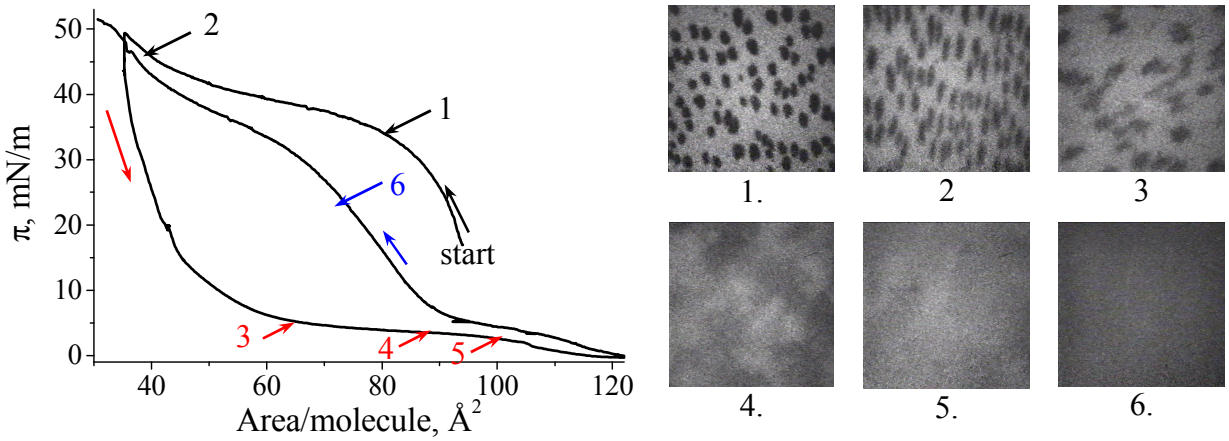

Figure 6.7. *Compression and expansion isotherm of 1% fluorescence-labelled DPPC monolayer with adsorbed Aβ on buffer and corresponding fluorescence microscopy images. 1-st compression is shown by black arrows, expansion by red arrows and 2-nd compression by blue arrows. The bulk peptide concentration in buffer at pH 7.4 is 0.185 μM. The image size is 280x300 μm².*

Interestingly, domains are not growing but instead are elongated in the direction perpendicular to compression. Further expansion of the film leads to a re-insertion of the peptide

at surface pressures below 20 mN/m. The domains disappear in the plateau region, which indicates the LC-LE transition. During re-compression they cannot be observed. Probably the peptide increases the viscosity of the monolayer and therefore the lipids cannot easily diffuse to form big domains as they still could do during adsorption because the peptide surface concentration is smaller and not altered. The first amyloid 'islands' probably are small but with time they can interact with each other producing larger aggregates.

Similar results were obtained with another zwitterionic lipid – DMPE that has the phase transition at 6 mN/m at 20ºC (data not shown). In general the same behaviour was observed during Aβ adsorption to negatively charged DPPG. The DPPG monolayer on water at 20 ºC has no LE-LC transition: it is condensed in the whole surface pressure range. To obtain the phase transition, the Aβ adsorption was measured at 35 ºC. At this temperature the phase transition is observed at 7 mN/m. During Aβ adsorption, hardly any plateau is visible (Figure 6.8). Despite of this, the domains are formed at the phase transition pressure and are not increasing in size. The small amount of domains could also indicate that in this case the transition may be not completed.

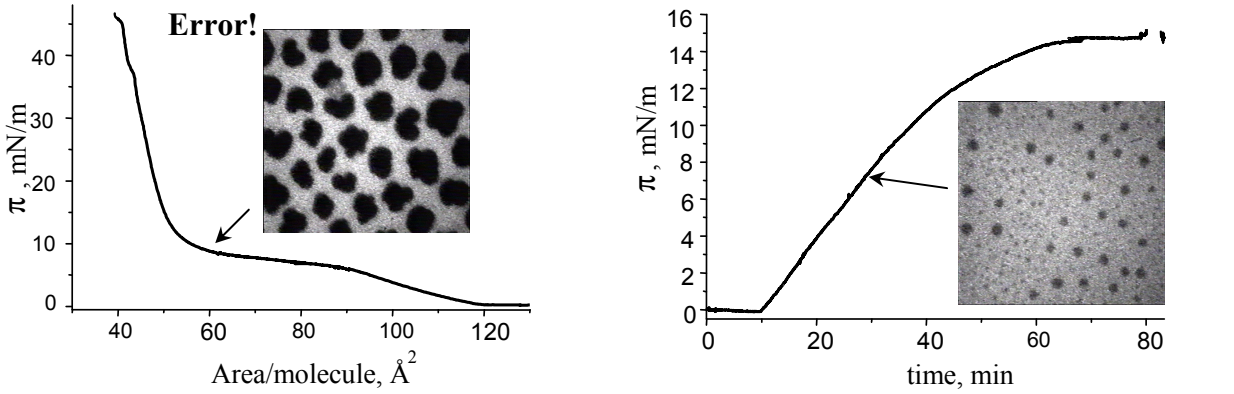

Figure 6.8. *Compression isotherm of the DPPG monolayer on water (left) and adsorption isotherm of Aβ peptide to a DPPG monolayer with 1% fluorescence label on water (right) at 35ºC and corresponding fluorescence microscopy images. The peptide concentration is 0.185 μM. The image size is 280x300 μm².*

The DPPG monolayer on the buffer used (phosphate buffered saline, 100 mM NaCl, pH 7.4) has a phase transition at 9 mN/m at 20 ºC. The domains formed in the pure monolayer are small. The adsorption kinetics is similar to that on pure water and the plateau is hardly seen. The small domains formed can be clearly seen (Figure 6.9).

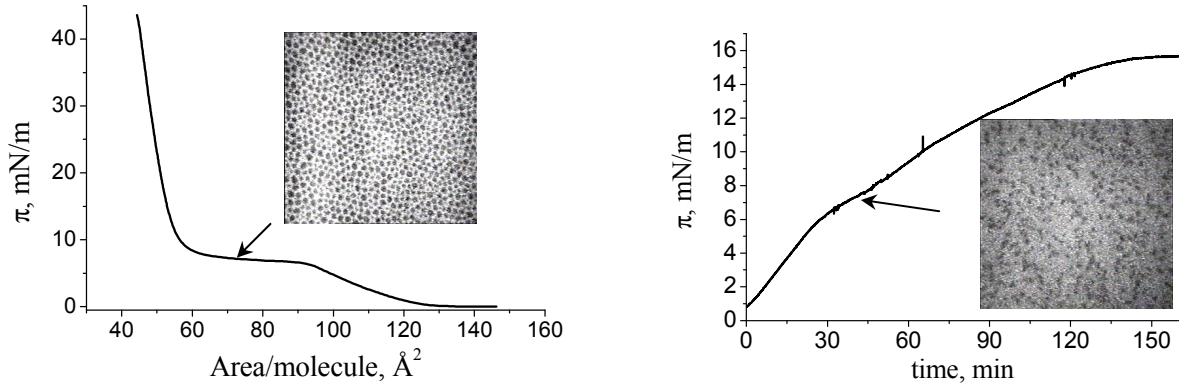

Figure 6.9. *Compression isotherm of the DPPG monolayer on buffer containing 10 mM Hepes, 100 mM NaCl (left) and kinetics of Aβ adsorption to 1% fluorescence-labelled DPPG monolayer on the same buffer (right) at 20ºC and at initially zero surface pressure and corresponding fluorescence microscopy images. The peptide concentration is 0.185 μM. The image size is 280x300 μm².*

Compression of the DPPG monolayer leads to the peptide squeeze out at surface pressures above 30 mN/m as it was observed for the DPPC monolayer. Similar behaviour during adsorption and following compression is observed for all studied lipids: liquid DMPC and POPG, lipids with a phase transition from LE to LC phase as DPPC, DMPE, DMPG, DPPG, DPTAP and lipids exhibiting only a condensed phase under experimental conditions as DPPS, DPPE. When the monolayer on pure water is compressed to 30 mN/m before peptide addition into the subphase and is kept constant during peptide adsorption, the peptide insertion leads to an increase of the monolayer surface area in the case of charged lipids and remains unchanged in the case of zwitterionic monolayers. The area increase is not observed if the subphase contains salt or/and buffer. Similar results were published by Ege and Lee [117].

The authors have shown that the peptide can insert into the charged DPPG and DPTAP monolayers when it was injected under these monolayers compressed to 30 mN/m or 25 mN/m. In these experiments instead of the area, the surface pressure was kept constant. Adsorption experiments were performed at 30 ºC. It was shown that an increase of the monolayer area after Aβ injection is much smaller at 30 mN/m than at 25 mN/m. Additionally, the area increase on phosphate buffered saline subphase with 120 mM NaCl and pH 7.4 is not significant at all (less than 2 % for DPPG and 4% for DPTAP). The peptide insertion into DPPG and DPTAP monolayers at 25 mN/m was followed by fluorescence microscopy as well as in the present work. It was observed that in the case of charged lipids, the bright area in the fluorescence images increases during the peptide insertion. The shape of the condensed phase domains is not changed for the DPPG monolayer and the domains are deformed and coalesced for DPTAP. The bright

area increase can be easily understood because the monolayer area also increases at 25 mN/m; for example, this increase exceeds 100 % on pure water. The change of the DPTAP domains shape may be a result of the influence of the peptide on the DPTAP phase transition pressure that is very close to 25 mN/m at 30 ºC. The influence on the DPPC domain shape at 25 mN/m is small since the peptide is not inserting into this monolayer at such high surface pressure. Therefore their results are in a good agreement with the present observations. The peptide does not insert into the zwitterionic DPPC monolayer at high surface pressures, although it is stabilized at the interface when inserted into charged monolayers at a surface pressure above the equilibrium pressure for pure peptide films. At modest salt concentration in the subphase, the peptide insertion into charged monolayers at 30 mN/m hardly occurs.

Additionally, it was demonstrated by other authors [119] that if the monolayer was compressed to the surface pressure above the equilibrium value of the pure peptide adsorption to the pure air/water interface before addition of the peptide, the peptide adsorption led to a slight increase of the surface pressure. They demonstrate that the peptide is not able to insert into zwitterionic monolayers at surface pressures above 25 mN/m and it inserted into both negatively and positively charged monolayers up to 30 mN/m. Apparently, the peptide interacts with charged monolayers that leads to its insertion even at high surface pressures.

6.2.3. Structure of lipid monolayers with adsorbed Aβ (1-40) peptide (GIXD).

The structure of negatively charged DPPG and DPPS, zwitterionic DMPE, DPPE and DPPC monolayers as well as positively charged DSTAP was investigated by GIXD experiments. The monolayers were compressed to a desired pressure, which was kept constant by an automatic mode of the trough, and diffraction data were taken. At low surface pressure, three diffraction peaks can be detected for DPPG, DMPE and DPPE monolayers. Such a peak distribution indicates the existence of an oblique chain lattice with molecules tilted in an intermediate direction between NN and NNN. The diffraction pattern of DPPC and DSTAP on both water and buffer and DPPG on buffer consist of two Bragg peaks: one at $Q_z = 0$ Å^{-1} and second at non-zero Qz. In the case of DPPC and DPPG it is not clear whether the second peak consists of one broad peak or of two non-resolved peaks. In the first case the lattice formed by aliphatic chains is orthorhombic with chains tilted into NN direction and in the second case it is oblique with chains tilted into intermediate direction between NN and NNN, similar to that of DPPG, DMPE and DPPE on water. Despite of this the fitting with two or three Bragg peaks results in similar values

of the tilt angle and cross-sectional area of the chain. Peak positions (Q_{xy} and Q_z values), the lattice parameters and tilt angles t for all measured phospholipids on water and on buffer are presented in Tables A3.3, A3.4, A3.9, A3.14-16 (Appendix 3). Increasing pressure leads to a shift to larger Q_{xy} and smaller Q_z values, because increasing lateral pressure decreases the tilt angle of the aliphatic chains. The phase transition to hexagonal packing of upright oriented molecules for DMPE, DPPE and DPPG on water takes place between 30 mN/m and 40 mN/m.

As it was shown before (Chapter 4), the peak positions for DPPG monolayers on buffer differ from those obtained on water. The positions are shifted to lower Q_{xy} and higher Q_z values indicating larger unit cell area and larger tilt angle of the aliphatic chains. Transition to the hexagonal packing cannot be achieved even at very high surface pressure. The tilt angle of DPPG chains on buffer decreases continuously with increasing pressures. DPPC and DSTAP on water and buffer exhibit a behaviour similar to DPPG on buffer. The mismatch between the head group size and the size of the two aliphatic chains leads to the tilted structure observed at all pressures. For DPPC, the lattice parameters and the tilt angle of the chains are the same at different ion concentrations and in a large pH interval, since DPPC is a zwitterionic lipid [120] with a large head group. However, the low resolution of diffraction peaks (due to a small correlation length) does not allow a very precise determination of the molecular tilt. In this case, the error bar can be ~ 2 º. In the case of DSTAP the size and strong repulsion between neighbouring molecules do not allow tighter packing in the monolayer (Tables A3.17-19 in Appendix 3). The structure of DSTAP monolayers, however, differs on water and on buffer. The lipid has a larger tilt on buffer, than on water. Since the lipid is equally charged in both cases, this indicates that counterions (Cl^-) penetrate into the DSTAP headgroup region and increase the area occupied by a lipid molecule.

GIXD measurements were also performed for lipid monolayers with adsorbed Aβ. Adsorption occured at initially zero pressure of the lipid monolayer. Data were collected after the surface pressure was stabilized, therefore the starting pressure is above 15 mN/m. When the equilibrium surface pressure was reached, the lipid/peptide film was compressed to obtain data for higher surface pressures. The obtained results and calculated structural parameters are shown in Tables A3.20-27. Comparison of the Bragg peak positions shows that the chain lattices of DPPC, DMPE and DPPE on Aβ solution in water as well as DPPC, DPPG and DSTAP on Aβ in buffer are very similar to that of lipid monolayers on pure subphase at the same surface pressures (Figures 6.10, 6.11). It is interesting to note that DPPC and DPPG being liquid at the beginning of the peptide adsorption condense and form the same structure as in the absence of the peptide

with increasing the surface pressure.

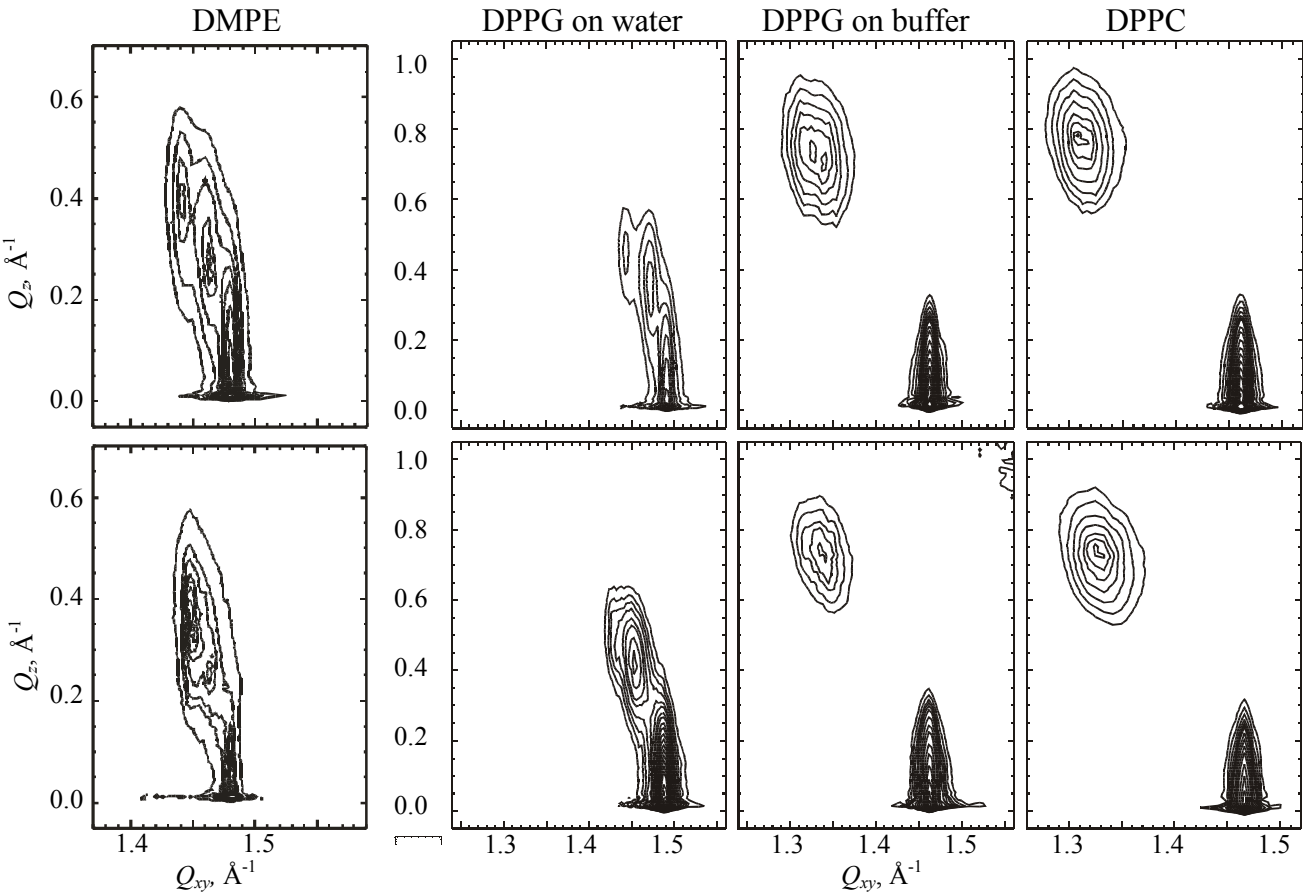

Figure 6.10. *Contour plots of the corrected X-ray intensities as a function of the in-plane component Q_{xy} and the out-of-plane component Q_z of the scattering vector of:DMPE on water, DPPG on water and buffer with pH 7.4, DPPC on buffer at 20 mN/m (top from left to right); the same lipid on 0.3 μM Aβ in water and buffer with pH 7.4, respectively (bottom).*

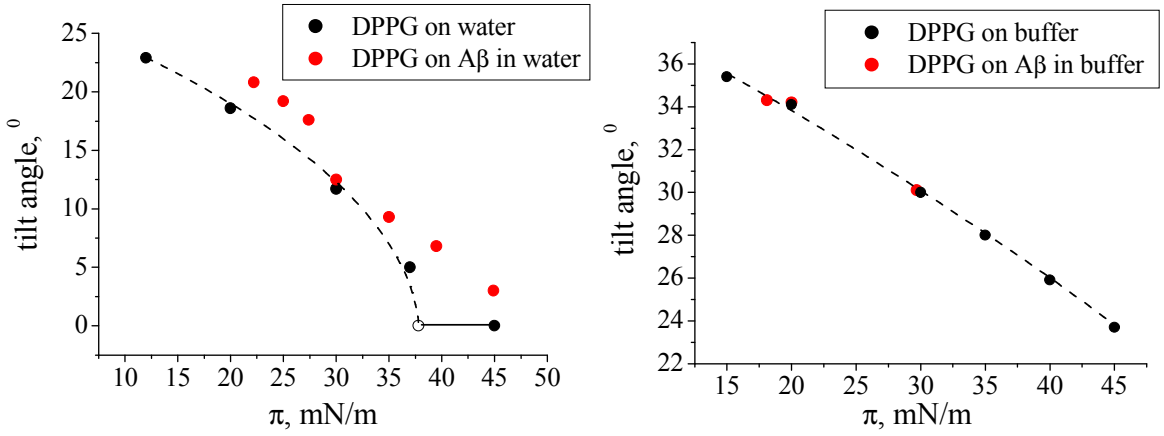

Figure 6.11. *Tilt angle of DPPG aliphatic chains on water and on Aβ solution in water – left and on buffer with pH 7.4 and on Aβ solution in the same buffer – right as a function of the surface pressure*

DPPG chains on Aβ in water have slightly larger tilt that can be explained by electrostatic interactions between the lipid and the peptide, which lead to a slightly higher ionization state of the lipid. Higher ionisation state may lead to larger repulsion between neighbouring molecules and slight reorientation of the headgroup, which increase the area per DPPG molecule. Aliphatic chains follow this change by increasing their tilt.

In contrast to DPPG, the DSTAP ionisation state is not changing upon binding with ions or the peptide. However the counterions can penetrate into the headgroup region of the lipid and lead to the different area occupied by the DSTAP molecule and tilt angle of the DSTAP chains on water and on 1 mM and phosphate buffered saline with pH 7.4 (Figure 6.12).

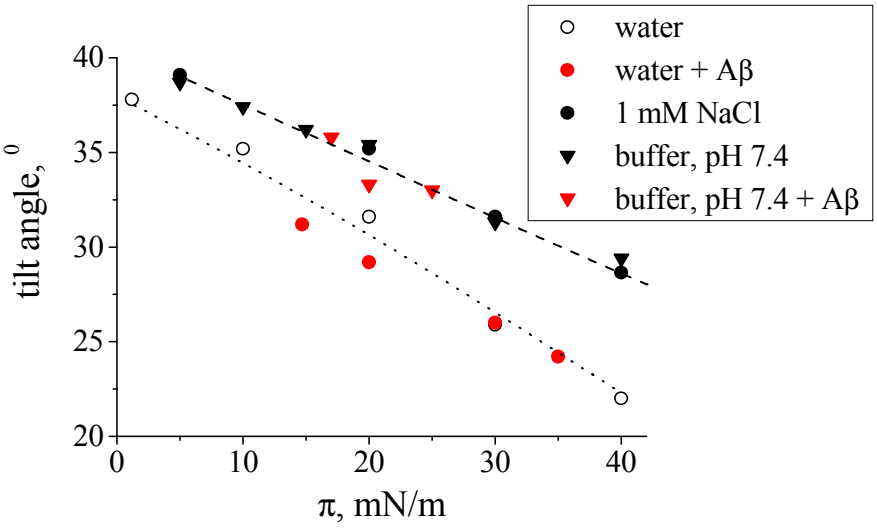

Figure 6. 12. *Tilt angle of DSTAP aliphatic chains on various subphases in the presence and absence of Aβ as a function of the surface pressure*

The DSTAP structure on water in the presence of the peptide is highly disturbed, the Bragg peaks are very broad and weak (Figure 6.13) and therefore the lipid structure estimation is not precise. Despite of this, the peak positions of DSTAP are similar on Aβ in water and pure water. The structure of DSTAP in the presence of buffer of NaCl is not destroyed by the peptide adsorption and the structure is the same on buffer and on Aβ in buffer. The small shift the of Bragg peak positions for DSTAP on Aβ is due to the small difference in pressure (15 mN/m in the case of buffer and 17 mN/m for buffer with Aβ)

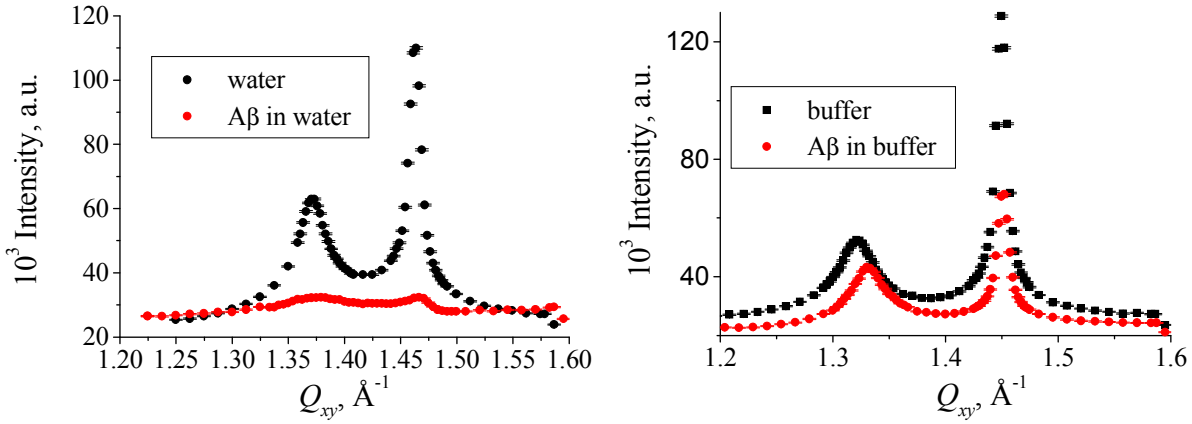

Figure 6.13. *Integrated intensity over the Q_z range –0.05 to 1.05 Å^{-1} as a function of Q_{xy} for DSTAP monolayer on water and on Aβ in water – left and to the DSTAP monolayer on buffer with pH 7.4 at 15 mN/m and on Aβ in the same buffer at 17 mN/m – right*

The GIXD patterns of the Aβ peptide adsorbed to the air/water interface or to lipid monolayers at low surface pressure show a Bragg peak at Q_{xy} = 1.33 Å^{-1} (ΔQ_{xy}=0.065 Å^{-1}) and zero Q_z with low intensity (Figure. 6.14).

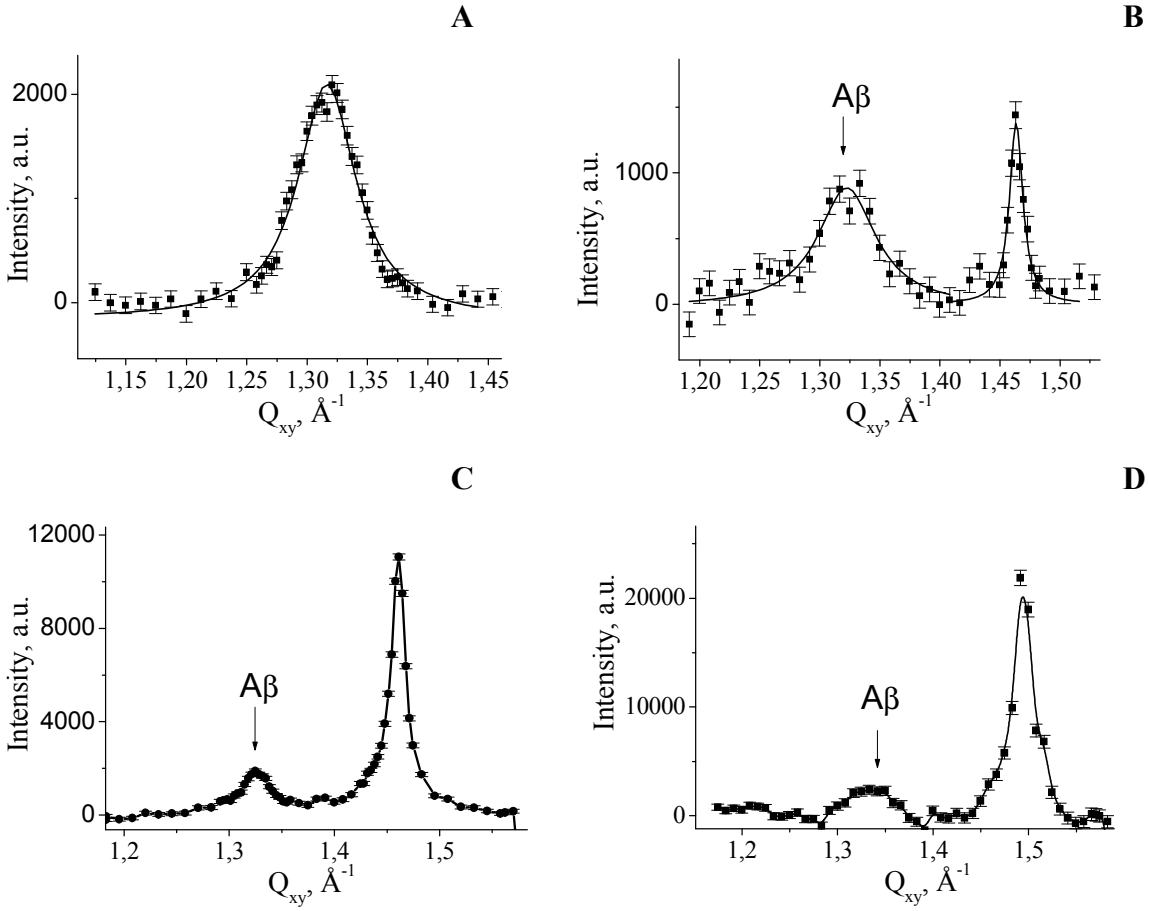

Figure 6.14. *Integrated intensity over the Q_z range –0.05 to 0.3 Å^{-1} as a function of Q_{xy} for Aβ adsorbed at the air/water interface – A (14 mN/m), adsorbed to the DPPC monolayer on water - B (10 mN/m), to the DPPG monolayer on buffer – C (18 mN/m) and water - D (20 mN/m). The peak between 1.45 and 1.5 Å^{-1} corresponds to the lipid monolayer.*

The peak corresponds to a distance of 4.7 Å, which is the spacing between hydrogen-bonded peptide chains in a β-sheet structure. In some cases an additional Bragg peak with a d-spacing of 39.3 Å was found (Figure 6.15 A). The origin of this peak is still unclear. It can for example arise from the width of the β-sheet ribbon that can be a length of one β-strand (~ 10 amino acids). The weak peak at 1.33 $Å^{-1}$ and an additional peak at small angles was not observed in the diffraction patterns taken at surface pressures above 30 mN/m for most of experiments.

Only in the case of DSTAP on Aβ in water both peaks can be observed at higher surface pressures, the intensity decreases but it does not disappear completely. This sample was measured with the set-up including thinner capton window, therefore it was possible to measure the diffraction signal at lower angles. At 40 mN/m, an additional peak at Q_{xy} = 0.08 $Å^{-1}$ and at zero Q_z can be seen, that corresponds to a distance of 80 Å (Figure 6.15 B). Interestingly, the position of this peak is half of the position of the weak peak at non-zero Q_z. It is possible that the latter is a second order peak of the distance of 80 Å. It is unlikely that the peptide forms mature fibrils within only 2-3 hours [112], thus this distance should arise from oligomers or protofibrils that come closer to each other during compression and exhibit one-dimensional ordering. Goldsbury et al [112] have shown that the protofibrils have usually ~ 8 nm in diameter, which is consistent with the distance measured in the present work. At present it is not clear whether the observed Bragg peak arises from the distance between neighbouring protofibrils or not.

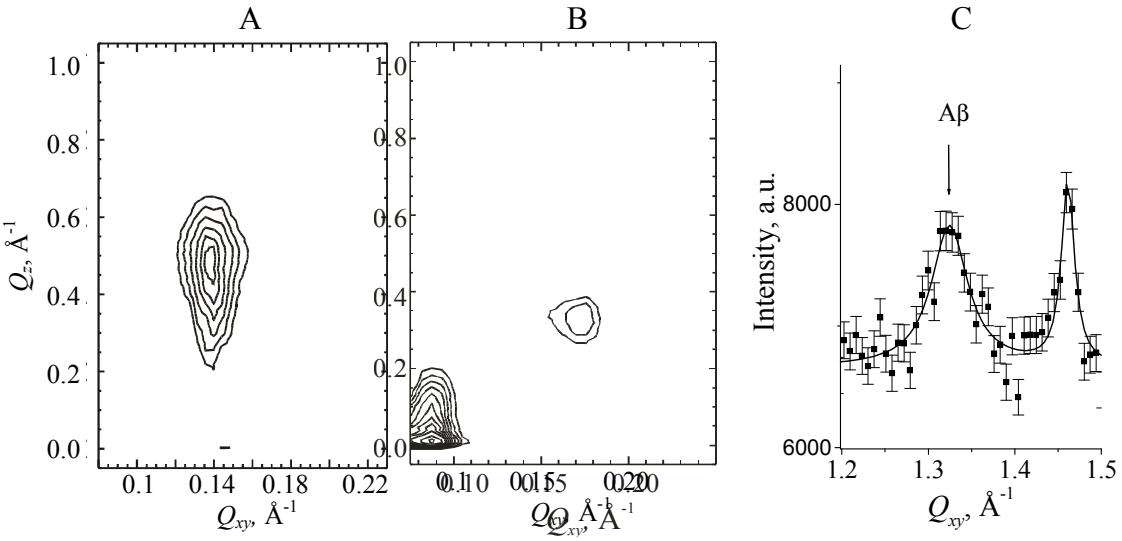

Figure 6.15. *Contour plots of the corrected X-ray intensities as a function of the in-plane component Q_{xy} and the out-of-plane component Q_z of the scattering vector of Aβ adsorbed to the air/water interface (A) and on a DSTAP monolayer at the surface pressure of 40 mN/m (B) and integrated intensity over the Q_z range –0.05 to 0.3 $Å^{-1}$ as a function of Q_{xy} for Aβ adsorbed on a DSTAP monolayer at 18 mN/m – C*

6.2.4. IRRAS of Aβ adsorbed at the air/water interface and on lipid monolayers.

IRRAS was applied to detect the Aβ presence and its secondary structure at the interface. During Aβ adsorption to the air/water interface or insertion into phospholipid monolayers, amide bands in the region between 1700 – 1500 cm^{-1} (Amide I: 1700-1620 cm^{-1} and Amide II: 1580-1520 cm^{-1}) appear and grow (Figure 6.16). After 3-4 hours of adsorption no further increase of the amide band intensities was observed.

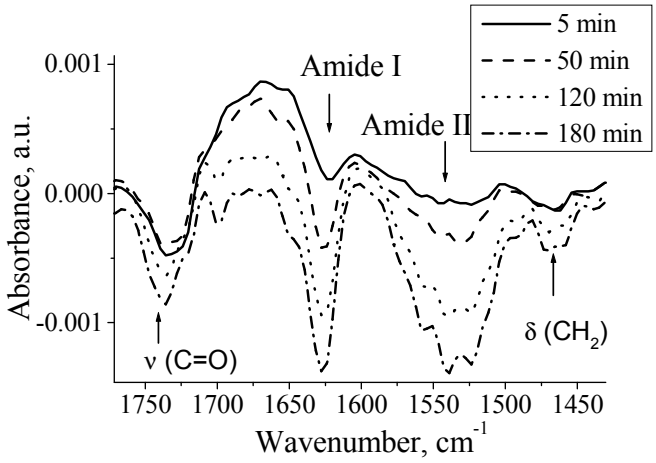

***Figure 6.16**. IRRA spectra of Aβ adsorbed to a DPPC monolayer (π_0 = 0 mN/m, A_0 = 96 $Å^2$/molecule) on water taken at different times. The peptide concentration was 0.185 μM; the final surface pressure was 15 mN/m. All spectra have been recorded at an angle of incidence of 40° and with s-polarized light.*

In order to compare spectra of Aβ adsorbed at the air/water (buffer) interface and on lipid monolayers, the pure lipid spectra were subtracted from mixed lipid/peptide spectra. The remaining peptide spectra are very similar to the spectra of the pure peptide adsorbed at the air/water (buffer) interface (Figure 6.17). The position of the amide bands does not depend on the type of lipid (zwitterionic or negatively charged). The most intense band in the Amide I region was obtained at 1627 cm^{-1} with a shoulder at 1690 cm^{-1} indicating the β-sheet conformation of the peptide at the interface. The shoulder of the Amide I band in the region of 1648 - 1658 cm^{-1} reveals the presence of a small amount of random coil or α-helical conformation, and the shoulder at 1674 cm^{-1} may be attributed to a β-turn or to residual trifluoroacetic acid (TFA) [121]. Amide II bands can be also used for secondary structure determination, however they are rarely used for this purpose [38]. Two major contributions were found in the Amide II region of the Aβ spectra. The most intense contribution at around 1530 cm^{-1} indicates the presence of β-sheet structure while a band at around 1550 cm^{-1} can be attributed to random coil, α-helix or β-

turn conformation [38, 58, 84]. Thus, Aβ peptide at the interface has mainly β-sheet conformation. Although the peptide has predominantly random coil conformation in water and buffer at pH 7.5, as proved by CD spectroscopy, the IRRA spectra do not change during the adsorption process. The peptide spectra are similar to those obtained for aggregated Aβ. Either only the small part of the peptide existing already in β-sheet conformation in bulk adsorbs to the interface, or the conformational transition from mainly random coil to mainly β-sheet at the interface is too fast to be detected.

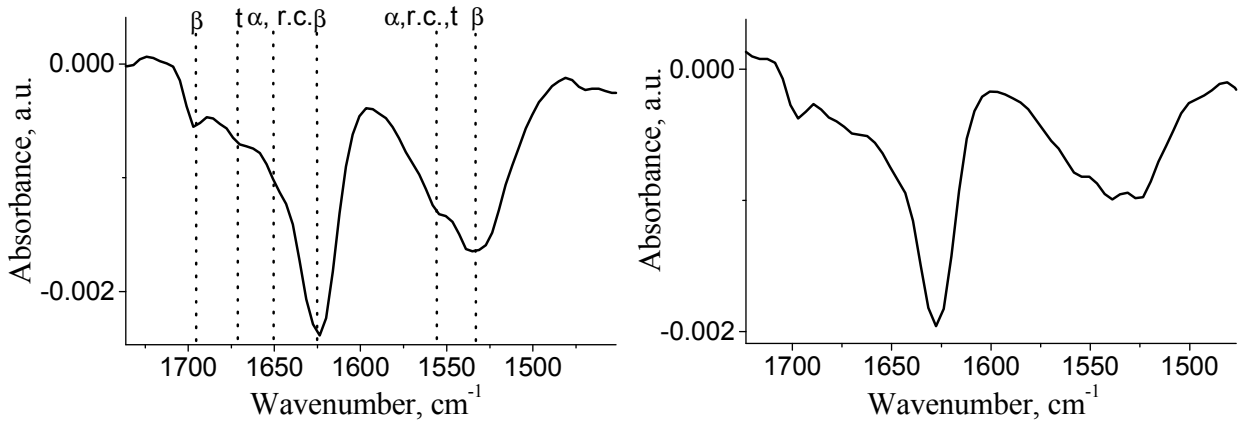

Figure 6.17. *IRRA spectra of Aβ adsorbed to the pure air/buffer interface (π = 14 mN/m) (left) and to a DPPG monolayer at 16 mN/m (right). The adsorption process started at an initial area per lipid of 96 Å^2. The respective spectrum of a pure DPPG monolayer recorded at the same area per molecule was subtracted.. All spectra have been recorded at an angle of incidence of 40° and with s-polarized light.*

IRRAS was also employed to reveal the orientation of molecules at the interface. For this purpose, spectra were acquired with p-polarized light at various angles of incidence (Figure 6.18 left). P-polarized light probes the dipole moment components parallel and perpendicular to the surface, and therefore molecular orientations can be determined. In contrast, s-polarized light probes only the dipole moment component parallel to the surface. The respective negative reflectance-absorbance values increase monotonically with increasing incidence angle and do not allow obtaining detailed information about the anisotropy of the film.

The Amide I band (1627 cm^{-1} and 1690 cm^{-1}) is associated with the peptide C=O stretching vibration and splits into two components. The transition dipole moment of the more intense contribution at 1627 cm^{-1} is oriented along the inter chain hydrogen bonds perpendicular to the peptide chain, and the less intense contribution at 1690 cm^{-1} is oriented along the peptide chain. The Amide II band results from C-N stretching and N-H bending vibrations. Its transition dipole moment is oriented along the peptide chain. The presence of a layer (e.g. lipid monolayer,

adsorbed peptide) at the air/water interface leads to the appearance of the O-H stretching band at 3800-3000 cm^{-1} and the H_2O bending band in the region of amide bands (1700-1600 cm^{-1}) that produces additional difficulties in the determination of the peptide secondary structure. The intensity of these bands depends on the layer thickness and refractive index [118, 122]. Simulations of amide bands of a β-sheet oriented parallel to the interface are shown for different angles of incidence using p-polarized light in Figure 6.18. A film thickness of 10 Å and the respective extinction coefficients of a model antiparallel β-sheet were used for the calculation [42]. Comparison of measured and simulated spectra reveals that Aβ is lying flat at the air/water interface. The orientation of the peptide penetrating into a phospholipid monolayer is the same as at the pure air/water interface (spectra not shown). This indicates that the presence of an uncompressed phospholipid monolayer does not affect the secondary structure as well as the orientation of the peptide.

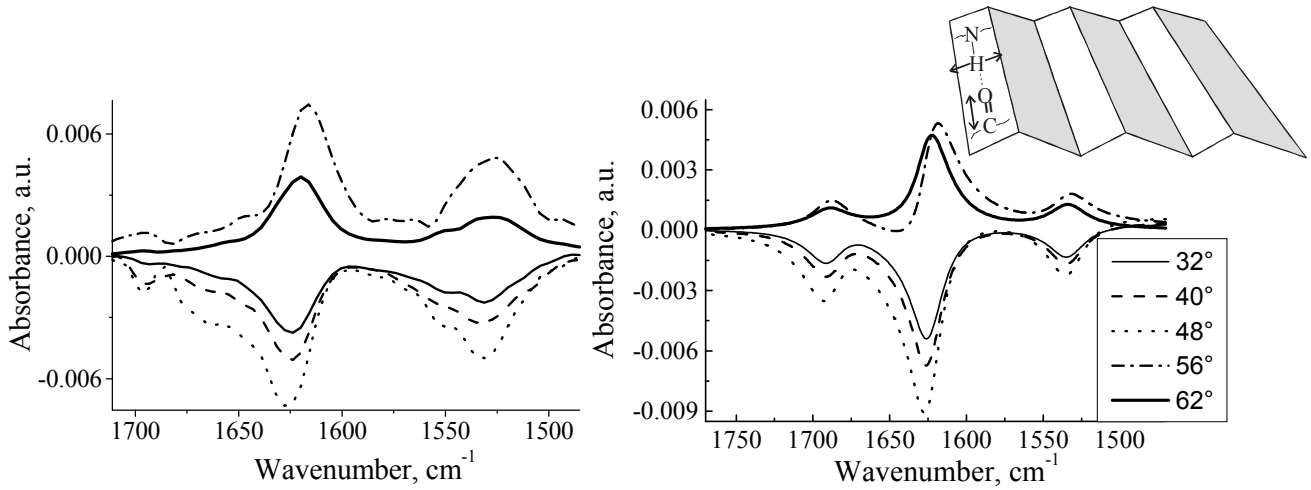

Figure 6.18. *Left -IRRA spectra of Aβ (0.185 μM) adsorbed at the air/buffer interface acquired with p-polarized light at various angles of incidence. The surface pressure induced by peptide adsorption is 15 mN/m. Right - simulated IRRA spectra of a β-sheet secondary structure lying flat at the air/water interface. The calculation was performed for p-polarized light and the respective angles of incidence for the Amide I bands at 1627 and 1690 cm^{-1} and the Amide II band at 1535 cm^{-1}.*

In contrast to Aβ insertion into phospholipid monolayers, a non β-sheet structure was detected during the first 30 min of Aβ insertion into positively charged DSTAP and DPTAP monolayers (Figure 6.19). The Amide bands have completely different shape and positions. The low intensity does not allow precise determination of the peptide orientation and it is not even possible to distinguish between random coil and α-helical structures. After ~ 30 minutes, the band at ~ 1626 cm^{-1} appears and grows. The final Aβ/DSTAP (or DPTAP) spectrum reminds

ofAβ/phospholipid spectra. Obviously, the peptide adopts first ether random coil or α-helical conformation at the interface that transforms into β-sheet conformation when a critical surface concentration of the peptide is achieved. It is well known that this critical concentration is higher for basic conditions than for neutral and acidic pH. The surface pH in the vicinity of the positively charged monolayers is higher than the bulk pH. This difference can be large (3-5 pH units) for highly charged trimethyl-ammonium-propane monolayers. Thus on water as well as on buffer, the surface pH can be close to 10. Therefore, to observe the aggregation (β-sheet formation) much more peptides at the interface covered with positively charged lipid monolayers are needed compared to common phospholipid monolayers.

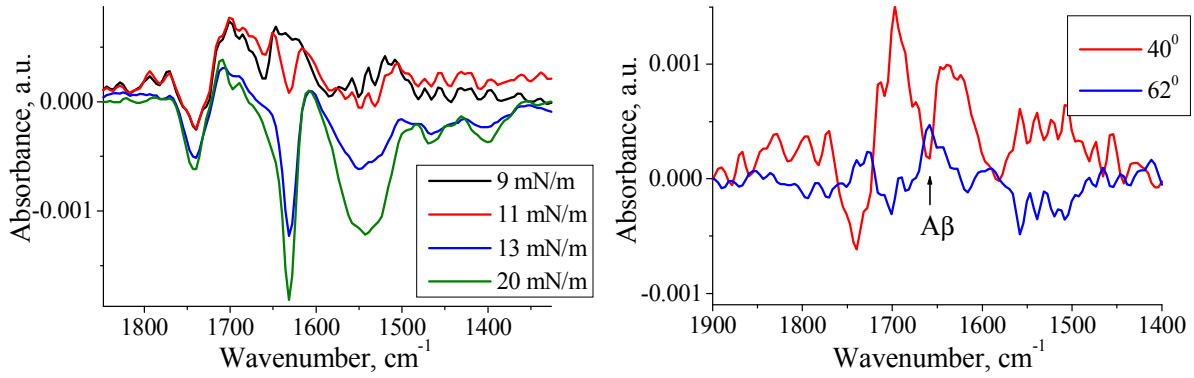

Figure 6.19. *IRRA spectra of DPTAP monolayers on Aβ solution in water taken during peptide adsorption. The surface pressure increases due to the peptide insertion into the monolayer. Left - spectra acquired with s-polarized light and incidence angle of 40 ° and right - spectra acquired with p-polarized light below and above the Brewster angle after ~ 20-30 minutes of adsorption at 9-10 mN/m.*

Additionally, IRRAS provides information about the state of lipid aliphatic chains in a monolayer [40]. The symmetrical (2849-2855 cm^{-1}) and asymmetrical (2916-2925 cm^{-1}) stretching modes of CH_2 groups are sensitive to conformational order and packing of the hydrocarbon chains [44, 45]. In the liquid-expanded state, the appearance of gauche conformations shifts the CH_2 modes to approximately 2924 cm^{-1} and 2855 cm^{-1}. In the liquid-condensed state, these bands are located at smaller values (approximately 2919 cm^{-1} and 2850 cm^{-1}), indicating that the aliphatic chains are in all-trans conformation.

Figure 6.20 (left) shows the CH_2 stretching mode positions as a function of surface pressure for DMPE monolayers on water during compression and DMPE monolayers on 0.185 μM Aβ in water during peptide adsorption. It is revealed that the phase behavior of zwitterionic DMPE is not influenced by Aβ adsorption. The same is also observed for zwitterionic DPPC on water as well as on buffer. The peptide penetrates into the area not occupied by lipids and

compresses them. This induces the phase transition in DPPC and DMPE monolayers. Since the transition pressure is the same on water and on the peptide solution, one can conclude that the peptide does not specifically interact with the zwitterionic lipids.

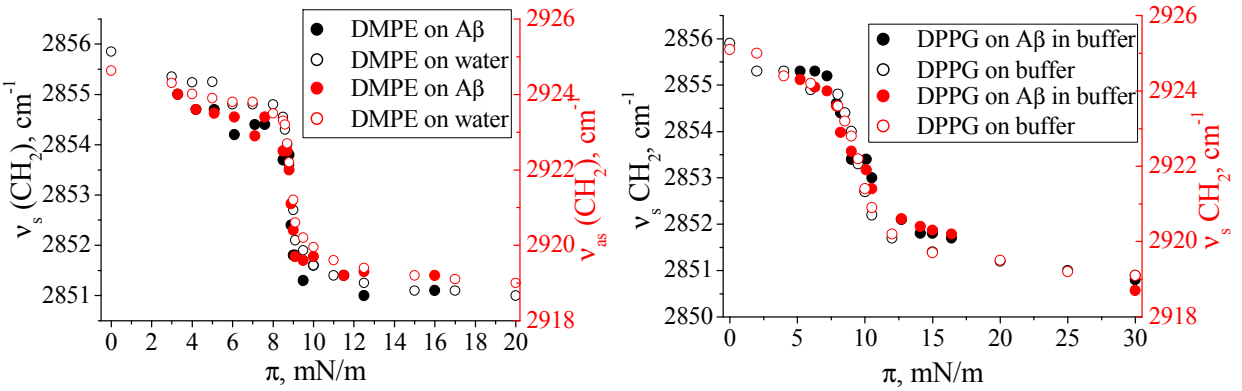

Figure 6.20. *Positions of the CH_2 symmetrical and asymmetrical stretching modes for DMPE monolayer on water (left) and DPPG monolayer on buffer with pH 7.4 (right) during compression and during Aβ adsorption.*

Similar results were obtained for DPPG on buffer with pH 7.4 (Figure 6.22 right). Therefore, it is unlikely that the peptide specifically interacts with these phospholipids at physiological pH values. The packing of the lipids in the condensed state is not influenced by the peptide as well. However, a shift in the CH_2 stretching modes of charged lipids on water indicates a small perturbation of the chain ordering (Figure 6.21). Obviously, in the absence of inorganic counter ions electrostatic interactions between lipids and the peptide play a significant role that leads to a better distribution of the peptide in the monolayer and therefore to a partial liquidization of the lipids.

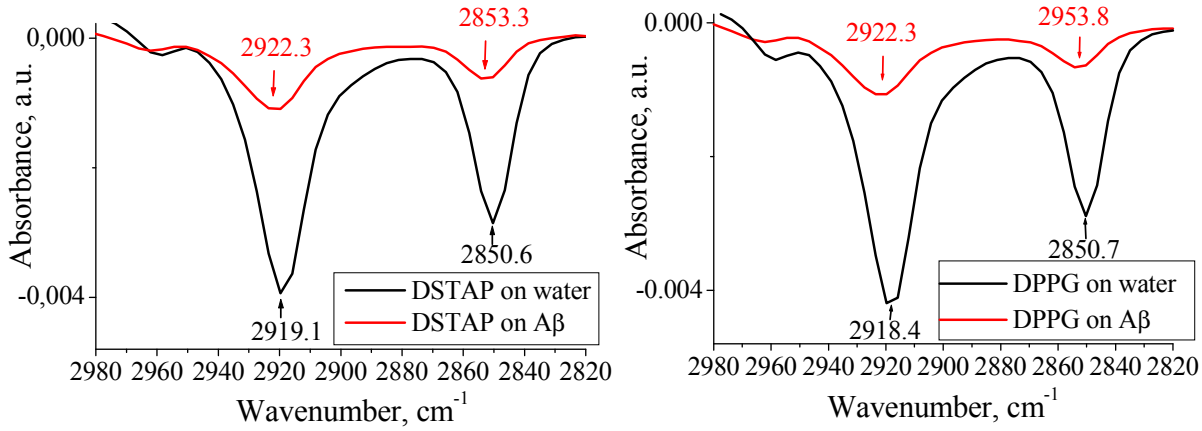

Figure 6.21. *IRRA spectra in the region of CH_2 stretching modes of DPPG (left) and DSTAP (right) monolayer on water and on Aβ solution in water at 20 mN/m (right). The adsorption process started at an initial area per lipid of ~ 100 Å^2. Spectra have been recorded at an angle of incidence of 40° and with s-polarized light.*

Compression of lipid monolayers with inserted Aβ leads to the squeezing out of the peptide at lateral pressures above 30 mN/m. At high surface pressures (40-45 mN/m), the monolayer occupies the same area per lipid molecule as the pure lipid monolayer on water or buffer. Expansion leads to a re-insertion of the peptide into the monolayer at surface pressures below the equilibrium value of 16-18 mN/m. IRRAS measurements show that the amide bands disappear completely from the IRRA spectra of zwitterionic monolayers on water and buffer and of anionic monolayers on buffer at surface pressures above 30 mN/m. This indicates that the peptide might be even desorbed from these monolayers. Another situation was observed for anionic monolayers on water. The Amide I band intensity decreases and shifts to slightly larger wavenumbers (from 1627 to 1630 cm^{-1}), but the bands do not disappear completely.

To prove the specific adsorption of the peptide to charged monolayers, another procedure was applied. The monolayers were compressed to a high surface pressure (30 mN/m) before peptide injection. After injection, the peptide does not adsorb to zwitterionic monolayers on both water and buffer. In this case, the monolayer spectra are identical to pure phospholipid spectra, no amide bands appear even after 24 hours of adsorption. In the case of negatively as well as positively charged monolayers on water, Aβ injection leads to the appearance of amide bands and the intensity of the water bands increases (Figure 6.22). The latter indicates an increasing surface layer thickness due to Aβ adsorption.

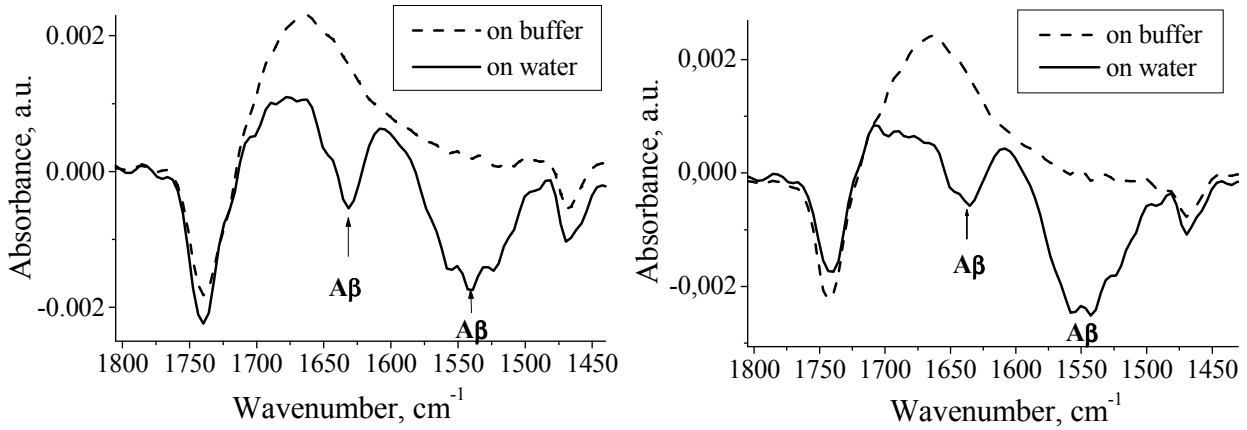

Figure 6.22. *IRRA spectra of DPPG (left) and DSTAP (right) monolayers on buffer (solid line) and on water (dashed line) with injected 40 μg Aβ. Spectra were taken one day after Aβ injection. The surface pressure was kept constant at 30 mN/m. All spectra have been recorded at an angle of incidence of 40° and with s-polarized light*

The most intense band in the Amide I region is observed at 1630 cm^{-1}. This position can again be attributed to β-sheet conformation. The reason for the shift of the Amide I band to larger wavenumbers could be a reduction of crystallinity of the adsorbed β-sheet induced by a more

hydrophilic environment in the vicinity of the phospholipid head groups. This assumption is supported by the disappearance of the Bragg peak arising from β-sheet structure in GIXD experiments.

On buffer, no peptide adsorption to charged monolayers was observed. Furthermore, injection of NaCl into the subphase beneath a DPPG monolayer compressed to 30 mN/m with adsorbed Aβ leads to the disappearance of the peptide signal (Figure 6.23). This can be explained by competitive adsorption of counterions. It is interesting to note that the presence of adsorbed peptide increases the intensity of the phosphate band around 1223 cm^{-1} indicating a slightly higher degree of ionization of DPPG on the peptide subphase compared to pure water. The phosphate group of DPPG should be slightly dehydrated in the presence of the peptide compared to the DPPG monolayer on buffer.

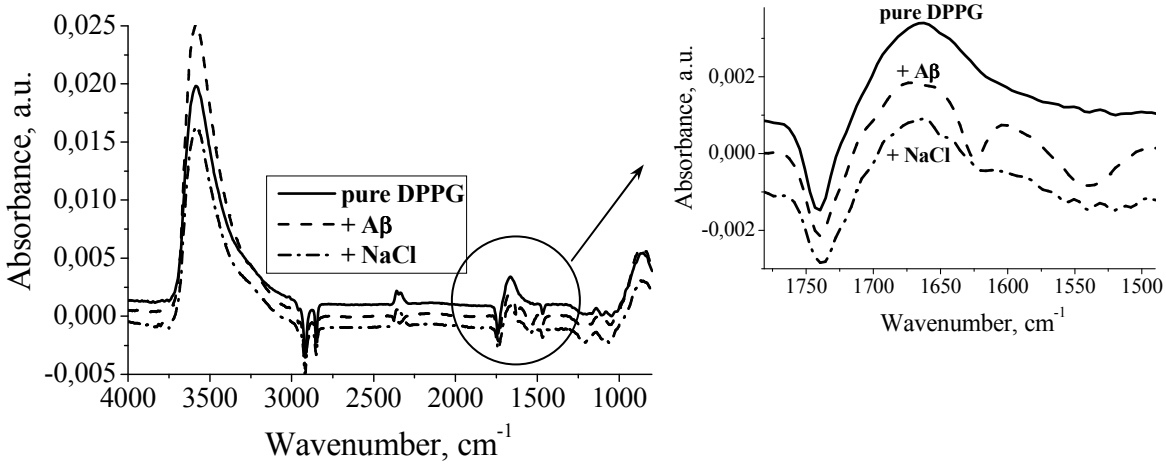

Figure 6.23. *IRRA spectra of a DPPG monolayer (amide region) on water (solid line), 3 hours after injection of 40 μg Aβ (dashed line) and one day after addition of salt (dotted line). The final Aβ concentration is 0.92 μM, and the final salt concentration is 50 mM. The DPPG spectra were shifted to 0.001 and DPPG on Aβ + salt to – 0.001 for clarity. The surface pressure was kept constant at 30 mN/m. The spectra were acquired with s-polarized light and an angle of incidence of 40°.*

Aβ adsorbs to compressed DPPS, POPG and GM1 monolayers on water at 30 mN/m although no adsorption of the peptide on these monolayers in the presence of buffer occurs (Figure 6.24). The adsorption is unspecific and can be ascribed to enhanced electrostatic interactions at low ionic strength. The surface charge density is obviously playing a little role as well as the nature of the anionic headgroup. For example, the GM1 has no phosphate group but it has a sugar group with carboxylic acid instead. The lipid phase state is not important as well, because the peptide adopts the same structure being adsorbed at a POPG monolayer, which is in the liquid expanded state, and at a DPPG monolayer, which is in a condensed state at room

temperature and 30 mN/m. Moreover, penetration or adsorption at zwitterionic DMPC on both water and buffer as well as at anionic POPG and DMPG on buffer, which exhibit also the LE phase under experimental conditions, does not occur at a surface pressure of 30 mN/m.

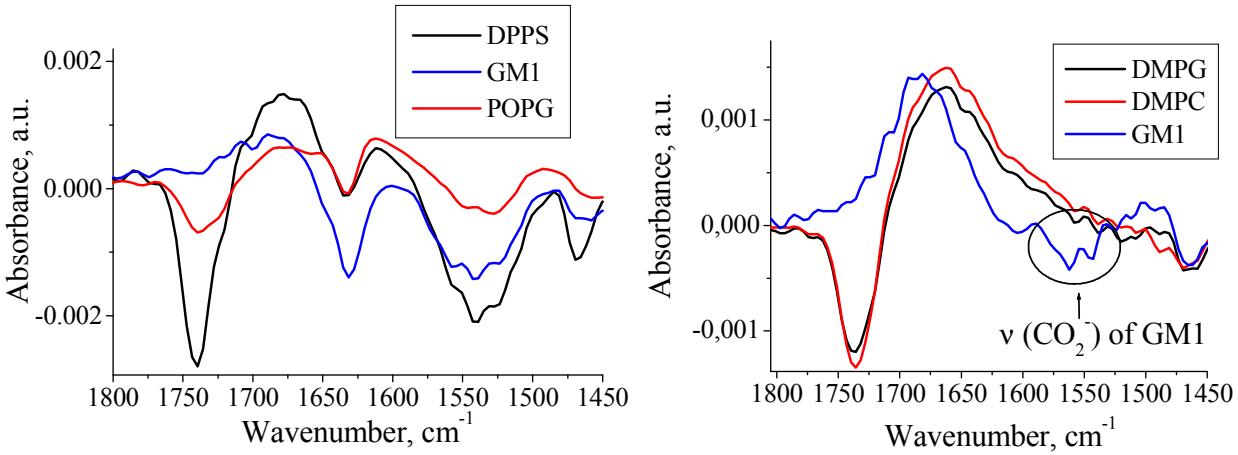

Figure 6.24. *IRRA spectra of different monolayers (amide region) on water (left) and on buffer (right). The spectra were taken ~ 12 hours after injection of 40 μg Aβ. POPG, DMPG and DMPC exhibit LE phase under the experimental conditions. The surface pressure was kept constant at 30 mN/m. The spectra were acquired with s-polarized light and an angle of incidence of 40°.*

However, a difference in the behavior of Aβ adsorbed at DPPG and DMPG at high surface pressure was observed. When the peptide inserted into DPPG monolayer on buffer the compression leads to a complete squeeze out of the peptide at higher surface pressures. In contrast, Aβ remains in the monolayer when DMPG is compressed to 30 mN/m. The difference between these two lipids is the phase state: DPPG exhibits a condensed phase at 30 mN/m and room temperature, while DMPG is in the liquid-expanded state under these conditions. The transition from LC to LE phase in the DMPG monolayer occurs at the surface pressure above 30 mN/m (37-41 mN/m). The peptide is squeezed out only when the condensed phase is formed (Figure 6.25). The peptide also remains adsorbed on or penetrated into the DMPG monolayer at 30 mN/m after salt is added to the subphase containing pure water. The peptide must be stabilized in the monolayer when DMPG is in the LE phase via electrostatic interactions, because it leaves the zwitterionc DMPC monolayer at high surface pressure, which exhibits the liquid-expanded phase as well under these conditions.

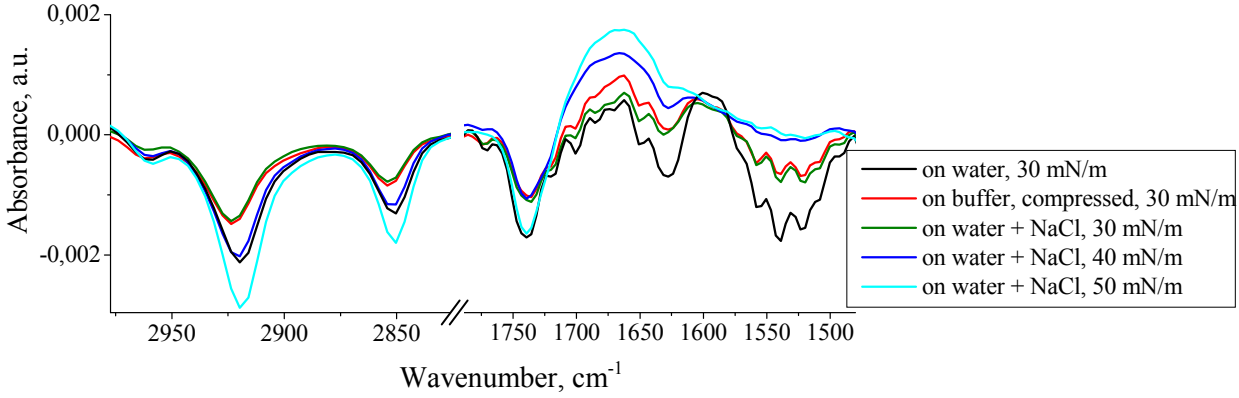

Figure 6.25. *IRRA spectra of DMPG monolayers in the CH_2 stretching and the amide regions in the presence of 40 μg Aβ. DMPG monolayer on water at 30 mN/m exhibits a condensed phase while on buffer it is in the LE phase. The phase transition of DMPG monolayer on buffer from LE to LC phase occurs at 37-41 mN/m under the experimental conditions. The spectra were acquired with s-polarized light and at an angle of incidence of 40º.*

Obviously, the hydrophobic interactions between aliphatic chains in the condensed phase are too strong. The peptide insertion into the monolayer is unfavorable since it would destabilize the interchain interactions. Therefore, the peptide is squeezed out from a condensed monolayer at high surface pressure. Another situation is observed when the lipid is in the liquid-expanded phase, the interchain interactions are weak and the peptide presence does not disturb the monolayer to a larger extent. Moreover, the peptide is stabilized in the anionic monolayers at high surface pressure due to weak electrostatic interactions.

6.3. Discussions

The secondary structure of Aβ adsorbed at the pure air/water (buffer) interface or at phospholipid monolayers has been determined by IRRAS experiments. The data demonstrate clearly that the peptide at the interface adopts a β-sheet conformation oriented parallel to the interface. The result is supported by GIXD investigations. The last reveal a Bragg peak arising from the adsorbed peptide β-sheets with a characteristic repeat distance of 4.7 Å. The air/water interface as well as phospholipid monolayers in an uncompressed state can be considered as hydrophobic / hydrophilic interfaces. Therefore, we assume that Aβ is attracted by such hydrophobic interfaces and increasing surface concentration of Aβ is responsible for the observed conformational change in the secondary structure from random coil to β-sheet. A similar result was previously observed by T. Kowalewski and D. M. Holtzman [123]. They found that Aβ forms uniform elongated sheets on hydrophobic graphite. The dimensions of these sheets were consistent with those of β-sheets with extended peptide chains perpendicular to the long axis of the aggregate.

The presence of the peptide in the monolayer does not change the phase behavior of zwitterionic lipids. The peptide is stabilized at the interface, because it allows withdrawing of hydrophobic amino acid residues away from water. However, it is unlikely that these residues are interacting with lipid aliphatic chains. Such interactions would change the phase transition of the lipid from LE to LC, which was not observed. This behavior of Aβ resembles adsorption of B18 on zwitterionic monolayers. Obviously, in both cases no interactions between lipid chains and peptide occur.

Compression of lipid monolayers with adsorbed Aβ leads to the peptide squeeze out. The peptide leaves the zwitterionic monolayers completely. Aβ can also not penetrate into the zwitterionic lipid monolayers when they are compressed to high surface pressure before peptide injection. The monolayer formed by zwitterionic phospholipids at high surface pressure can be considered as a hydrophilic surface. Obviously, there is no driving force for the peptide to adsorb from aqueous polar environment to the polar lipid headgroup. However, adsorption of Aβ to highly compressed charged TAP, PG, GM1 and PS monolayers on water can be explained by weak electrostatic interactions between these lipids and Aβ. These interactions are possible owing to a low counter ion concentration in the subphase and therefore a poor charge compensation of charged monolayers combined with a low surface pH [12] inducing a net

positive charge in the peptide in the case of anionic lipids and, in turn, high surface pH and net negative charge of the peptide in the vicinity of positively charged monolayers. Since the area occupied by a lipid molecule at high surface pressure increases very little during adsorption of the peptide, one can conclude that the peptide is adsorbing at the monolayer but not penetrating into the chain region. Being adsorbed at negatively charged monolayers, the peptide should change the ionisation state of lipid molecules acting as buffer. As we know, the structure of a charged DPPG monolayer differs from that of the protonated one. Therefore, one can expect that the structure of DPPG monolayers on water and on the peptide solution will differ as well, although in reality the DPPG structure is almost not changed after Aβ adsorption. Probably there are two phenomena, which compensate each other. On one hand the peptide changes the lipid ionization state increasing the repulsion between lipid molecules that leads to a more tilted structure, and on the other hand interaction with lipid molecules may affect the headgroup orientation and hydration which can change the tilt angle in the opposite direction.

The electrostatic interactions with charged lipids lead to peptide adsorption (high surface concentration of peptide) and as consequence to aggregation. The secondary structure of the peptide adsorbed at charged monolayers is slightly different from that formed at the air/water interface most likely due to such factors as hydration and electrostatic interactions. The shoulder at 1650 cm^{-1} in the amide I region of the peptide/lipid spectra suggests that this structure, beside β-sheet, contains additionally either α-helix or random coil. Kowalewski and Holzemann observed the formation of aggregates, which develop into fibrils on hydrophilic negatively charged mica surfaces. The dimensions of these aggregates were different from the layer formed on a hydrophobic graphite surface. Probably, the peptide being attracted to a charged surface forms partly α-helical partly β-sheet structures. Transition from random coil to α-helix was previously detected [91] during aggregation and fibrillization of Aβ peptides. This process is thought to be an important step in Aβ fibrilogenesis. Thus, negatively charged membranes can accelerate Aβ aggregation and fibrilization, which is consistent with observations of McLaurin et al. [124, 125].

In monolayer experiments, the electrostatic interactions are screened and the peptide is removed from the surface at modest salt concentrations. It may appear puzzling that going from water to buffer, i.e. closer to physiological conditions, the electrostatic repulsion between phospholipid head groups is increased, but the attraction between head groups and Aβ is

decreased. This can be rationalized by the fact that the Debye screening length decreases to 1 nm on going to 100 mM salt. Hence, since the head groups are closer than 1 nm screening is not very effective and the increased charge density at the interface dominates. On the other hand, the Aβ/head group distance is mostly above 1 nm, and thus the electrostatic interaction is mostly screened.

Opposite to monolayers, interactions between Aβ and negatively charged vesicles are not screened in buffer. This can be rationalized by the fact that the ratio between lipids and counterions is completely different in monolayers and in bulk. It is also possible that the monolayer at 30 mN/m is not the ideal system to model vesicle/peptide interactions. The peptide can partly penetrate into the chain region of vesicles which can in combination with electrostatic interactions provide formation of the helical structure in two hydrophobic regions of the peptide (residues 17-21 and 29-36). The electrostatic interactions between PG headgroups and lysine (residue 28) are not screened in this case since the peptide is stabilized at the vesicle surface *via* the hydrophobic C-terminus. This conclusion is partly supported by monolayer experiments. The peptide remains adsorbed on or partly penetrated into anionic monolayers at high surface pressure when the lipid chains are in the liquid state.

Terzi et al. (1997), Bokvist et al. (2004), Kakio et al. (2002) have shown that the secondary structure of Aβ in the presence of negatively charged vesicles depends on the lipid to peptide ratio (L/P). The peptide adopts β-sheet conformation at L/P below 30, while at higher L/P a conformational change to α-helix was observed. One can expect that Aβ adsorbs to the vesicle surface due to electrostatic interactions. If the L/P ratio is high, the peptide surface concentration is low and the peptide is surrounded by lipids. If the L/P ratio is too low, the peptide surface concentration is high and neighboring peptide molecules can form an intermolecular β-sheet structure. Hence there is a competition between lipids and other Aβ molecules. The pathway random coil – β-sheet – α-helix in experiments with vesicles (constant peptide concentration, increasing lipid concentration) should be similar to monolayer experiments. However, no α-helical secondary structure at the interface was detected by IRRAS. This occurs because for a given binding constant and the concentrations used in the IRRAS experiments, the degree of binding of Aβ is different in the monolayer system compared to the bulk vesicle system. For instance, Terzi et al. [81] used an Aβ concentration of 25 μM and high L/P ratios to observe the transition to α-helix. In an earlier work [126] they used CD and ITC measurements and described

the concentration dependent random coil – β-structure transition by a cooperative aggregation model with an association constant of approximately $1x10^4$ M^{-1}. One can calculate that for this system essentially all Aβ is present in the bound form. In the IRRAS experiments we use a fixed lipid concentration, i.e. a certain area of the water surface is covered with lipid. The Aβ concentration was varied between 0.2 – 0.4 μM. Thus we are in the range of a 1/1 L/P ratio. Therefore, a large excess of lipid molecules to induce the β-sheet - α-helix transition as observed in bulk with vesicle systems is never reached in equilibrium. Because the lipid concentration at the air-water interface is essentially fixed, the only possibility to obtain large L/P ratios is to decrease the Aβ concentration. For a peptide concentration 100-fold lower (0.002 μM) and a L/P ratio of approximately 100, the concentration of bound peptide would be however very small, namely 0.5 nM (only 0.2% of the binding sites are occupied). Such a small amount of peptide cannot be detected using IRRAS or any other technique. It is therefore not surprising that the β-sheet - α-helix transition cannot be observed in the IRRAS experiments after reaching the adsorption equilibrium. However, at the beginning of the adsorption process one can expect high enough L/P ratios. But then the question arises what is the minimum peptide concentration to be detected by IRRAS. Assuming that this minimum peptide concentration at the interface has to be around 0.7 nm^2 per amino acid residue as observed for another model peptide (Kerth et al., 2004), then Aβ occupies an area of less than 30 nm^2. Such an area corresponds to approximately 60 DPPG molecules in the condensed state. Therefore, the L/P ratio would be 60 and one would expect a conformational change to α-helix as observed in bulk. However, the IRRA signal of the peptide is in the resolution limit at such small concentrations and much smaller than signals arising from the lipids and water, and remains therefore maybe undetected. On the other hand, the curvature of the system could play a certain role and the L/P ratio at planar monolayer surfaces has maybe to be larger than at curved vesicle surfaces to induce the transition to α-helix. At higher peptide surface concentration the IRRA signal is strong enough, but the L/P ratio is small and this explains why we observe only β-sheet conformation at the surface. Only in the case of positively charged monolayers the transition from either α-helix or random coil to β-sheet is detected. This might occur because the surface pH is high even when the buffer is used, and it is known that at basic pH the β-sheet formation is inhibited or a much higher concentration of the peptide is required to induce the transition to β-sheet.

From the present results we conclude that Aβ adsorbs only to hydrophobic or charged

surfaces. Increasing peptide concentration leads to conformational changes in the peptide secondary structure from predominantly random coil in solution to pure β-sheet on hydrophobic surfaces and to a mixed α-helix/β-sheet structure on charged surfaces.

7. Conclusions.

Biological membranes are complex systems, therefore simple models may help to better understand processes occurring in nature. Langmuir monolayers are suitable model system to study membrane – ion and membrane - peptide or protein interactions. The system allows applying precise and modern techniques to clarify the structure of lipids and peptides.

In the present work it was demonstrated that alkali cations interact mostly electrostatically with the negatively charged DPPG monolayer. The size and polarizability of ions play only a small role in the monovalent ion - membrane interactions. Moreover, the Gouy-Chapman theory can be successfully applied to elucidate the dissociation constant of the DPPG monolayer. The found value of the pKa is 1 which is very close to the theoretically estimated one. In opposite to monovalent cations, the hydration of divalent cations is very important and the DPPG monolayer structure is strongly influenced by the divalent cation nature. Additionally, studies of ion – membrane interactions can help in understanding the membrane – peptide interactions.

The two peptides investigated in the present work have different structure and properties. However, both peptides are amphipathic and their behavior at the pure air/water interface or adsorbed on lipid monolayers is sometimes similar. Both peptides do not interact with zwitterionic lipid monolayers. Their insertion into these monolayers does not change the lipid phase behavior. This can be understood if one assumes that the peptide – lipid hydrophobic interactions are too weak or that there are no interactions at all. During the lipid LE-LC phase transition, the peptides are likely excluded from the condensed lipid domains. Obviously, the peptides would disturb the van-der-Waals attractions between lipid aliphatic chains. Both peptides interact electrostatically with negatively charged lipid monolayers which leads to a smearing out of the lipid phase transition. These interactions are pronounced in pure water and are screened in the presence of salt or buffer. The screening is more effective in the case of Aβ since this peptide is amphoteric (it has both negatively and positively charged amino acid residues). In general, both peptides are stabilized at the hydrophilic/hydrophobic interface because this reduces the contact of their hydrophobic parts with water. Insertion or even partial penetration into highly compressed lipid monolayers in the absence of electrostatic interactions is not possible since the peptide destabilizes lipid interchain interactions. Therefore, the peptides do not adsorb onto zwitterionic monolayers on both water and buffer and onto charged monolayers

on buffer at a surface pressure above30 mN/m. Furthermore, when the mixed lipid/peptide film is compressed above the peptides equilibrium surface pressure, both peptides are completely squeezed out from the monolayers. To keep the peptides adsorbed on lipid monolayers, stabilization *via* electrostatic interactions is necessary. When a lipid forms a condensed phase the interchain interactions are dominating and electrostatic interactions in the presence of additional inorganic counterions are generally too weak to keep the peptides adsorbed on a negatively charged monolayer. The stabilization of Aβ in negatively charged monolayers was observed only when the lipid monolayer exhibits the disordered LE phase at 30 mN/m. In this case, the peptide inserts at low surface pressure into the monolayer and cannot be squeezed out completely at 30 mN/m. However it does not adsorb to or insert into a compressed LE monolayer.

Both studied peptides are in general unstructured in water or buffer at modest concentrations and are able to form β-sheet rich fibrils at high concentration. However, the structure of the peptides adsorbed at the air/water interface is different: Aβ adopts the β-sheet conformation whereas B18 forms an α-helix. Obviously, both peptides have a random coil conformation in aqueous subphases due to the formation of hydrogen bonds with water molecules. At the interface, the C=O·····HN hydrogen bonds within the same peptide backbone or between neighboring molecules are formed which provides more regular structures in peptides. The difference in the B18 and Aβ surface structures can be rationalized as different modes of structure stabilization by hydrophobic attractions and electrostatic attractions/repulsions. The B18 is positively charged therefore, the repulsions between neighboring peptide molecules do not allow formation of inter-molecular aggregates that is required for β-sheet formation of such short peptides. The formation of β-sheet was observed when B18 adsorbs *via* electrostatic interactions at a negatively charged DPPG monolayer. The positive charges of the peptide are probably screened by the phospholipid negative charge which allows closer packing of the peptide. Thus the β-sheet is formed. In contrast, in Aβ both charges are present therefore the intermolecular β-sheets can be stabilized *via* hydrophobic interactions and salt bridges between oppositely charged amino acid residues. The hydrophobic surfaces are attractive for Aβ and the high surface concentration of the peptide is responsible for the β-sheet formation at the interface. The electrostatic interactions between SDS micelles or DMPG vesicles and Aβ lead to the formation of the α-helical structure. It can happen that the intermolecular salt bridges are destroyed in the vicinity of highly charged surfaces and the peptide adopts α-helical conformation in its

monomeric form. This conclusion is supported by the fact that the α-helix or β-sheet transition is observed when the lipid to peptide ratio decreases. Since in monolayer experiments this ratio is always too low, the pure α-helix was not observed when Aβ was adsorbing on negatively charged monolayers. The interactions of Aβ with positively charged surfaces (monolayers or vesicles) lead to similar effects. At a low lipid to peptide ratio, Aβ forms β-sheets while it adopts the α-helical conformation at high ratio. This can be understood as the competitive electrostatic interactions between oppositely charged residues of neighboring peptides and between the peptide and lipid.

The observed tendencies when the peptides interact with lipid monolayers are helpful for understanding the mechanism of their actions *in vivo*. Apparently, Aβ peptide accumulation in the brain is concentration driven. Increasing the Aβ concentration leads to a change in the lipid to peptide ratio that induces the β-sheet formation. B18 inserts into zwitterionic membranes especially in the presence of Zn^{2+} and likely forms an α-helical structure. It can also form β-sheets at negatively charged membranes. The presence of B18 in the hydrophobic membrane core or at the surface may induce membrane fusion because the lipid/lipid interactions are perturbed. Unfortunately at the present stage one cannot say if the monolayer at 30 mN/m is a good model for the lipid bilayers. The difference in the results obtained with monolayers and vesicles may have its origin in a different access of the lipid bilayers for peptides which cannot be compared with the adsorption of the peptide to lipid monolayers compressed to 30 mN/m because of non comparable thickness of the hydrophobic core. However, the monolayer experiments clarify which type of interactions is responsible for the peptide folding at membrane surfaces.

Appendix 1

Table A1

Twenty natural amino acids with abbreviation codes, side chain chemical structures, polarity and pK values of charged groups in proteins [16], the character of ionic forms is given for pH 6-7. The general structure of amino acids is NH_2-CH(R)-COOH, where R is the side group.

Code	Name	Side group	Character	Typical pK* value
A	Alanine	$-CH_3$	non-polar	
R	Arginine	$-(CH_2)_3NHC(NH)NH_2$	basic	12.0
N	Asparagine	$-CH_2CONH_2$	neutral	
D	Aspartic acid	$-CH_2COOH$	acidic	4.4
C	Cysteine	$-CH_2SH$	neutral	8.5
Q	Glutamine	$-CH_2CH_2CONH_2$	neutral	
E	Glutamic acid	$-CH_2CH_2COOH$	acidic	4.4
G	Glycine	-H	non-polar	
H	Histidine	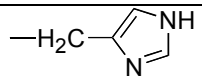	basic	6.5
I	Isoleucine	$-CH(CH_3)CH_2CH_3$	non-polar	
L	Leucine	$-CH_2CH(CH_3)_2$	non-polar	
K	Lysine	$-(CH_2)_4NH_2$	basic	10.0
M	Methionine	$-(CH_2)_2SHCH_3$	non-polar	
F	Phenylalanine	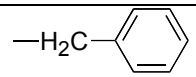	non-polar	
P**	Proline	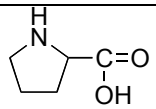	non-polar	
S	Serine	$-CH_2OH$	neutral	
T	Threonine	$-CH(CH_3)OH$	neutral	
W	Tryptophane	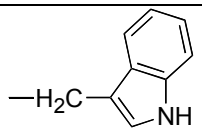	non-polar	
Y	Tyrosine	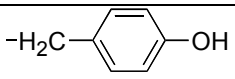	neutral	10.0
V	Valine	$-CH(CH_3)_2$	non-polar	

*pK values depend on the temperature, ionic strength and microenvironment

**The full structure of proline is given

Appendix 2

Chemical structures of main lipids used in this work

1,2-dimyristoyl- (DMPE) and 1,2-dipalmitoyl-sn-glycero-3-phosphoethanolamine (DPPE)

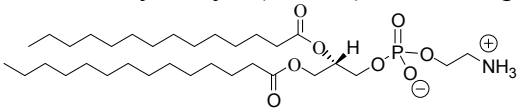

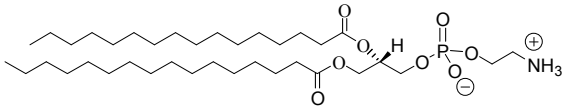

1,2-dimyristoyl- (DMPC) and 1,2-dipalmitoyl-sn-glycero-3-phosphocholine (DPPC)

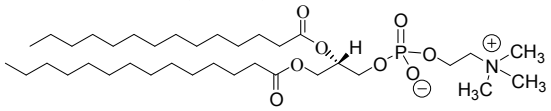

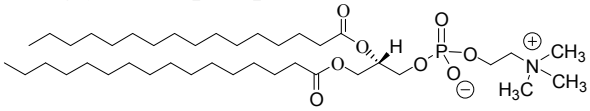

1,2-dimyristoyl- (DMPG) and 1,2-dipalmitoyl sn-glycero-3-[phospho-rac-(1-glycerol)] (DPPG) sodium salt

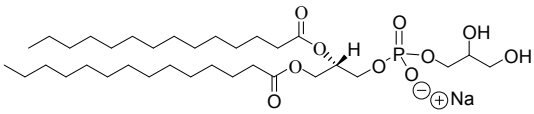

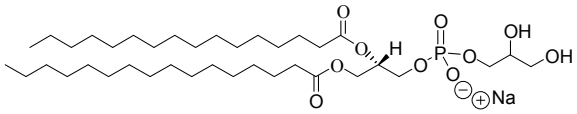

1,2-dipalmitoyl-sn-glycero-3-[phospho-L-serine] sodium salt (DPPS)

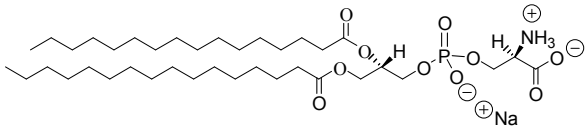

1,2-dipalmitoyl- (DPTAP) and 1,2-distearoyl-3-trimethylammonium-propane chloride (DSTAP)

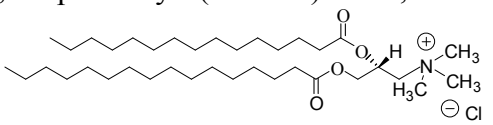

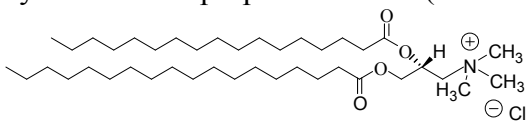

1-palmitoyl-2-oleoyl-sn-glycero-3-[phospho-rac-(1-glycerol)] sodium salt (POPG)

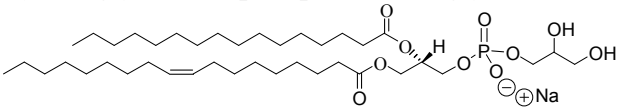

1-palmitoyl-2-[6-[(7-nitro-2-1,3-benzoxadiazol-4-yl)amino]-dodecanoy]- sn-glycero-3-phosphocholine (NBD-PC)

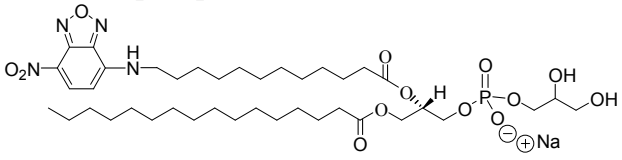

Table A2
Important absorption bands of phospholipids and peptides

Assignment	Approximate frequency, cm^{-1}	Description
Amide A, N-H-stretching (ν)	~3305 3275-3230	α-helix [38] β-sheet [38]
CH_3 asymmetrical stretch (ν_{as})	~2960	weak, compared to CH_2
CH_2 asymmetrical stretch (ν_{as})	~2924 2920-2916	LE phase of lipids [40] condensed phase of lipids [40]
CH_3 symmetrical stretch (ν_s)	~2870	weak, compared to CH_2
CH_2 symmetrical stretch (ν_s)	~2854 2851-2949	LE phase of lipids [40] condensed phase of lipids [40]
C=O stretching (ν) of lipids ester group	~1735	sensitive to hydration and hydrogen bonding [47]
Amide I, mostly C=O stretching (~70-80 %) of peptides and proteins amide bond with small contribution of C-N stretching (~20 %) and C-CN deformation (~10 %)	1650-1660 1645-1660 1665-1676 1620-1640 1685-1695	α-helix [38] random coil [54] turn [38] β-sheet [38] usually appear as a shoulder for antiparallel β-sheet [38]
Amide II, results from in-plane NH-bending (δ) (~40-60 %), C-N stretching (~20-40 %) and some contribution of C-C stretching (~10 %)	1510-1580	Usually band is too complex, rarely used for secondary structure determination [38]
CH_2 scissoring (δ)	~1465 1467-1469 ~1471 1462,1473	disordered phase hexagonal triclinic packing orthorhombic phase doublet
Amide III, mostly in-plane N-H bending (δ)	1200-1400	Very complex and weak [38]
PO_2^- asymmetrical stretching (ν_{as})	1240-1205	sensitive to hydration, ion binding and hydrogen bonding [47]
CO-O-C asymmetrical stretching (ν_{as})	~1170	
PO_2^- symmetrical stretching (ν_s)	1085-1090	hydration sensitive [50]
PO_3^{2-} asymmetrical stretching (ν_{as})	1074-1086	observed for phosphatidic acid with Ca^{2+} [51]
CO-O-C symmetrical stretching (ν_s)	~1070	
C-O-P-O-C stretching (ν)	~1060	
PO_3^{2-} symmetrical stretching (ν_s)	1012-1000	observed for phosphatidic acid with Ca^{2+} [51]
$N(CH_3)_3^+$ asymmetrical stretching (ν_{as})	~972	

Appendix 3

For all tables in appendix 3 the best-fit values of the in-plane and out-of-plane scattering vector components Q_{xy} and Q_z, lattice parameters, tilt angle t, chain in-plane area A_{xy} and chain cross-sectional area A_0 are given.

Table A3.1

DPPG monolayers on subphases containing 0.1 M Cs^+ at various pH.

pH of a subphase	π, mN/m	Q_{xy}, Å^{-1}	Q_z, Å^{-1}	Lattice parameters,	tilt, deg.	A_{xy}, Å^2	A_0, Å^2
2*	25	1. 1.502 2. 1.486	1. 0 2. 0.274	a = 4.9 Å, b = 4.85 Å, γ = 120,4º	12.1	20.5	20.0
	30	1. 1.510 2. 1.499	1. 0 2. 0.11	a = 4.85 Å, b = 4.82 Å, γ = 120,24º	5.0	20.2	20.1
	35	1.510	0	a = 4.79 Å, γ = 120º	0.0	19.9	
2	25	1. 1.496 2. 1.485 3. 1.457	1. 0.03 2. 0.33 3. 0.36	a = 4.83 Å, b = 4.92 Å, γ = 118,9º	15.3	20.8	20.1
	35	1. 1.510 2. 1.501	1. 0 2. 0.16	a = 4.84 Å, b = 4.82 Å, γ = 120,2º	7.0	20.2	20.0
3	25	1. 1.487 2. 1.457 3. 1.424	1. 0.03 2. 0.42 3. 0.45	a = 4.87 Å, b = 4.99 Å, γ = 117,8º	19.5	21.5	20.3
	35	1. 1.505 2. 1.492	1. 0 2. 0.22	a = 4.88 Å, b = 4.84 Å, γ = 120,3º	9.7	20.4	20.1
4	20	1. 1.474 2. 1.397	0 0.62	a = 5.30 Å, b = 5.02 Å, γ = 121.9º	27.7	22.6	20.0
	25	1. 1.476 2. 1.407	1. 0 2. 0.59	a = 5.24 Å, b = 5.0 Å, γ = 121.6º	26.2	22.3	20.0
7	25	1. 1.465 2. 1.346	1. 0 2. 0.72	a = 5.56 Å, b = 5.11 Å, γ = 123.0º	32.4	23.9	20.1
	35	1. 1.471 2. 1.372	1. 0 2. 0.64	a = 5.42 Å, b = 5.06 Å, γ = 122.4º	29.0	23.2	20.3
	45	1. 1.476 2. 1.454 3. 1.397	1. 0.07 2. 0.51 3. 0.58	a = 4.88 Å, b = 5.08 Å, γ = 117.7º	22.7	22.0	20.2
7**	25	1. 1.469 2. 1.379 3. 1.351	1. 0.05 2. 0.65 3. 0.73	a = 5.02 Å, b = 5.13 Å, γ = 114.9º	31.0	23.4	20.0
	35	1. 1.477 2. 1.413 3. 1.388	1. 0.06 2. 0.56 3. 0.63	a = 4.96 Å, b = 5.05 Å, γ = 116.4º	26.6	22.5	20.1
	45	1. 1.485 2. 1.442 3. 1.420	1. 0.07 2. 0.44 3. 0.51	a = 4.91 Å, b = 4.98 Å, γ = 117.6º	21.4	21.7	20.2

- no alkali cations, ** lithium is used instead of cesium

Table A3.2

DPPG monolayers on subphases containing 0.01 M Cs^+ with various pH at 25 mN/m.

pH of a subphase	Q_{xy}, Å^{-1}	Q_z, Å^{-1}	Lattice parameters	tilt, deg.	A_{xy}, Å^2	A_0, Å^2
3	1. 1.502 2. 1.484	1. 0 2. 0.28	a = 4.91 Å, b = 4.85 Å, γ = 120.5º	12.5	20.6	20.1
4	1. 1.487 2. 1.458 3. 1.427	1. 0.10 2. 0.41 3. 0.51	a = 4.88 Å, b = 4.99 Å, γ = 118.0º	20.7	21.5	20.1
5	1. 1.471 2. 1.390 3. 1.361	0.07 0.62 0.68	a = 5.0 Å, b = 5.11 Å, γ = 115.4º	29.3	23.1	20.1
7	1. 1.466 2. 1.346	1. 0.0 2. 0.74	a = 5.56 Å, b = 5.11 Å, γ = 123.0º	32.5	23.9	20.1

Table A3.3

DPPG monolayer on pure water.

π, mN/m	Q_{xy}, Å^{-1}	FWHM, Å^{-1}	Q_z, Å^{-1}	FWHM, Å^{-1}	a, Å	b, Å	γ, deg.	tilt, deg	A_{xy}, Å^2	A_0, Å^2
12	1.412 1.450 1.483	0.026 0.024 0.013	0.56 0.47 0.09	0.28 0.28 0.28	4.89	5.02	117.6	23.1	21.8	20.0
20	1.443 1.472 1.491	0.022 0.021 0.012	0.45 0.36 0.09	0.30 0.30 0.30	4.86	4.95	118.5	18.3	21.2	20.1
30	1.447 1.496 1.502	0.024 0.020 0.013	0.30 0.24 0.06	0.29 0.29 0.29	4.82	4.88	119.3	12.1	20.5	20.0
37	1.511 1.509	0.13 0.18	0.0 0.12	0.29 0.29	4.81	4.80	120.2	5.0	20.0	19.9
45	1.516	0.011	0.0	0.26	4.79		120	0.0	19.8	19.8

Table A3.4

DPPG monolayer on phosphate buffered saline with pH 7.4, 0.13 M Na^+, 0.008 M K^+.

π, mN/m	Q_{xy}, Å^{-1}	FWHM, Å^{-1}	Q_z, Å^{-1}	FWHM, Å^{-1}	a, Å	b, Å	γ, deg.	tilt, deg	A_{xy}, Å^2	A_0, Å^2
15	1.296 1.325 1.459	0.049 0.047 0.013	0.81 0.73 0.06	0.30 0.30 0.29	5.13	5.24	112.4	35.4	24.9	20.3
20	1.315 1.345 1.462	0.053 0.045 0.012	0.77 0.71 0.06	0.29 0.29 0.29	5.09	5.20	113.3	33.8	24.3	20.2
30	1.356 1.384 1.470	0.054 0.042 0.012	0.69 0.65 0.04	0.29 0.29 0.29	5.01	5.12	115.1	30.3	23.2	20.1
35	1.375 1.403 1.474	0.052 0.048 0.015	0.66 0.58 0.08	0.29 0.29 0.29	4.98	5.08	115.9	27.8	22.8	20.1
40	1.394 1.420 1.478	0.050 0.057 0.017	0.62 0.56 0.06	0.28 0.28 0.29	4.95	5.04	116.7	26.4	22.3	20.0
45	1.412 1.435 1.482	0.049 0.054 0.017	0.57 0.46 0.11	0.30 0.30 0.30	4.96	5.01	117.3	23.5	21.9	20.1

Table A3.5
DPPG monolayer on 0.005 M Mg^{2+}.

π, mN/m	**Q_{xy}, Å^{-1}**	**FWHM, Å^{-1}**	**Q_z, Å^{-1}**	**FWHM, Å^{-1}**	**a, Å**	**b, Å**	**γ, deg.**	**tilt, deg**	**A_{xy}, Å^2**	**$A_{0,}$ Å^2**
4.1	1.317 1.351 1.462	0.035 0.035 0.012	0.76 0.71 0.05	0.28 0.28 0.28	5.07	5.20	113.6	33.5	24.2	20.2
8.2	1.330 1.363 1.464	0.040 0.036 0.012	0.74 0.71 0.03	0.28 0.28 0.28	5.05	5.18	114.2	32.5	23.9	20.1
12.4	1.346 1.379 1.467	0.038 0.033 0.012	0.71 0.68 0.03	0.28 0.28 0.28	5.02	5.15	114.9	31.3	23.4	20.0
16.5	1.361 1.393 1.471	0.032 0.034 0.012	0.70 0.63 0.06	0.30 0.28 0.29	5.00	5.11	115.4	29.9	23.1	20.0
20.6	1.382 1.412 1.476	0.041 0.027 0.012	0.08 0.56 0.64	0.28 0.30 0.28	4.96	5.07	116.2	27.0	22.6	20.1
25	1.396 1.423 1.479	0.044 0.022 0.012	0.60 0.52 0.08	0.30 0.29 0.30	4.94	5.04	116.7	25.3	22.3	20.1
29	1.410 1.437 1.483	0.031 0.026 0.013	0.56 0.49 0.07	0.30 0.30 0.28	4.92	5.01	117.3	23.8	21.9	20.1
33	1.419 1.443 1.485	0.032 0.028 0.013	0.53 0.50 0.03	0.29 0.29 0.29	4.91	4.99	117.5	22.9	21.7	20.0
35	1.429 1.450 1.488	0.034 0.024 0.012	0.50 0.45 0.05	0.28 0.28 0.28	4.90	4.97	117.8	21.2	21.5	20.1
40	1.446 1.464 1.492	0.036 0.024 0.013	0.45 0.41 0.04	0.30 0.30 0.30	4.88	4.94	118.3	19.1	21.2	20.0
45	1.462 1.475 1.497	0.039 0.040 0.014	0.40 0.35 0.05	0.28 0.28 0.28	4.86	4.90	118.7	16.4	20.9	20.0
50	1.486 1.501	0.047 0.013	0.26 0.0	0.30 0.30	4.90	4.85	120.4	11.5	20.5	20.1

Table A3.6
DPPG monolayer on 0.005 M Ca^{2+}.

π, mN/m	Q_{xy}, **Å^{-1}**	**FWHM, Å^{-1}**	Q_z, **Å^{-1}**	**FWHM, Å^{-1}**	**a, Å**	**b, Å**	**γ, deg.**	**tilt, deg**	A_{xy}, **Å^2**	A_0, **Å^2**
5.3	1.357 1.392 1.470	0.039 0.030 0.012	0.70 0.62 0.08	0.27 0.27 0.28	5.00	5.12	115.3	29.7	23.1	20.1
10	1.375 1.409 1.474	0.033 0.030 0.012	0.66 0.59 0.07	0.27 0.27 0.28	4.97	5.09	116.1	28.1	22.7	20.0
15	1.394 1.425 1.479	0.031 0.032 0.012	0.61 0.54 0.07	0.30 0.28 0.27	4.93	5.05	116.7	25.8	22.2	20.0
20	1.414 1.443 1.485	0.036 0.026 0.012	0.52 0.46 0.06	0.30 0.30 0.28	4.90	5.00	117.4	22.0	21.8	20.2
25	1.434 1.460 1.490	0.043 0.025 0.013	0.48 0.43 0.05	0.29 0.29 0.29	4.88	4.97	118.0	20.3	21.4	20.0
30	1.468 1.475 1.494	0.058 0.019 0.013	0.41 0.35 0.06	0.28 0.28 0.28	4.87	4.89	119.0	16.8	20.8	20.0
35.5	1.469 1.487 1.500	0.036 0.036 0.014	0.33 0.29 0.04	0.30 0.30 0.30	4.83	4.89	119.0	13.8	20.7	20.1
40	1.493 1.504	0.046 0.013	0.24 0.0	0.29 0.29	4.87	4.84	120.3	10.6	20.4	20.0
45	1.502 1.508	0.034 0.013	0.19 0.0	0.30 0.30	4.84	4.82	120.1	8.3	20.2	19.9
50	1.514	0.015	0.0	0.30	4.79	4.79	120	0.0	19.9	

Table A3.7
DPPG monolayer on 0.005 M Cu^{2+}.

π, mN/m	**Q_{xy}, Å^{-1}**	**FWHM, Å^{-1}**	**Q_z, Å^{-1}**	**FWHM, Å^{-1}**	**a, Å**	**b, Å**	**γ, deg.**	**tilt, deg**	**A_{xy}, Å^2**	**A_0, Å^2**
5	1.360 1.397 1.471	0.054 0.031 0.013	0.68 0.60 0.08	0.28 0.28 0.27	4.98	5.12	115.5	29.0	23.0	20.2
16	1.413 1.443 1.484	0.052 0.029 0.014	0.56 0.45 0.11	0.28 0.28 0.28	4.90	5.01	117.4	22.9	21.8	20.1
25	1.474 1.482 1.497	0.050 0.025 0.016	0.32 0.26 0.08	0.28 0.30 0.28	4.84	4.90	118.9	13.0	20.8	20.2
30	1.492 1.507	0.026 0.015	0.25 0.0	0.27 0.30	4.87	4.83	120.3	10.8	20.4	20.0
35	1.512	0.013	0.0	0.30	4.80	4.80	120	0.0	19.9	
40	1.514	0.014	0.0	0.27	4.79	4.79	120	0.0	19.9	

Table A3.8
DPPG monolayer on 0.005 M Zn^{2+}.

π, mN/m	**Q_{xy}, Å^{-1}**	**FWHM, Å^{-1}**	**Q_z, Å^{-1}**	**FWHM, Å^{-1}**	**a, Å**	**b, Å**	**γ, deg.**	**tilt, deg**	**A_{xy}, Å^2**	**A_0, Å^2**
5	1.385 1.419 1.476	0.045 0.035 0.013	0.61 0.63 0.08	0.30 0.28 0.30	4.95	5.07	116.5	25.7	22.4	20.2
15	1.429 1.459 1.489	0.035 0.039 0.016	0.53 0.40 0.12	0.28 0.28 0.28	4.88	4.97	118.0	21.1	21.4	20.0
25	1.485 1.502	0.042 0.016	0.24 0.0	0.30 0.30	4.90	4.85	120.4	10.6	20.5	20.2
30	1.502 1.510	0.032 0.015	0.16 0.0	0.30 0.30	4.85	4.82	120.2	7.0	20.2	20.0
35	1.513	0.014	0.0	0.28	4.80	4.80	120	0.0	19.9	

Table A3.9

DPPC monolayer on 0.01 M Hepes, 0.1 M NaCl with pH 7.4.

π, mN/m	**Q_{xy}, Å^{-1}**	**FHWM, Å^{-1}**	**Q_z, Å^{-1}**	**FHWM, Å^{-1}**	**a, Å**	**b, Å**	**γ, deg.**	**tilt, deg**	**A_{xy}, Å^2**	**A_0, Å^2**
10	1.270 1.293 1.457	0.047 0.059 0.013	0.85 0.76 0.09	0.30 0.28 0.28	5.19	5.29	110.7	37.5	25.7	20.3
20	1.303 1.322 1.461	0.054 0.050 0.013	0.83 0.75 0.08	0.30 0.30 0.30	5.14	5.21	112.4	36.2	24.8	20.0
25	1.319 1.337 1.463	0.050 0.080 0.015	0.79 0.71 0.08	0.30 0.29 0.30	5.11	5.18	113.2	34.3	24.4	20.1
30	1.333 1.357 1.465	0.067 0.089 0.018	0.74 0.65 0.09	0.30 0.30 0.30	5.07	5.16	114.0	32.0	23.9	20.3
40	1.366 1.437 1.469	0.087 0.088 0.027	0.66 0.51 0.15	0.30 0.30 0.30	4.90	5.15	116.8	26.9	22.5	20.1
45	1.386 1.447 1.471	0.110 0.063 0.029	0.61 0.45 0.16	0.30 0.30 0.30	4.89	5.11	117.5	24.5	22.2	20.2
50	1.394 1.447 1.474	0.091 0.057 0.030	0.59 0.42 0.17	0.30 0.30 0.30	4.89	5.08	117.5	23.6	22.1	20.2

Table A3.10

DPPC monolayer on 0.01 M Hepes, 0.1 M NaCl, 0.001 M $ZnCl_2$ with pH 7.4.

π, mN/m	**Q_{xy}, Å^{-1}**	**FHWM, Å^{-1}**	**Q_z, Å^{-1}**	**FHWM, Å^{-1}**	**a, Å**	**b, Å**	**γ, deg.**	**tilt, deg**	**A_{xy}, Å^2**	**A_0, Å^2**
10	1.270 1.290 1.458	0.040 0.064 0.013	0.84 0.76 0.08	0.30 0.30 0.30	5.20	5.28	110.5	37.4	25.7	20.4
20	1.323 1.347 1.466	0.046 0.051 0.013	0.77 0.69 0.08	0.29 0.29 0.29	5.08	5.18	113.4	33.3	24.1	20.2
30	1.338 1.363 1.468	0.045 0.060 0.015	0.75 0.66 0.09	0.29 0.29 0.30	5.05	5.15	114.1	32.1	23.7	20.1
45	1.384 1.415 1.477	0.048 0.077 0.019	0.64 0.53 0.11	0.28 0.29 0.29	4.96	5.07	116.3	26.6	22.5	20.1

Table A3.11

DPPC monolayer on B18 in 0.01 M Hepes, 0.1 M NaCl with pH 7.4.

π, mN/m	**Q_{xy}, Å^{-1}**	**FHWM, Å^{-1}**	**Q_z, Å^{-1}**	**FHWM, Å^{-1}**	**a, Å**	**b, Å**	**γ, deg.**	**tilt, deg**	**A_{xy}, Å^2**	**A_0, Å^2**
20	1.310 1.330 1.463	0.051 0.046 0.015	0.82 0.74 0.08	0.29 0.29 0.30	5.12	5.20	112.7	35.5	24.6	20.0
30	1.330 1.359 1.465	0.055 0.055 0.016	0.76 0.69 0.07	0.30 0.30 0.30	5.06	5.17	114.0	32.2	23.9	20.1
35	1.346 1.374 1.468	0.034 0.046 0.019	0.72 0.62 0.10	0.29 0.29 0.29	5.03	5.14	114.7	30.6	23.5	20.2
40	1.360 1.490 1.473	0.087 0.088 0.034	0.70 0.56 0.14	0.30 0.30 0.30	4.99	5.11	115.2	29.0	23.1	20.2

Table A3.12

DPPC monolayer on B18 in 0.01 M Hepes, 0.1 M NaCl, 0.001 M $ZnCl_2$ with pH 7.4.

π, mN/m	**Q_{xy}, Å^{-1}**	**FHWM, Å^{-1}**	**Q_z, Å^{-1}**	**FHWM, Å^{-1}**	**a, Å**	**b, Å**	**γ, deg.**	**tilt, deg**	**A_{xy}, Å^2**	**A_0, Å^2**
20	1.320 1.360 1.465	0.061 0.024 0.019	0.81 0.71 0.10	0.29 0.29 0.29	5.04	5.20	113.8	34.34	24.0	19.9
25	1.342 1.374 1.469	0.046 0.049 0.015	0.74 0.62 0.09	0.29 0.29 0.29	5.03	5.15	114.5	30.4	23.5	20.3
30	1.354 1.380 1.470	0.046 0.052 0.014	0.71 0.62 0.09	0.29 0.29 0.30	5.02	5.12	114.9	30.0	23.3	20.2
45	1.407 1.431 1.480	0.069 0.079 0.020	0.59 0.51 0.08	0.29 0.29 0.30	4.93	5.02	117.2	24.6	22.2	20.1

Table A3.13

DPPG monolayer on B18 in phosphate buffered saline, 0.13 M Na^+, 0.08 M K^+, with pH 7.4.

π, mN/m	**Q_{xy}, Å^{-1}**	**FHWM, Å^{-1}**	**Q_z, Å^{-1}**	**FHWM, Å^{-1}**	**a, Å**	**b, Å**	**γ, deg.**	**tilt, deg**	**A_{xy}, Å^2**	**A_0, Å^2**
25	1.330 1.362 1.464	0.068 0.075 0.023	0.75 0.69 0.06	0.29 0.29 0.30	5.05	5.18	114.1	32.6	23.9	20.1
30	1.353 1.388 1.467	0.065 0.052 0.023	0.66 0.72 0.06	0.30 0.30 0.30	5.01	5.14	115.3	31.1	23.3	19.9
40	1.393 1.413 1.476	0.041 0.090 0.028	0.62 0.47 0.15	0.29 0.29 0.30	4.97	5.04	116.5	25.0	22.4	20.3
45	1.413 1.449 1.480	0.073 0.035 0.025	0.57 0.43 0.14	0.29 0.29 0.30	4.90	5.02	117.7	22.9	21.8	20.1

Table A3.14
DPPE monolayer on pure water.

π, mN/m	Q_{xy}, Å^{-1}	FHWM, Å^{-1}	Q_z, Å^{-1}	FHWM, Å^{-1}	a, Å	b, Å	γ, deg.	tilt, deg	A_{xy}, Å^2	A_0, Å^2
5	1.392 1.431 1.476	0.024 0.031 0.012	0.63 0.55 0.08	0.27 0.27 0.27	4.93	5.06	117.0	26.4	22.3	19.9
10	1.411 1.444 1.480	0.023 0.024 0.012	0.57 0.50 0.07	0.29 0.27 0.28	4.90	5.02	117.6	23.9	21.9	20.0
20	1.449 1.472 1.4905	0.020 0.020 0.012	0.44 0.37 0.07	0.27 0.27 0.28	4.86	4.94	118.6	18.0	21.1	20.1
25	1.462 1.482 1.495	0.023 0.021 0.013	0.375 0.309 0.066	0.28 0.29 0.28	4.85	4.91	119.0	15.3	20.8	20.1
30	1.500 1.491	0.015 0.021	0 0.28	0.29 0.30	4.86	4.85	120.2	12.3	20.4	20.0
40	1.512	0.013	0	0.29	4.80	4.80	120	0	19.9	19.9

Table A3.15
DMPE monolayer on pure water.

π, mN/m	Q_{xy}, Å^{-1}	FHWM, Å^{-1}	Q_z, Å^{-1}	FHWM, Å^{-1}	a, Å	b, Å	γ, deg.	tilt, deg	A_{xy}, Å^2	A_0, Å^2
10	1.405 1.437 1.472	0.027 0.029 0.014	0.58 0.45 0.13	0.28 0.28 0.28	4.93	5.05	117.6	23.5	22.1	20.2
20	1.440 1.462 1.480	0.021 0.032 0.014	0.43 0.30 0.13	0.29 0.29 0.29	4.90	4.97	118.7	17.0	21.4	20.4
30	1.483 1.487	0.021 0.015	0.23 0.0	0.29 0.28	4.89	4.88	120.1	10.1	20.7	20.4
40	1.497	0.013	0	0.31	4.85	4.85	120	0	20.4	20.4

Table A3.16
DPPC monolayer on pure water.

π, mN/m	Q_{xy}, Å^{-1}	FHWM, Å^{-1}	Q_z, Å^{-1}	FHWM, Å^{-1}	a, Å	b, Å	γ, deg.	tilt, deg	A_{xy}, Å^2	A_0, Å^2
15	1.299 1.303 1.461	0.045 0.074 0.015	0.82 0.74 0.08	0.30 0.30 0.30	5.19	5.21	111.7	35.9	25.10	20.3
25	1.326 1.327 1.466	0.031 0.077 0.016	0.77 0.71 0.06	0.30 0.30 0.30	5.14	5.15	112.9	33.8	24.4	20.3
35	1.341 1.370 1.470	0.052 0.067 0.019	0.72 0.60 0.12	0.30 0.30 0.30	5.03	5.14	114.4	30.4	23.6	20.3
45	1.380 1.410 1.477	0.067 0.060 0.030	0.63 0.46 0.17	0.29 0.29 0.29	4.95	5.08	116.1	27.6	22.6	20.0

Table A3.17
DSTAP monolayer on pure water.

π, mN/m	Q_{xy}, Å^{-1}	FHWM, Å^{-1}	Q_z, Å^{-1}	FHWM, Å^{-1}	a, Å	b, Å	γ, deg.	tilt, deg	A_{xy}, Å^2	A_0, Å^2
1.2	1.292 1.445	0.052 0.012	0.84 0.0	0.28 0.28	5.84	5.24	123.9	37.8	25.4	20.1
10	1.331 1.452	0.045 0.012	0.79 0.0	0.28 0.27	5.63	5.16	123.1	35.2	24.4	19.9
20	1.372 1.463	0.036 0.014	0.71 0.0	0.27 0.27	5.41	5.08	122.2	31.6	23.3	19.8
30	1.419 1.476	0.042 0.013	0.59 0.0	0.27 0.26	5.19	4.98	121.4	25.9	22.1	19.9
40	1.446 1.486	0.037 0.017	0.50 0.0	0.27 0.26	5.06	4.93	120.9	22.0	21.4	19.9
50	1.469 1.487	0.076 0.014	0.46 0.0	0.25 0.27	4.96	4.90	120.4	20.1	21.0	19.7

Table A3.18
DSTAP monolayer on 0.001 M NaCl.

π, mN/m	Q_{xy}, Å^{-1}	FHWM, Å^{-1}	Q_z, Å^{-1}	FHWM, Å^{-1}	a, Å	b, Å	γ, deg.	tilt, deg	A_{xy}, Å^2	A_0, Å^2
5	1.289 1.443	0.046 0.013	0.87 0.0	0.29 0.29	5.88	5.25	124.0	39.1	25.6	19.9
20	1.336 1.452	0.042 0.013	0.79 0.0	0.29 0.27	5.60	5.15	122.9	35.2	24.2	19.8
30	1.368 1.459	0.042 0.014	0.71 0.0	0.27 0.26	5.43	5.09	122.2	31.6	23.4	19.9
40	1.397 1.471	0.039 0.019	0.65 0.0	0.26 0.26	5.29	5.02	121.8	28.7	22.6	19.8

Table A3.19
DSTAP monolayer on phosphate buffered saline, 0.13 M Na^+, 0.08 M K^+, with pH 7.4.

π, mN/m	Q_{xy}, Å^{-1}	FHWM, Å^{-1}	Q_z, Å^{-1}	FHWM, Å^{-1}	a, Å	b, Å	γ, deg.	tilt, deg	A_{xy}, Å^2	A_0, Å^2
5	1.290 1.443	0.048 0.012	0.86 0.0	0.28 0.29	5.88	5.25	124.0	38.7	25.6	20.0
10	1.307 1.446	0.047 0.012	0.83 0.0	0.29 0.28	5.77	5.22	123.6	37.4	25.1	19.9
15	1.321 1.450	0.044 0.013	0.81 0.0	0.29 0.28	5.69	5.18	123.3	36.2	24.7	19.9
20	1.336 1.452	0.040 0.013	0.80 0.0	0.28 0.28	5.60	5.15	122.9	35.4	24.2	19.8
30	1.369 1.459	0.044 0.013	0.70 0.0	0.26 0.26	5.42	5.09	122.2	31.3	23.4	20.0
40	1.395 1.465	0.046 0.015	0.67 0.0	0.26 0.27	5.29	5.04	121.7	29.4	22.7	19.8

Table A3.20

DPPE monolayer on 0.3 μM Aβ in pure water.

π, mN/m	Q_{xy}, Å^{-1}	FHWM, Å^{-1}	Q_z, Å^{-1}	FHWM, Å^{-1}	a, Å	b, Å	γ, deg.	tilt, deg	A_{xy}, Å^2	A_0, Å^2
17.5	1.435 1.462 1.485	0.019 0.036 0.013	0.516 0.395 0.121	0.29 0.29 0.29	4.88	4.97	118.3	19.5	21.4	20.0
20	1.451 1.476 1.490	0.35 0.38 0.016	0.42 0.33 0.09	0.29 0.29 0.29	4.86	4.94	118.8	17.6	20.9	20.0
30	1.498 1.489	0.0145 0.037	0 0.26	0.29 0.29	4.88	4.85	120.2	11.4	20.5	20.1
40	1.510	0.013	0	0.28	4.80	4.80	120	0	20.0	20.0

Table A3.21

DMPE monolayer on 0.3 μM Aβ in pure water.

π, mN/m	Q_{xy}, Å^{-1}	FHWM, Å^{-1}	Q_z, Å^{-1}	FHWM, Å^{-1}	a, Å	b, Å	γ, deg.	tilt, deg	A_{xy}, Å^2	A_0, Å^2
19.8	1.448 1.465 1.481	0.020 0.028 0.013	0.40 0.31 0.09	0.29 0.29 0.29	4.90	5.01	118.9	16.2	21.3	20.4
30	1.487 1.491	0.070 0.012	0 0.17	0.29 0.29	4.88	4.87	120.1	7.5	20.5	20.4
40	1.496	0.013	0	0.30	4.85	4.85	120	0	20.4	20.4

Table A3.22

DPPC monolayer on 0.3 μM Aβ in pure water.

π, mN/m	Q_{xy}, Å^{-1}	FHWM, Å^{-1}	Q_z, Å^{-1}	FHWM, Å^{-1}	a, Å	b, Å	γ, deg.	tilt, deg	A_{xy}, Å^2	A_0, Å^2
15	1.302 1.335 1.462	0.048 0.036 0.013	0.81 0.71 0.10	0.30 0.30 0.30	5.10	5.73	112.7	34.6	24.6	20.3
20	1.323 1.338 1.466	0.043 0.056 0.015	0.76 0.69 0.07	0.30 0.30 0.30	5.10	5.68	112.9	33.5	24.4	20.3
30	1.345 1.369 1.471	0.058 0.049 0.015	0.71 0.63 0.08	0.30 0.30 0.30	5.04	5.51	114.4	30.6	23.5	20.3
40	1.376 1.427 1.474	0.046 0.060 0.015	0.67 0.56 0.09	0.30 0.30 0.30	4.92	5.11	116.6	27.0	22.5	20.0

Table A3.23

DPPC monolayer on 0.3 μM Aβ in 0.01 M Hepes, 0.1 M NaCl, pH 7.4.

π, mN/m	Q_{xy}, Å^{-1}	FHWM, Å^{-1}	Q_z, Å^{-1}	FHWM, Å^{-1}	a, Å	b, Å	γ, deg.	tilt, deg	A_{xy}, Å^2	A_0, Å^2
15	1.296 1.459	0.070 0.014	0.80 0.0	0.30 0.31	5.86	5.21	124.3	36.9	25.3	20.2
40	1.347 1.375 1.469	0.48 0.58 0.016	0.71 0.64 0.07	0.29 0.29 0.29	5.03	5.13	114.7	31.1	23.5	20.1

Table A3.24

DPPG monolayer on 0.3 μM Aβ in pure water.

π, mN/m	Q_{xy}, Å^{-1}	FHWM, Å^{-1}	Q_z, Å^{-1}	FHWM, Å^{-1}	a, Å	b, Å	γ, deg.	tilt, deg	A_{xy}, Å^2	A_0, Å^2
22.2	1.425 1.454 1.488	0.019 0.052 0.015	0.51 0.41 0.10	0.3 0.3 0.3	4.88	4.98	117.8	20.8	21.5	20.1
25	1.437 1.465 1.490	0.038 0.051 0.014	0.47 0.37 0.10	0.28 0.28 0.28	4.87	4.65	118.2	19.2	21.3	20.1
27.6	1.454 1.476 1.494	0.054 0.042 0.015	0.47 0.37 0.10	0.29 0.29 0.29	4.85	4.93	118.7	18.7	21.0	19.9
30	1.498 1.48	0.018 0.045	0.0 0.28	0.29 0.29	4.92	4.86	120.4	12.5	20.6	20.2
40	1.507 1.497	0.015 0.047	0 0.18	0.30 0.30	4.86	4.83	120.2	6.8	20.25	20.1
45	1.512	0.016	0	0.32	4.80	4.80	120.0	0.0	20.0	20.0

Table A3.25

DPPG monolayer on 0.3 μM Aβ phosphate buffered saline, 0.13 M Na^+, 0.08 M K^+, with pH 7.4..

π, mN/m	Q_{xy}, Å^{-1}	FHWM, Å^{-1}	Q_z, Å^{-1}	FHWM, Å^{-1}	a, Å	b, Å	γ, deg.	tilt, deg	A_{xy}, Å^2	A_0, Å^2
18.1	1.306 1.339 1.461	0.055 0.076 0.018	0.80 0.71 0.09	0.29 0.29 0.29	5.10	5.22	113.0	34.6	24.5	20.2
20	1.311 1.341 1.462	0.047 0.074 0.015	0.78 0.70 0.08	0.29 0.29 0.29	5.09	5.21	113.1	33.9	24.4	20.3
29.7	1.356 1.381 1.469	0.057 0.059 0.017	0.73 0.65 0.08	0.28 0.28 0.30	5.02	5.12	115.1	30.9	23.3	20.0

Table A3.26

DSTAP monolayer on 0.3 μM Aβ in pure water.

π, mN/m	Q_{xy}, Å^{-1}	FHWM, Å^{-1}	Q_z, Å^{-1}	FHWM, Å^{-1}	a, Å	b, Å	γ, deg.	tilt, deg	A_{xy}, Å^2	A_0, Å^2
14.7	1.376 1.466	0.079 0.023	0.71 0.0	0.28 0.30	5.40	5.06	122.2	31.2	23.1	19.8
20	1.386 1.471	0.144 0.030	0.66 0.0	0.29 0.31	5.35	5.03	122.1	29.2	22.8	19.9
30	1.414 1.478	0.064 0.016	0.59 0.0	0.28 0.30	5.21	4.99	121.5	26.0	22.2	19.9
35	1.427 1.486	0.077 0.024	0.55 0.0	0.29 0.30	5.16	4.95	121.4	24.2	21.8	19.9

Table A3.27

DSTAP monolayer on 0.3 μM Aβ phosphate buffered saline, 0.13 M Na^+, 0.08 M K^+, with pH 7.4..

π, mN/m	Q_{xy}, Å^{-1}	FHWM, Å^{-1}	Q_z, Å^{-1}	FHWM, Å^{-1}	a, Å	b, Å	γ, deg.	tilt, deg	A_{xy}, Å^2	A_0, Å^2
17.0	1.332 1.451	0.041 0.013	0.80 0.0	0.28 0.28	5.63	5.16	123.0	35.8	24.4	19.8
20	1.353 1.458	0.043 0.014	0.75 0.0	0.27 0.27	5.51	5.12	122.6	33.3	23.7	19.8
25	1.360 1.457	0.045 0.014	0.74 0.0	0.28 0.28	5.47	5.11	122.4	33.0	23.6	19.8

References.

1. Lösche, M., E. Sackmann, and H. Möhwald, *A Fluorescence Microscopic Study Concerning the Phase-Diagram of Phospholipids.* Berichte Der Bunsen-Gesellschaft-Physical Chemistry Chemical Physics, 1983. **87**(10): p. 848-852.
2. Lösche, H. and H. Möhwald, *Fluorescence Microscopy on Monomolecular Films at an Air Water Interface.* Colloids and Surfaces, 1984. **10**(AUG): p. 217-224.
3. Henon, S. and J. Meunier, *Microscope at the Brewster-Angle - Direct Observation of 1st-Order Phase-Transitions in Monolayers.* Review of Scientific Instruments, 1991. **62**(4): p. 936-939.
4. Honig, D. and D. Möbius, *Direct Visualization of Monolayers at the Air-Water-Interface by Brewster-Angle Microscopy.* Journal of Physical Chemistry, 1991. **95**(12): p. 4590-4592.
5. Albrecht, O., H. Gruler, and E. Sackmann, *Polymorphism of Phospholipid Monolayers.* Journal De Physique, 1978. **39**(3): p. 301-313.
6. Israelachvili, J.N., *Strength of Van-Der-Waals Attraction between Lipid Bilayers.* Langmuir, 1994. **10**(9): p. 3369-3370.
7. Lundquis.M, *Relation between Polymorphism in 2-Dimensional Monomolecular Films on Water to Polymorphism in 3-Dimensional State, and Formation of Multimolecular Films on Water .1. Alkyl Acetates.* Chemica Scripta, 1971. **1**(1): p. 5-&.
8. Lundquis.M, *Relation between Polymorphism in 2-Dimensional Monomolecular Films on Water to Polymorphism in 3-Dimensional State, and Formation of Multimolecular Films on Water .2. Ethyl-Esters of Aliphatic Acids.* Chemica Scripta, 1971. **1**(5): p. 197-&.
9. Kaganer, V.M. and E.B. Loginov, *Symmetry and Phase-Transitions in Langmuir Monolayers - the Landau Theory.* Physical Review E, 1995. **51**(3): p. 2237-2249.
10. Kenn, R.M., K. Kjaer, and H. Möhwald, *Non-rotator phases in phospholipid monolayers?* Colloids and Surfaces a-Physicochemical and Engineering Aspects, 1996. **117**(1-2): p. 171-181.
11. Lakhdar-Ghazal, F., J.L. Tichadou, and J.F. Tocanne, *Effect of Ph and Mono-Valent Cations on the Ionization State of Phosphatidylglycerol in Monolayers - an Experimental (Surface-Potential) and Theoretical (Gouy-Chapman) Approach.* European Journal of Biochemistry, 1983. **134**(3): p. 531-537.
12. Le Calvez, E., et al., *Effect of cations on the dissociation of arachidic acid monolayers on water studied by polarization-modulated infrared reflection-absorption spectroscopy.* Langmuir, 2001. **17**(3): p. 670-674.
13. Johann, R., D. Vollhardt, and H. Mohwald, *Shifting of fatty acid monolayer phases due to ionization of the headgroups.* Langmuir, 2001. **17**(15): p. 4569-4580.
14. Miranda, P.B., Q. Du, and Y.R. Shen, *Interaction of water with a fatty acid Langmuir film.* Chemical Physics Letters, 1998. **286**(1-2): p. 1-8.
15. Shchukin, E.D., et al., *Colloid and Surface Chemistry*. Studies in Interface science, ed. D. Möbius and R. Miller. Vol. 12. 2001: Elsever.
16. Stryer, L., *Biochemistry*. 4 ed. 1997, New York: W.H.Freeman and Company.
17. Sewald, N. and H.-D. Jakubke, *Peptides: Chemistry and Biology*. 2002, Weinheim: Wiley-VCH.
18. Zagorski, M.G., et al., *Methodological and chemical factors affecting amyloid beta peptide amyloidogenicity*, in *Amyloid, Prions, and Other Protein Aggregates*. 1999, ACADEMIC PRESS INC: San Diego. p. 189-204.

19. Binder, H., et al., *The effect of Zn2+ on the secondary structure of a histidine-rich fusogenic peptide and its interaction with lipid membranes.* Biochimica Et Biophysica Acta-Biomembranes, 2000. **1468**(1-2): p. 345-358.
20. Ulrich, A.S., et al., *Ultrastructural characterization of peptide-induced membrane fusion and peptide self-assembly in the lipid bilayer.* Biophysical Journal, 1999. **77**(2): p. 829-841.
21. Glaser, R.W., et al., *Structure analysis of a fusogenic peptide sequence from the sea urchin fertilization protein bindin.* Biochemistry, 1999. **38**(8): p. 2560-2569.
22. Nakanishi, K., N. Berova, and R.W. Woody, eds. *Circular Dichroism. Principles and Applications*. 1994, VCH Publishers, Inc.: New York - Weinheim - Cambridge.
23. Greenfield, N.J., *Methods to estimate the conformation of proteins and polypeptides from circular dichroism data.* Analytical Biochemistry, 1996. **235**(1): p. 1-10.
24. Sreerama, N., S.Y. Venyaminov, and R.W. Woody, *Estimation of protein secondary structure from circular dichroism spectra: Inclusion of denatured proteins with native proteins in the analysis.* Analytical Biochemistry, 2000. **287**(2): p. 243-251.
25. Brahms, S. and J. Brahms, *Determination of Protein Secondary Structure in Solution by Vacuum Ultraviolet Circular-Dichroism.* Journal of Molecular Biology, 1980. **138**(2): p. 149-178.
26. Provencher, S.W. and J. Glockner, *Estimation of Globular Protein Secondary Structure from Circular-Dichroism.* Biochemistry, 1981. **20**(1): p. 33-37.
27. Sreerama, N. and R.W. Woody, *Estimation of protein secondary structure from circular dichroism spectra: Comparison of CONTIN, SELCON, and CDSSTR methods with an expanded reference set.* Analytical Biochemistry, 2000. **287**(2): p. 252-260.
28. Cevc, G., ed. *Phospholipids Handbook*. 1993, MARCEL DEKKER, INC: New York. 988.
29. Als-Nielsen, J., et al., *Principles and Applications of Grazing-Incidence X-Ray and Neutron-Scattering from Ordered Molecular Monolayers at the Air-Water-Interface.* Physics Reports-Review Section of Physics Letters, 1994. **246**(5): p. 252-313.
30. Jacquemain, D., et al., *Crystal-Structures of Self-Aggregates of Insoluble Aliphatic Amphiphilic Molecules at the Air-Water-Interface - an X-Ray Synchrotron Study.* Journal of the American Chemical Society, 1991. **113**(20): p. 7684-7691.
31. Kaganer, V.M., H. Möhwald, and P. Dutta, *Structure and phase transitions in Langmuir monolayers.* Reviews of Modern Physics, 1999. **71**(3): p. 779-819.
32. Helm, C.A., et al., *Phospholipid Monolayer Density Distribution Perpendicular to the Water-Surface - a Synchrotron X-Ray Reflectivity Study.* Europhysics Letters, 1987. **4**(6): p. 697-703.
33. Schalke, M., et al., *Submolecular organization of DMPA in surface monolayers: beyond the two-layer model.* Biochimica Et Biophysica Acta-Biomembranes, 2000. **1464**(1): p. 113-126.
34. Kjaer, K., et al., *An X-Ray-Scattering Study of Lipid Monolayers at the Air Water Interface and on Solid Supports.* Thin Solid Films, 1988. **159**: p. 17-28.
35. Als-Nielsen, J. and H. Möhwald, *Synchrotron x-ray scattering studies of Langmuir films*, in *Handbook of Synchrotron Radiation*, S. Ebashi, M. Koch, and E. Rubenstein, Editors. 1991, Elsevier: Amsterdam.
36. Flach, C.R., et al., *External Reflection Ftir of Peptide Monolayer Films in-Situ at the Air/Water Interface - Experimental-Design, Spectra-Structure Correlations, and Effects of Hydrogen-Deuterium Exchange.* Biophysical Journal, 1994. **67**(1): p. 402-410.
37. Tamm, L.K. and S.A. Tatulian, *Infrared spectroscopy of proteins and peptides in lipid*

bilayers. Quarterly Reviews of Biophysics, 1997. **30**(4): p. 365-429.
38. Goormaghtigh, E., V. Cabiaux, and J.-M. Ruysschaert, *Determination of soluble and membrane protein structure by Fourier Transform Infrared Spectroscopy*, in *Subcellular Biochemistry: Physicochemical Methods in the Study of Biomembranes*, H.J. Hilderson and G.B. Ralston, Editors. 1994, Plenum Press: New York.
39. Flach, C.R., J.W. Brauner, and R. Mendelsohn, *Protein-lipid interaction in monolayers as studied by IRRAS at the a/w interface.* Biophysical Journal, 1996. **70**(2): p. WP251-WP251.
40. Mendelsohn, R., J.W. Brauner, and A. Gericke, *External Infrared Reflection-Absorption Spectrometry Monolayer Films at the Air-Water-Interface.* Annual Review of Physical Chemistry, 1995. **46**: p. 305-334.
41. Mendelsohn, R. and C.R. Flach, *Peptide structure in langmuir films: IRRAS studies of secondary structure and lipid interactions in SP-C and SP-B mimics.* Biophysical Journal, 2003. **84**(2): p. 310A-310A.
42. Buffeteau, T., et al., *Anisotropic optical constants of alpha-helix and beta-sheet secondary structures in the infrared.* Journal of Physical Chemistry B, 2000. **104**(18): p. 4537-4544.
43. Xu, Z., et al., *Orientation of peptides in aqueous monolayer films. Infrared reflection-absorption spectroscopy studies of a synthetic amphipathic beta-sheet.* Langmuir, 2004. **20**(9): p. 3730-3733.
44. Snyder, R.G., H.L. Strauss, and C.A. Elliger, *C-H Stretching Modes and the Structure of Normal-Alkyl Chains .1. Long, Disordered Chains.* Journal of Physical Chemistry, 1982. **86**(26): p. 5145-5150.
45. Macphail, R.A., et al., *C-H Stretching Modes and the Structure of Normal-Alkyl Chains .2. Long, All-Trans Chains.* Journal of Physical Chemistry, 1984. **88**(3): p. 334-341.
46. Cameron, D.G., E.F. Gudgin, and H.H. Mantsch, *Dependence of Acyl Chain Packing of Phospholipids on the Head Group and Acyl Chain-Length.* Biochemistry, 1981. **20**(15): p. 4496-4500.
47. Hübner, W. and A. Blume, *Interactions at the lipid-water interface.* Chemistry and Physics of Lipids, 1998. **96**(1-2): p. 99-123.
48. Dicko, A., H. Bourque, and M. Pezolet, *Study by infrared spectroscopy of the conformation of dipalmitoylphosphatidylglycerol monolayers at the air-water interface and transferred on solid substrates.* Chemistry and Physics of Lipids, 1998. **96**(1-2): p. 125-139.
49. Estrela-Lopis, I., G. Brezesinski, and H. Möhwald, *Dipalmitoyl-phosphatidylcholine/phospholipase D interactions investigated with polarization-modulated infrared reflection absorption spectroscopy.* Biophysical Journal, 2001. **80**(2): p. 749-754.
50. Arrondo, J.L.R., F.M. Goni, and J.M. Macarulla, *Infrared-Spectroscopy of Phosphatidylcholines in Aqueous Suspension - a Study of the Phosphate Group Vibrations.* Biochimica Et Biophysica Acta, 1984. **794**(1): p. 165-168.
51. Laroche, G., et al., *Structure and Dynamics of Dimyristoylphosphatidic Acid Calcium Complexes by H-2 Nmr, Infrared, and Raman Spectroscopies and Small-Angle X-Ray-Diffraction.* Biochemistry, 1991. **30**(12): p. 3105-3114.
52. Mirkin, N.G. and S. Krimm, *Structural dependence of NH stretch mode frequency shifts in amide and peptide.* Journal of Physical Chemistry A, 2004. **108**(25): p. 5438-5448.
53. Nevskaya, N.A. and Y.N. Chirgadze, *Infrared-Spectra and Resonance Interactions of Amide-One and Amide-2 Vibrations of Alpha-Helix.* Biopolymers, 1976. **15**(4): p. 637-

648.
54. Venyaminov, S.Y. and N.N. Kalnin, *Quantitative Ir Spectrophotometry of Peptide Compounds in Water (H2o) Solutions .2. Amide Absorption-Bands of Polypeptides and Fibrous Proteins in Alpha-Coil, Beta-Coil, and Random Coil Conformations.* Biopolymers, 1990. **30**(13-14): p. 1259-1271.
55. Chirgadze, Y.N. and N.A. Nevskaya, *Infrared-Spectra and Resonance Interaction of Amide-One Vibration of Parallel-Chain Pleated Sheet.* Biopolymers, 1976. **15**(4): p. 627-636.
56. Chirgadze, Y.N. and N.A. Nevskaya, *Infrared-Spectra and Resonance Interaction of Amide-One Vibration of Anti-Parallel-Chain Pleated Sheet.* Biopolymers, 1976. **15**(4): p. 607-625.
57. Kubelka, J. and T.A. Keiderling, *Differentiation of beta-sheet-forming structures: Ab initio-based simulations of IR absorption and vibrational CD for model peptide and protein beta-sheets.* Journal of the American Chemical Society, 2001. **123**(48): p. 12048-12058.
58. Venyaminov, S.Y. and N.N. Kalnin, *Quantitative Ir Spectrophotometry of Peptide Compounds in Water (H2o) Solutions .1. Spectral Parameters of Amino-Acid Residue Absorption-Bands.* Biopolymers, 1990. **30**(13-14): p. 1243-1257.
59. Gericke, A., C.R. Flach, and R. Mendelsohn, *Structure and orientation of lung surfactant SP-C and L-alpha-dipalmitoylphosphatidylcholine in aqueous monolayers.* Biophysical Journal, 1997. **73**(1): p. 492-499.
60. Kerth, A., et al., *Infrared reflection absorption spectroscopy of amphipathic model peptides at the air/water interface.* Biophysical Journal, 2004. **86**(6): p. 3750-3758.
61. Bi, X.H., et al., *Secondary structure and lipid interactions of the N-terminal segment of pulmonary surfactant SP-C in Langmuir films: IR reflection-absorption spectroscopy and surface pressure studies.* Biochemistry, 2002. **41**(26): p. 8385-8395.
62. Kuzmin, V.L. and A.V. Mikhailov, *Molecular Theory of Light-Reflection and the Applicability Limits of a Macroscopic Approach.* Optika I Spektroskopiya, 1981. **51**(4): p. 691-695.
63. Kuzmin, V.L., V.P. Romanov, and A.V. Mikhailov, *Light-Reflection on the Boundary of Liquid-Systems and Surface-Layer Structure.* Optika I Spektroskopiya, 1992. **73**(1): p. 3-47.
64. Binder, H. and O. Zschörnig, *The effect of metal cations on the phase behavior and hydration characteristics of phospholipid membranes.* Chemistry and Physics of Lipids, 2002. **115**(1-2): p. 39-61.
65. Copeland, B.R. and H.C. Andersen, *A Theory of Effects of Protons and Divalent-Cations on Phase-Equilibria in Charged Bilayer-Membranes - Comparison with Experiment.* Biochemistry, 1982. **21**(12): p. 2811-2820.
66. Kwon, K.O. and M.J. Kim, *Thermotropic behavior of phospholipid bilayers interacting with metal ions at subzero region.* Colloids and Surfaces B-Biointerfaces, 1996. **6**(2): p. 131-138.
67. Cevc, G., A. Watts, and D. Marsh, *Non-Electrostatic Contribution to the Titration of the Ordered-Fluid Phase-Transition of Phosphatidylglycerol Bilayers.* Febs Letters, 1980. **120**(2): p. 267-270.
68. Kwon, K.O., et al., *Thermotropic Behavior of a Phospholipid-Bilayer Interacting with Metal-Ions.* Langmuir, 1994. **10**(5): p. 1415-1420.
69. Eisenberg, M., et al., *Adsorption of Mono-Valent Cations to Bilayer Membranes Containing Negative Phospholipids.* Biochemistry, 1979. **18**(23): p. 5213-5223.

70. Sacre, M.M. and J.F. Tocanne, *Importance of Glycerol and Fatty-Acid Residues on Ionic Properties of Phosphatidylglycerols at Air-Water-Interface.* Chemistry and Physics of Lipids, 1977. **18**(3-4): p. 334-354.
71. Zhang, Y.P., R. Lewis, and R.N. McElhaney, *Calorimetric and spectroscopic studies of the thermotropic phase behavior of the n-saturated 1,2-diacylphosphatidylglycerols.* Biophysical Journal, 1997. **72**(2): p. 779-793.
72. Grigoriev, D., et al., *Effect of monovalent ions on the monolayers phase behavior of the charged lipid DPPG.* Journal of Physical Chemistry B, 1999. **103**(6): p. 1013-1018.
73. Grigoriev, D., et al., *A novel method to evaluate the phase transition thermodynamics of Langmuir monolayers. Application to DPPG monolayers affected by subphase composition.* Journal of Physical Chemistry B, 2003. **107**(51): p. 14283-14288.
74. Thomas, L.C. and Chittend.Ra, *Characteristic Infrared Absorption Frequencies of Organophosphorus Compounds .7. Phosphorus Ions.* Spectrochimica Acta Part a-Molecular Spectroscopy, 1970. **A 26**(4): p. 781-&.
75. Thomas, L.C. and R.A. Chittenden, *Characteristic Infrared Absorption Frequencies of Organophosphorus Compounds .1. The Phosphoryl (P=O) Group.* Spectrochimica Acta, 1964. **20**(3): p. 467-487.
76. Ulrich, A.S., et al., *Membrane fusion is induced by a distinct peptide sequence of the sea urchin fertilization protein bindin.* Journal of Biological Chemistry, 1998. **273**(27): p. 16748-16755.
77. Barre, P., et al., *Structural and dynamical changes of the bindin B18 peptide upon binding to lipid membranes. A solid-state NMR study.* Biochemistry, 2003. **42**(27): p. 8377-8386.
78. Afonin, S., et al., *'Boomerang'-like insertion of a fusogenic peptide in a lipid membrane revealed by solid-state F-19 NMR.* Magnetic Resonance in Chemistry, 2004. **42**(2): p. 195-203.
79. Afonin, S., et al., *4-Fluorophenylglycine as a label for F-19 NMR structure analysis of membrane-associated peptides.* Chembiochem, 2003. **4**(11): p. 1151-1163.
80. Sinz, A., A.J. Jin, and O. Zschornig, *Evaluation of the metal binding properties of a histidine-rich fusogenic peptide by electrospray ionization Fourier transform ion cyclotron resonance mass spectrometry.* Journal of Mass Spectrometry, 2003. **38**(11): p. 1150-1159.
81. Terzi, E., G. Holzemann, and J. Seelig, *Interaction of Alzheimer beta-amyloid peptide(1-40) with lipid membranes.* Biochemistry, 1997. **36**(48): p. 14845-14852.
82. Bokvist, M., et al., *Two types of Alzheimer's beta-amyloid (1-40) peptide membrane interactions: Aggregation preventing transmembrane anchoring Versus accelerated surface fibril formation.* Journal of Molecular Biology, 2004. **335**(4): p. 1039-1049.
83. Greenfield, N.J., *Applications of circular dichroism in protein and peptide analysis.* Trac-Trends in Analytical Chemistry, 1999. **18**(4): p. 236-244.
84. Kalnin, N.N., I.A. Baikalov, and S.Y. Venyaminov, *Quantitative Ir Spectrophotometry of Peptide Compounds in Water (H2o) Solutions .3. Estimation of the Protein Secondary Structure.* Biopolymers, 1990. **30**(13-14): p. 1273-1280.
85. Kruger, P., et al., *Effect of hydrophobic surfactant protein SP-C on binary phospholipid monolayers. Molecular machinery at the air/water interface.* Biophysical Chemistry, 2002. **99**(3): p. 209-228.
86. Lewis, R., et al., *Fourier transform infrared spectroscopic studies of the interaction of the antimicrobial peptide gramicidin S with lipid micelles and with lipid monolayer and bilayer membranes.* Biochemistry, 1999. **38**(46): p. 15193-15203.
87. Kang, J., et al., *The Precursor of Alzheimers-Disease Amyloid-A4 Protein Resembles a*

Cell-Surface Receptor. Nature, 1987. **325**(6106): p. 733-736.
88. Haass, C., et al., *Amyloid Beta-Peptide Is Produced by Cultured-Cells During Normal Metabolism.* Nature, 1992. **359**(6393): p. 322-325.
89. Soto, C. and B. Frangione, *2 Conformational States of Amyloid Beta-Peptide - Implications for the Pathogenesis of Alzheimers-Disease.* Neuroscience Letters, 1995. **186**(2-3): p. 115-118.
90. Teplow, D.B., *Structural and kinetic features of amyloid beta-protein fibrillogenesis.* Amyloid-Journal of Protein Folding Disorders, 1998. **5**(2): p. 121-142.
91. Walsh, D.M., et al., *Amyloid beta-protein fibrillogenesis - Structure and biological activity of protofibrillar intermediates.* Journal of Biological Chemistry, 1999. **274**(36): p. 25945-25952.
92. Walsh, D.M., et al., *Amyloid beta-protein fibrillogenesis - Detection of a protofibrillar intermediate.* Journal of Biological Chemistry, 1997. **272**(35): p. 22364-22372.
93. Forloni, G., *Neurotoxicity of beta-amyloid and prion peptides.* Current Opinion in Neurology, 1996. **9**(6): p. 492-500.
94. Selkoe, D.J., *Neuroscience - Alzheimer's disease: Genotypes, phenotype, and treatments.* Science, 1997. **275**(5300): p. 630-631.
95. Koppaka, V. and P.H. Axelsen, *Accelerated accumulation of amyloid beta proteins on oxidatively damaged lipid membranes.* Biochemistry, 2000. **39**(32): p. 10011-10016.
96. Lin, H., R. Bhatia, and R. Lal, *Amyloid beta protein forms ion channels: implications for Alzheimer's disease pathophysiology.* Faseb Journal, 2001. **15**(13): p. 2433-2444.
97. Mason, R.P., et al., *Distribution and fluidizing action of soluble and aggregated amyloid beta-peptide in rat synaptic plasma membranes.* Journal of Biological Chemistry, 1999. **274**(26): p. 18801-18807.
98. Waschuk, S.A., et al., *Cellular membrane composition defines A beta-lipid interactions.* Journal of Biological Chemistry, 2001. **276**(36): p. 33561-33568.
99. Yip, C.M., et al., *Cholesterol, a modulator of membrane-associated A beta-fibrillogenesis and neurotoxicity.* Journal of Molecular Biology, 2001. **311**(4): p. 723-734.
100. Yip, C.M. and J. McLaurin, *Amyloid-beta peptide assembly: A critical step in fibrillogenesis and membrane disruption.* Biophysical Journal, 2001. **80**(3): p. 1359-1371.
101. Behl, C., *Amyloid beta-protein toxicity and oxidative stress in Alzheimer's disease.* Cell and Tissue Research, 1997. **290**(3): p. 471-480.
102. Barrow, C.J., et al., *Solution Conformations and Aggregational Properties of Synthetic Amyloid Beta-Peptides of Alzheimers-Disease - Analysis of Circular-Dichroism Spectra.* Journal of Molecular Biology, 1992. **225**(4): p. 1075-1093.
103. Ma, K., M.G. Zagorski, and W.K. Surewicz, *Secondary structure and orientation of the peptide corresponding to a putative transmembrane domain of Alzheimer's amyloid precursor protein.* Biophysical Journal, 1998. **74**(2): p. A220-A220.
104. Fraser, P.E., et al., *Ph-Dependent Structural Transitions of Alzheimer Amyloid Peptides.* Biophysical Journal, 1991. **60**(5): p. 1190-1201.
105. Stine, W.B., et al., *In vitro characterization of conditions for amyloid-beta peptide oligomerization and fibrillogenesis.* Journal of Biological Chemistry, 2003. **278**(13): p. 11612-11622.
106. Coles, M., et al., *Solution structure of amyloid beta-peptide(1-40) in a water-micelle environment. Is the membrane-spanning domain where we think it is?* Biochemistry, 1998. **37**(31): p. 11064-11077.
107. Shao, H.Y., et al., *Solution structures of micelle-bound amyloid beta-(1-40) and beta-(1-42) peptides of Alzheimer's disease.* Journal of Molecular Biology, 1999. **285**(2): p. 755-

773.
108. Fraser, P.E., et al., *Fibril Formation by Primate, Rodent, and Dutch-Hemorrhagic Analogs of Alzheimer Amyloid Beta-Protein.* Biochemistry, 1992. **31**(44): p. 10716-10723.
109. Lynn, D.G. and S.C. Meredith, *Review: Model peptides and the physicochemical approach to beta-amyloids.* Journal of Structural Biology, 2000. **130**(2-3): p. 153-173.
110. Antzutkin, O.N., et al., *Supramolecular structural constraints on Alzheimer's beta-amyloid fibrils from electron microscopy and solid-state nuclear magnetic resonance.* Biochemistry, 2002. **41**(51): p. 15436-15450.
111. Tomski, S.J. and R.M. Murphy, *Kinetics of Aggregation of Synthetic Beta-Amyloid Peptide.* Archives of Biochemistry and Biophysics, 1992. **294**(2): p. 630-638.
112. Goldsbury, C.S., et al., *Studies on the in vitro assembly of A beta 1-40: Implications for the search for A beta fibril formation inhibitors.* Journal of Structural Biology, 2000. **130**(2-3): p. 217-231.
113. Curtain, C.C., et al., *Metal ions, pH, and cholesterol regulate the interactions of Alzheimer's disease amyloid-beta peptide with membrane lipid.* Journal of Biological Chemistry, 2003. **278**(5): p. 2977-2982.
114. Kakio, A., et al., *Cholesterol-dependent formation of GM1 ganglioside-bound amyloid beta-protein, an endogenous seed for Alzheimer amyloid.* Journal of Biological Chemistry, 2001. **276**(27): p. 24985-24990.
115. Kakio, A., et al., *Formation of a membrane-active form of amyloid beta-protein in raft-like model membranes.* Biochemical and Biophysical Research Communications, 2003. **303**(2): p. 514-518.
116. Schladitz, C., et al., *Amyloid-beta-sheet formation at the air-water interface.* Biophysical Journal, 1999. **77**(6): p. 3305-3310.
117. Ege, C. and K.Y.C. Lee, *Insertion of Alzheimer's A beta 40 peptide into lipid monolayers.* Biophysical Journal, 2004. **87**(3): p. 1732-1740.
118. Meister, A., A. Kerth, and A. Blume, *Interaction of sodium dodecyl sulfate with dimyristoyl-sn-glycero-3-phosphocholine monolayers studied by infrared reflection absorption spectroscopy. A new method for the determination of surface partition coefficients.* Journal of Physical Chemistry B, 2004. **108**(24): p. 8371-8378.
119. Ji, S.R., Y. Wu, and S.F. Sui, *Study of beta-amyloid peptide (A beta 40) insertion into phospholipid membranes using monolayer technique.* Biochemistry-Moscow, 2002. **67**(11): p. 1283-1288.
120. Aroti, A., et al., *Effects of Hofmeister anions on DPPC Langmuir monolayers at the air-water interface.* Journal of Physical Chemistry B, 2004. **108**(39): p. 15238-15245.
121. Dieudonne, D., et al., *Secondary structure in lung surfactant SP-B peptides: IR and CD studies of bulk and monolayer phases.* Biochimica Et Biophysica Acta-Biomembranes, 2001. **1511**(1): p. 99-112.
122. Hussain, H., et al., *Amphiphilic block copolymers of poly(ethylene oxide) and poly(perfluorohexylethyl methacrylate) at the water surface and their penetration into the lipid monolayer.* Journal of Physical Chemistry B, 2004. **108**(28): p. 9962-9969.
123. Kowalewski, T. and D.M. Holtzman, *In situ atomic force microscopy study of Alzheimer's beta-amyloid peptide on different substrates: New insights into mechanism of beta-sheet formation.* Proceedings of the National Academy of Sciences of the United States of America, 1999. **96**(7): p. 3688-3693.
124. McLaurin, J. and A. Chakrabartty, *Characterization of the interactions of Alzheimer beta-amyloid peptides with phospholipid membranes.* European Journal of Biochemistry, 1997.

245(2): p. 355-363.
125. McLaurin, J., et al., *Structural transitions associated with the interaction of Alzheimer beta-amyloid peptides with gangliosides.* Journal of Biological Chemistry, 1998. **273**(8): p. 4506-4515.
126. Terzi, E., G. Holzemann, and J. Seelig, *Self-Association of Beta-Amyloid Peptide(1-40) in Solution and Binding to Lipid-Membranes.* Journal of Molecular Biology, 1995. **252**(5): p. 633-642.

Acknowledgements

I would like to thank Prof. Helmuth Möhwald and Dr. Gerald Brezesinski for the possibility to make the PhD work in the Max-Planck Institute and for introducing me in the field of Langmuir monolayers. I especially appreciate for letting me to work independently, though I could get the help whenever I needed it. A special thank to Dr. Gerald Brezesinski for help in solving scientific problems and answering many questions concerning methods, obtained results and strategy for future experiments.

Dr. Vladimir Shapovalov is gratefully acknowledged for his help in solving scientific problems, and for new ideas, which were used in the conducted work. I would also like to thank Dr. Andreas Kerth for introducing me in the IRRAS technique and for very helpful advises. I would like to acknowledge Dr. Olaf Zschoernig for providing the B18.

Dr. Lidong Lee, Dagmara Mirska and Dr. Alexei Antipov are specially thanked for the help in everyday life.

Some of the experiments and sample preparation have been conducted with help of Irina Berndt.

I want to thank all the members of my group for the friendly and kind atmosphere, which is extremely important for any person. Especially I would like thank Sandra Rocha for support and fruitful discussions.

This work was supported by the DFG (BR1378/8-2).